Significance of basin asymmetry and regional groundwater flow conditions in preliminary geothermal potential assessment – Implications on extensional geothermal plays

Ádám Tóth [a,*], Attila Galsa [b], Judit Mádl-Szőnyi [a]

[a] *József & Erzsébet Tóth Endowed Hydrogeology Chair, Department of Geology, ELTE Eötvös Loránd University, Pázmány Péter sétány 1/C, 1117 Budapest, Hungary*
[b] *Department of Geophysics and Space Science, ELTE Eötvös Loránd University, Pázmány Péter sétány 1/C, 1117 Budapest, Hungary*

ARTICLE INFO

ABSTRACT

Extensional domain type geothermal plays, as fertile targets for future resource development, consist of an orogen and an adjoining sedimentary basin of asymmetric physiographic and geologic setting. Preliminary geothermal potential, i.e. prospective geothermal regions, basin-scale flow patterns, heat transfer processes, temperature distribution and appearance of thermal springs were analyzed systematically by numerical simulations in groundwater basins with special emphasis on the effects of basin asymmetry. The importance of basin-scale regional groundwater flow studies in preliminary geothermal potential assessment was demonstrated for synthetic and real-life cases. A simulated series of simplified real systems revealed the effects of anisotropy, asymmetry of the topographical driving force for groundwater flow, basin heterogeneity and basal heat flow on heat accumulation, locations of thermal spring discharge and prevailing mechanisms of heat transfer. As a new aspect in basin-scale groundwater and geothermal studies, basin asymmetry was introduced which has a critical role in discharge and accumulation patterns, thus controlling the location of basin parts bearing the highest geothermal potential. During the reconnaissance phase of geothermal exploration, these conceptual, generalized and simplified groundwater flow and heat transport models can support the identification of prospective areas and planning of shallow and deep geothermal energy utilization, also with respect to reinjection possibilities. Finally, the scope of "geothermal hydrogeology" is defined in a scientific manner for the first time.

1. Introduction and aims

A recent advancement in the geothermal energy sector was the introduction of a novel type of resource cataloging scheme called the geothermal play concept (Moeck 2014; Moeck and Beardsmore 2014; Moeck et al. 2015). In contrast with the previously applied criteria, such as temperature and depth (e.g. Muffler (1979); Sanyal (2005)), here the geological setting and controls form the basis of categorization of geothermal play systems. This concept can provide a common framework for classification and allow planning of exploration and exploitation strategies on the basis of generic geological and tectonic processes and factors. In this context, geothermal geology as a sub-discipline was also introduced aiming at the assessment and characterization of heat source, heat transport mechanisms and heat reservoirs (Moeck 2014; Moeck and Beardsmore 2014; Moeck et al. 2015).

The first classification scheme of geothermal plays was composed by Rybach (1981), who defined conduction (CD) and convection (CV) dominated plays on the basis of the main heat transfer process. Moeck (2014) divided these two groups further into a total of six geothermal play types: CD1 intracratonic basin, CD2 orogenic belt, CD3 basement, CV1 volcanic, CV2 plutonic and CV3 extensional domains. This geothermal resource catalog scheme triggered a revolution and a boom in the classification of already operating and prospective potential geothermal systems and fields applying geothermal play types (e.g. Anderson and Rezaie (2019); Aravena et al. (2016); Prol-Ledesma and Morán-Zenteno (2019); Wang et al. (2018)). Around 90% of worldwide geothermal development is related to CV1 volcanic and CV2 plutonic type geothermal plays followed by the CV3 extensional domain type with around 10% of current world geothermal energy production. However, the latter represents a prospective target for future developments where these extensional domains will be the focus of interest, exploration and extraction, and thus investment strategies

---

(Moeck 2014; Moeck and Beardsmore 2014; Moeck et al. 2015).

In a geothermal system, whose main elements are a heat source, a reservoir and a fluid, heat transport mechanisms are strongly controlled by subsurface fluid flow, which transfers heat and modifies the temperature distribution (Anderson 2005; Dickson and Fanelli 2004; Hochstein 1990; Rybach, 1985; Tóth 1999). Reservoir-scale models are only able to properly describe the temperature distribution and modes of heat transport if proper boundary conditions are imposed, taking into account the effects of basin-scale regional groundwater flow systems (An et al. 2015; Bauer et al. 2019; Bethke 1985; Domenico and Palciauskas 1973; Lazear 2006; Szijártó et al. 2019; Tóth 2015). Consequently, geothermal investigation of a geothermal play and its extended vicinity must involve an analysis of its basin-scale groundwater flow systems because of the interrelationship between regional geothermal heat patterns and gravity-driven regional groundwater flow. For this purpose, processing and interpretation of field-based fluid dynamic parameters, numerical simulation of basin hydraulics and field mapping of manifestations of groundwater's geologic agency, such as naturally discharging thermal springs, may be applied (Tóth 2015).

Issues concerning sustainability and longevity of geothermal systems under operation are the key factors in investment and development. Therefore, based on economic considerations, the rejuvenation of a geothermal system is essential for long-term production. Reinjection can provide a solution for prolonging the operation, however, natural groundwater flow systems are an integral part of geothermal systems as they sustain groundwater replenishment and advective heat transport (Axelsson 2008; Kaya et al. 2011; Mádl-Szőnyi and Simon 2016; Moeck 2014; Stefansson, 1997). Consequently, regional groundwater flow patterns and hydrodynamic processes determine the availability of groundwater serving as a production fluid and the possible need for reinjection, which also depends on the geologic setting and evolution of an area (Horváth et al. 2015; Mádl-Szőnyi and Simon 2016; Moeck 2014). These conditions must be unraveled prior to the actual development in the reconnaissance phase (Mádl-Szőnyi and Simon 2016).

In this paper, we demonstrate the importance of basin-scale topography-driven regional groundwater flow in geothermal studies, as a yet not broadly applied approach, and define "geothermal hydrogeology" which has not been described in a scientific manner in published papers. Accordingly, instead of a reservoir-scale examination of prospective geothermal regions, a basin-scale evaluation approach was applied and flow patterns, heat transfer processes, temperature distribution and appearance of thermal springs were analyzed, justified by the size and extent of geothermal plays. Natural hydrogeological conditions have implications and consequences on geothermal resource characterization, therefore, conclusions regarding possibilities of shallow and deep energy utilization and rejuvenation of geothermal heat can be drawn. Since extensional domain type (CV3) geothermal plays are a fertile target for future developments, a special emphasis is placed on this type of physiographic and geologic setting, i.e. containing an orogen and an adjoining sedimentary basin. In addition, because there are no identical basins and juxtaposed orogens (having the same topographic undulation), several topographic variations of groundwater basins were investigated in numerical simulations and effects of basin asymmetry on geothermal potential are discussed.

2. Theoretical considerations and study approach

For the assessment of geothermal resources, various terms are used describing geothermal potential, which represents the potentially exploitable geothermal energy stored in a given subsurface domain. Theoretical potential, the broadest term, refers to the physically usable geothermal energy, the heat in place. However, on the basis of economic considerations and for practical reasons, technical, economic, sustainable and developable potential are applied denoting smaller and smaller fractions of the theoretical potential. As the latter require field-based information, regional assessment of geothermal resources is limited to

the theoretical potential (Nádor et al. 2019; Rybach 2010; Rybach 2015). Throughout this paper, the prospective resources and potential heat accumulations were examined, therefore, geothermal potential hereinafter refers to the theoretical potential.

The relevance of topography-driven regional groundwater flow, in the form of hydraulic head variation, acting in potential geothermal areas was recognized even before the geothermal play concept (Craw et al. 2005; Deming et al. 1992; Hochstein 1988; Smith and Chapman 1983). The undulation of topography and the groundwater table serves as a driving force of fluid flow not only in mountainous or volcanic regions but also in sedimentary basins (e.g. Bethke (1989); Garven (1995)). Since topographical variations do exist at any part of the continental lithosphere, and they are visualized in all conceptual figures of various play types of Moeck (2014), the existence of regional-scale groundwater flow cannot be excluded. Even more so, the role of groundwater flow in the formation of heat accumulations needs to be taken into account.

Basin-scale groundwater studies started with the application of simplified homogeneous and isotropic representations of flow fields: a Unit basin with a linearly sloping water table and a Composite basin (or Small drainage basin) with a sinusoidal undulation of the upper boundary. Later, the theory of topography-driven regional groundwater flow has evolved into a conceptual framework in the understanding of subsurface flow patterns and related manifestations in hydraulically continuous basins with hierarchically nested groundwater flow systems (Bredehoeft 2018; Tóth 1962b; Tóth 1963; Tóth 1970; Tóth 1971; Tóth 1980; Tóth 1995; Tóth 1999; Tóth 2009a). The core of this concept is the recognition of the basin as being a unit – in which the same processes act – for regional-scale hydrogeological studies. These synthetic basin models can serve as a starting point of understanding real-life cases by modifying (squeezing, stretching, exaggerating and diminishing) the original geometry, medium and water table (Tóth 2009a; Tóth 2016). In this concept, the terms "regional flow" and "basin-scale flow" are used interchangeably as a regional flow system is the highest order of flow systems in a basin and it links the principal groundwater divide and valley hydraulically, and the extent of a regional flow system is comparable with the size of the basin. Contrary to the definition of a geological basin, groundwater basins are rather only "half-basins" extending from a water divide to a valley, which are axes of symmetry (Tóth 1962b; Tóth 1963). To overcome this ambiguity, in this paper, two synthetic "half-basins" were merged and the resulting "full" basins were considered as input geometry for numerical simulation.

One of the natural manifestations of groundwater flow is the occurrence of springs and thermal springs with elevated water temperature (Tóth 2015). There are various definitions of a thermal spring: a common one being where water temperatures are higher than the annual average air temperature, 20 °C or 36 °C (Krešić and Stevanović 2009; Pentecost et al. 2003). We used a threshold of 30 °C for thermal waters on the basis of the Lindal diagram and regional practice (Gudmundsson et al. 1985; Lindal 1973; Rman et al. 2020). Studies have highlighted that local permeability changes, conduit faults, fault zones and fractures favor in-the-fault-plane circulation and development of thermal springs (Andrews et al. 1982; Bredehoeft 1997; Forster and Smith 1989; Jiang et al. 2018; López and Smith 1995). However, springs are the natural terminal points of groundwater flow paths, and in this manner, they can reflect the near-surface and subsurface geothermal anomalies, as well as heat accumulations controlled by basin-scale groundwater flow (Engelen and Kloosterman 2012; Krešić and Stevanović 2009; Renner et al. 1975; Tóth 1971; Tóth 2009b; Tóth 2015). Thermal springs can, thus, be preliminary indicators of geothermal resources. Furthermore, their hydrogeochemical facies is widely used for the characterization of geothermal reservoirs (Arnórsson et al. 2006; Fournier 1977; Giggenbach 1988; Yang et al. 2017). Nevertheless, the absence of thermal springs does not directly mean a lack of underground stored heat and geothermal systems lacking a clear surface manifestation are generally referred to as "blind" systems

(Moeck 2014).

In this study, all above-mentioned and outlined considerations and ideas were combined. To this end, theoretical geothermal potential in "full" basins with topography-driven regional groundwater flow was investigated with a special emphasis on thermal water occurrence (temperature above 30 °C). The applied basin geometries might be analogous to any kind of geothermal plays, but mostly resemble asymmetric orogen plus sedimentary basin settings. In this context, a symmetric basin refers to a "full" basin which has the same values of water table rise at the two water divides, so that it is symmetric in terms of the topographical driving force of groundwater flow. Accordingly, asymmetric basins possess different elevations of the water table at the margins (i.e. hydraulic heads), yielding an asymmetric driving force. Note, that entirely symmetrical basins do not exist in nature, however, "hydrogeologically symmetric" basins might be present.

3. Study series in synthetic groundwater basins

A numerical simulation series was performed on a wide range of synthetic groundwater basins with symmetric and asymmetric topographical driving forces of groundwater flow to reveal the effects of various geometric and geologic parameters and agents, such as anisotropy of hydraulic conductivity, surface undulation, sedimentary basin fill and temperature gradient. Simulation results were compared based on descriptive response parameters (defined in section 3.2.) which are indicative of theoretical geothermal potential.

3.1. Model description and scenarios

Numerical simulation of subsurface flow and coupled heat transfer was carried out in COMSOL Multiphysics 5.3a, which is a finite element numerical software package for multi-disciplinary problems (Zimmerman 2006). Steady-state Fluid flow (Porous Media and Subsurface Flow/ Darcy's Law) and Heat transfer (Heat transfer in porous media) modules were applied assuming constant fluid density and dynamic fluid viscosity and gravitational acceleration. In this manner, conduction and advection/forced thermal convection (coupled via Darcy velocity) were

the only sources of heat transfer. The effects of heat production and free thermal convection caused by density variations due to temperature change were neglected and groundwater flow was induced purely by water table undulation (Domenico and Palciauskas 1973). However, free and mixed thermal convection cannot be excluded in deeper parts of the basins and in heterogeneous systems (Clauser and Villinger 1990; Lopez et al. 2016; Raffensperger and Vlassopoulos 1999; Szijártó et al. 2019; Yang et al. 2006). As topography-driven regional groundwater flow is the predominant driving force of groundwater on a basin scale, for the sake of simplicity, further driving forces were not included, such as compaction, compression and chemical composition variations (Bethke 1989; Person et al. 1996; Tóth 1987).

The basic model geometry was a merged Unit basin (left-hand side) and a Composite basin (right-hand side) functioning as a "full" basin. This geometry was used by several other authors and in study topics (e.g. Carrillo-Rivera and Ouysse (2013); Jiang et al. (2014); Khan and Khan (2019); Tóth (1999)). The size of the basins was set according to the original values: 20,000 ft. + 20,000 ft. (6096 m + 6096 m, altogether ~12.2 km) in the horizontal extent and 10,000 ft. (3048 m) as the minimum basin depth at the mid-point of the basin (Tóth 1962b; Tóth 1963). Note that Tóth used feet as a unit thus we also defined the geometries in feet to have a direct link to his basic models but the values in meters are also provided for reference. Due to numerical reasons, the linearly sloping surface of the Unit basin was modified to a half period of a cosine function to avoid calculation issues along the sharp edges. This is the modified Unit basin (Unit basin*) (Fig. 1.):

$$w_{wt} = w_0 - acos\frac{2\pi x}{\lambda} = w_0 - acosbx \qquad (1)$$

$$b = \frac{2\pi}{\lambda} \qquad (2)$$

where w_{wt} is the water table variation on the upper boundary, w_0 is the reference elevation, a is the cosine function amplitude, x is horizontal distance, λ is wavelength and b is wave number.

The Composite basin on the right-hand side has a sinusoidally undulating surface superimposed on a regional slope:
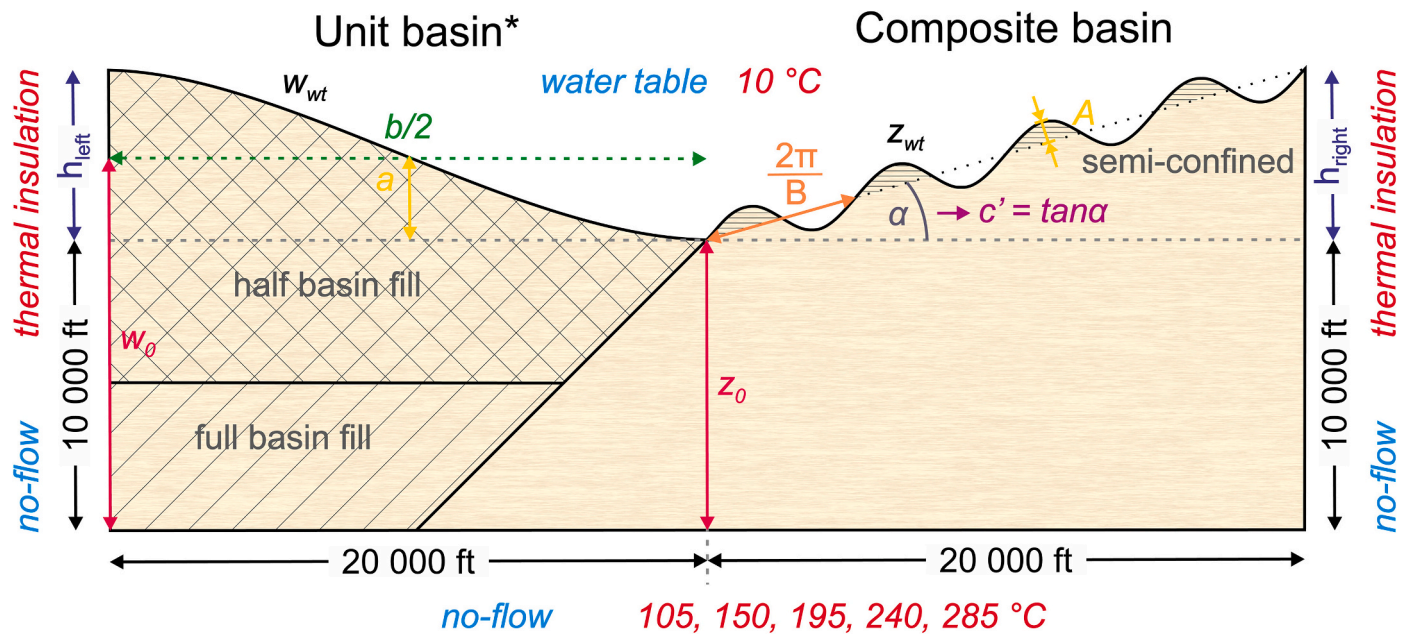

Fig. 1. Basic model geometry indicating basin parameters and applied boundary conditions (hydraulic in blue, thermal in red), see text for a detailed description. Unit basin* refers to the modified Unit basin with a half-cosine upper boundary. Half and full sedimentary basin fill and a semi-confined cover were applied in the heterogeneous models. (10,000 ft. = 3048 m, 20,000 ft. = 6096 m). (For interpretation of the references to colour in this figure legend, the reader is referred to the web version of this article.)

$$z_{wt} = z_0 + x\tan\alpha + A\frac{sin\left(B\frac{x}{cos\alpha}\right)}{cos\alpha} \tag{3}$$

$$a' = \frac{A}{cos\alpha} \tag{4}$$

$$b' = \frac{B}{cos\alpha} \tag{5}$$

$$c' = tan\alpha \tag{6}$$

then: $z_{wt} = z_0 + c'x + a'\sin(b'x)$ (7)

where z_{wt} is the water table undulation on the upper boundary, z_0 is the reference elevation, α is the angle of the regional linear slope, A is the amplitude and B is the wave number of the undulation (Tóth 1963; Tóth 2009a). Hydraulic head (water table) on the left (h_{left}) and the right (h_{right}) served as the regional driving force of groundwater flow (Fig. 1.).

Boundary conditions for groundwater flow were also adjusted to the original setting: bottom and sides being impermeable, no-flow boundaries and upper boundary acting as a varying water table (w_{wt} and z_{wt}). For the heat transfer module, thermal insulation on the sides and an arbitrary constant air temperature of 10 °C were applied. At the bottom, various values of constant temperature were defined as a boundary condition according to various initial geothermal gradients: 105 °C (30 °C/km), 150 °C (45 °C/km), 195 °C (60 °C/km), 240 °C (75 °C/km) and 285 °C (90 °C/km).

Each model geometry was simulated with a set of hydraulic conductivity values, spanning 10 orders of magnitude (31 cases), in a logarithmically quasi-equidistant way: 10^{-12}, $2\cdot10^{-12}$, $5\cdot10^{-12}$, 10^{-11} … $2\cdot10^{-3}$, $5\cdot10^{-3}$, 10^{-2} m/s of horizontal hydraulic conductivity (K_{xx}) representing a wide variety of geologic media: from nearly impermeable, intact metamorphic aquitards via permeable siliciclastic and carbonate aquifers to very good, high-yield unconsolidated aquifers (e.g. Brassington (2017); Domenico and Schwartz (1997); Freeze and Cherry (1979)). However, heterogeneous cases were also investigated analogue to an orogen plus a sedimentary basin setting. In the basin part (left-hand side, Unit basin*), half and full basin fill units were introduced (Fig. 1.). The former can be interpreted as a confining layer in the upper half of the basin and the latter is a sedimentary sequence occupying the basin over the total thickness. The last case is the semi-confined situation of the orogen part (right-hand side, Composite basin) which represents a confining sedimentary cover of limited thickness (Mádl-Szőnyi and Tóth 2015). The K_{xx} of the basin fill/sedimentary cover was kept constant at 10^{-7} m/s in all simulation scenarios. As a general rule of thumb, a vertical hydraulic conductivity (K_{yy}) of one order of magnitude less than the horizontal (K_{xx}) was applied, except those cases, where the effect of anisotropy (ε = K_{xx}/ K_{yy}) was examined using different ratios.

Thermal conductivity of subsurface materials was kept constant, except for a simple differentiation between a value of 1.7 W/(m·K) for the homogeneous cases and 2.5 W/(m·K) for the sedimentary basin-fill and confining unit (Beardsmore and Cull 2001; Clark 1966; Eppelbaum et al. 2014; Sharma 1997). For the thermal conductivity of water, a value of 0.6 W/(m·K) was adopted. A value of 4200 J/(kg·K) was used for the heat capacity of water (at constant pressure) and a uniform value of 1000 J/(kg·K) for the geologic units.

The model domain was divided into triangular finite elements, whose maximum size was 80 m. Along the critical upper and lower boundaries, where sharp changes could occur in temperature, boundary mesh layers were inserted to reduce the finite element size and refine the solution. The models contained 191,630 finite elements on average. For visualization of flow patterns, magnitude controlled streamlines were chosen, thus the flow between each pair of adjacent streamlines is the same throughout the domain, giving streamlines that are more dense where the magnitude of the field is high.

Altogether, 30 model geometries were studied with 31 variations of hydraulic conductivity, yielding 930 scenarios of synthetic basins.

Effects of i) anisotropy (models 1–2), ii) water table variation of the Composite basin (after Tóth (1962a); Tóth (1962b); Tóth (1963); Tóth (2009a)) and the Unit basin* parts (regional slope, the amplitude of undulation) (models 3–4), iii) heterogeneous basins with sedimentary fill (half and full, semi-confined) (models 5–6) and iv) various basal thermal boundary conditions according to various geothermal gradients (30, 45, 60, 75, 90 °C/km) (models 7–8) were subsequently examined (Table A.1.).

3.2. Response parameters

The simulation results of the synthetic basin models were interpreted and compared on the basis of 5 response parameters, that describe the preliminary theoretical geothermal potential. (1) Maximum temperature of discharging groundwater (T_{max}) is related to the occurrence of thermal springs, which can be an indication of accumulated heat in a subsurface domain. As the temperature was kept constant along the upper boundary, the outflowing water temperature would have been 10 °C. Therefore, this parameter was taken along a line parallel to the surface but situated 50 m deeper, causing a slight systematic difference in maximum water temperatures. (2) Average temperature (T_{av}) of the model domain was a general parameter characterizing the temperature conditions. (3) The area of the thermal water "reservoir" in proportion to the whole model domain (A% ($T > 30$ °C)) describing the quantity of theoretically available, heat in place. (4) All of these response parameters, by all means, were governed by the relative dominance of conduction or advection, caused by groundwater flow due to topographical variations, and also hydraulic conductivity of the medium. Therefore, a non-dimensional Péclet number was calculated to reveal the predominance of conduction or advection as the main heat transfer process in various model settings (e.g. Szijártó et al. (2019); Wooding (1963)):

$$Pe = \frac{\rho_w \cdot c_{p_w} \cdot \overline{d} \cdot \overline{U}}{\lambda_b} \tag{8}$$

$$\lambda_b = n \cdot \lambda_w + (1-n)\lambda_m \tag{9}$$

where ρ_w is the density of water (1000 kg/m^3), c_{pw} is the heat capacity at constant pressure of water (4200 J/(kg·K)), $\overline{d}$ is the average model depth (m), which was calculated for each model setting, $\overline{U}$ is the average Darcy velocity (m/s), λ_b, λ_w, λ_m are the bulk, water and matrix thermal conductivities (W/(m·K)), respectively, and n is porosity (0.2). In cases where Pe $<<$1, heat transfer was controlled by conduction rather than advection. If $Pe>>1$, thermal advection by groundwater flow acts as the dominant process of heat transport. Around a value of 1, both processes can be relevant and can co-exist. (5) Finally, the location of discharging thermal water (T > 30 °C) along the horizontal axis was plotted in order to find the position of possible thermal springs. In this part of the graph, the location of T_{max} is indicated by the corresponding symbol, and bars to the left and right represent the width of the thermal water plume reaching the near-surface.

4. Results and interpretation

The simplest model setup was the homogeneous and isotropic case of the base model geometry (Unit basin* + Composite basin; model ID: 1 in Table A.1.), i.e. the original figure of Tóth (1999). The model revealed asymmetric flow field in the two basin-halves due to the different variations of water table along the upper boundary. The mid-basin regional discharge pattern (in the vicinity of the boundary between the two basin-halves) was also asymmetric, even though, the basin was symmetric in terms of the regional topographic driving force. Its asymmetry was even more apparent in the temperature field, where a deflection of heat accumulation appeared. In the deeper part, the heat was mostly symmetrically distributed, however, in the shallower part (upper 1/4 of the basin), there was a departure to the left of the theoretical boundary
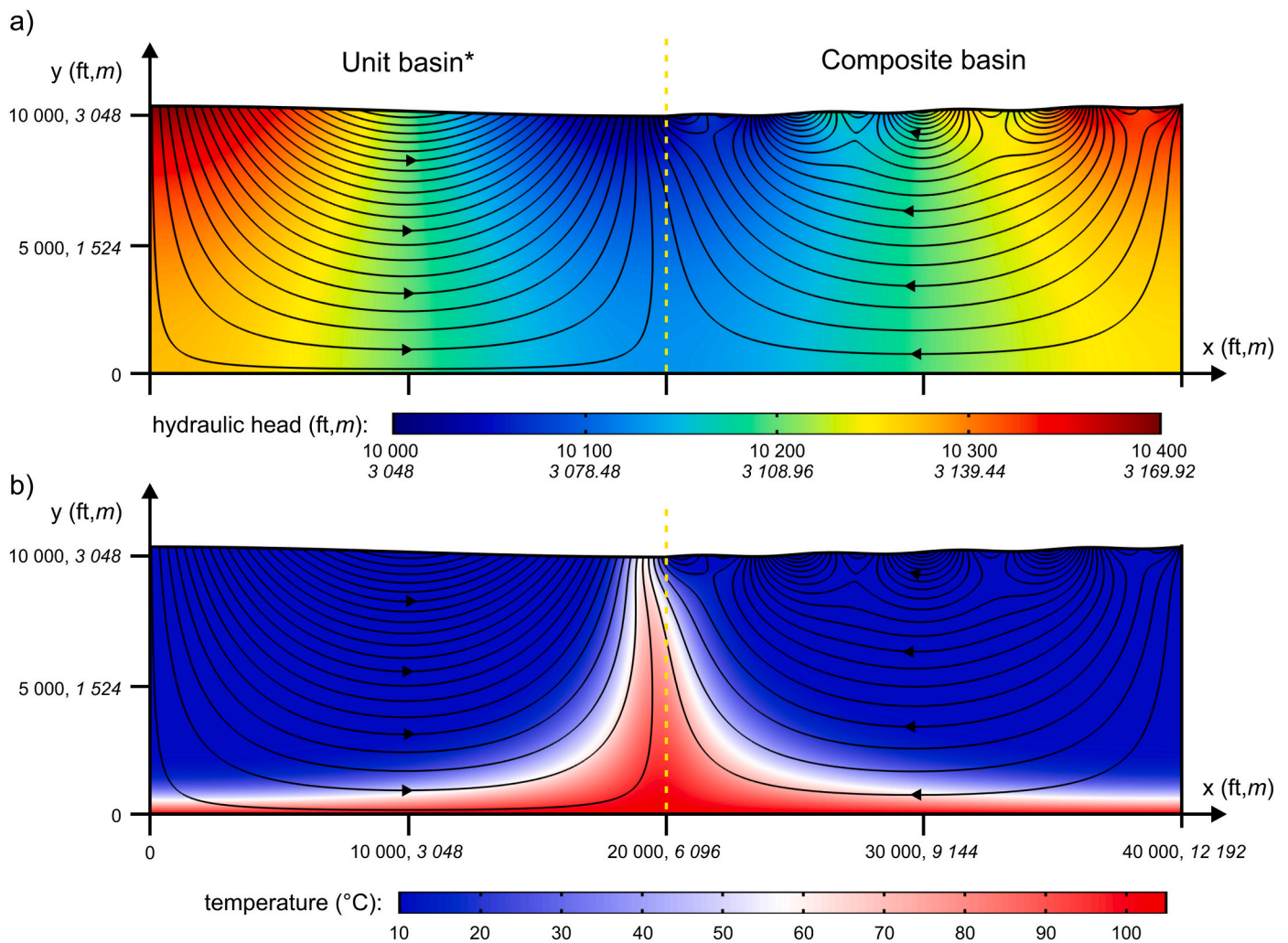
Fig. 2. Simulation results of the homogeneous, isotropic and symmetric model 1 at $K = 10^{-6}$ m/s. a) Hydraulic head distribution with magnitude controlled streamlines. b) Temperature field with streamlines. Unit basin* refers to the modified Unit basin with a half-cosine upper boundary. Calculated recharge rate: 496 mm/yr, maximum of Darcy velocity magnitude: $2.67 \cdot 10^{-7}$ m/s, number of streamlines: 20. Yellow dashed line represents the boundary of the two basin-halves, i. e. the centerline. (For interpretation of the references to colour in this figure legend, the reader is referred to the web version of this article.)

(centerline) due to local-scale water table variation in the Composite basin-half (Fig. 2.). In this way, the hottest water could be found ~300 m from the centerline in the Unit basin* part, not at the main hydraulic head minimum, i.e. at 6096 m. Even in the simplest model geometry, asymmetry of the flow field and heat accumulation was unraveled and basin interplay had an important role. Therefore, the conceptual figure of Tóth (1999) should be modified regarding the mid-basin discharge pattern and temperature field.

4.1. Effects of anisotropy

In groundwater flow modelling practice, as a rule of thumb, the vertical hydraulic conductivity is often taken as one order of magnitude less than the horizontal ($\varepsilon = 10$). Moreover, the anisotropy of the hydraulic conductivity is even more relevant in siliciclastic sedimentary basins, depending on the stratification of various formations, and can reach values of 100–1000 (Freeze and Cherry 1979; Wang et al. 2011). Hence, the effects of anisotropy were investigated in 4 cases: model 2.a ($\varepsilon = 10$, Fig. B.1.), 2.b ($\varepsilon = 100$, Fig. B.2.) and 2.c ($\varepsilon = 1000$, Fig. B.3.) plus model 1, where $\varepsilon = 1$ (isotropic).

On the basis of the simulation results (Fig. 3.), maximum values of the maximum temperature of discharging water (max(T_{max})) gradually decreased as anisotropy increased: ~58 °C ($\varepsilon = 1$), ~36 °C ($\varepsilon = 10$),

~19 °C ($\varepsilon = 100$) and ~ 15 °C ($\varepsilon = 1000$). Meanwhile, these maximum values were reached at higher and higher horizontal hydraulic conductivities: in the same order at $5 \cdot 10^{-6}$, 10^{-5}, $2 \cdot 10^{-5}$ and 10^{-4} m/s. The latter 2 cases ($\varepsilon = 100$ and 1000) did not result in thermal spring occurrence (Fig. 3.a). The portion of the thermal water reservoir (A% ($T > 30$ °C)) and average temperature (T_{av}) show a similarly shaped curve, so these parameters were plotted on the same graph. A plateau of both parameters appeared at ~79% of A% and ~ 58 °C of T_{av}, however, from $K > 10^{-8}$ m/s the amount of thermal water and the associated average temperature is inversely proportional to the horizontal hydraulic conductivity. There was also a difference of 3 orders of magnitude in K between the case of $\varepsilon = 1$ ($K = 10^{-8}$ m/s) and $\varepsilon = 1000$ ($K = 10^{-5}$ m/s). Anisotropy strongly affected the minimum values of A% and T_{av} at the highest hydraulic conductivity ($K = 10^{-2}$ m/s): ~2%, ~10 °C ($\varepsilon = 1$), ~3%, ~12 °C ($\varepsilon = 10$), ~28%, ~27 °C ($\varepsilon = 100$) and ~ 68%, ~50 °C ($\varepsilon = 1000$), respectively (Fig. 3.b). The Péclet number was dependent only on the average Darcy velocity, as other parameters were constant in this set of cases (water density, heat capacity at constant water pressure, average model depth and thermal conductivity), thus values of *Pe* were a linear function of K. The critical value of 1 was reached at various hydraulic conductivities: 10^{-8} ($\varepsilon = 1$), $5 \cdot 10^{-8}$ ($\varepsilon = 10$), 10^{-7} ($\varepsilon = 100$) and $5 \cdot 10^{-7}$ m/s ($\varepsilon = 1000$). Increasing anisotropy thus promoted the dominance of conduction as the main heat
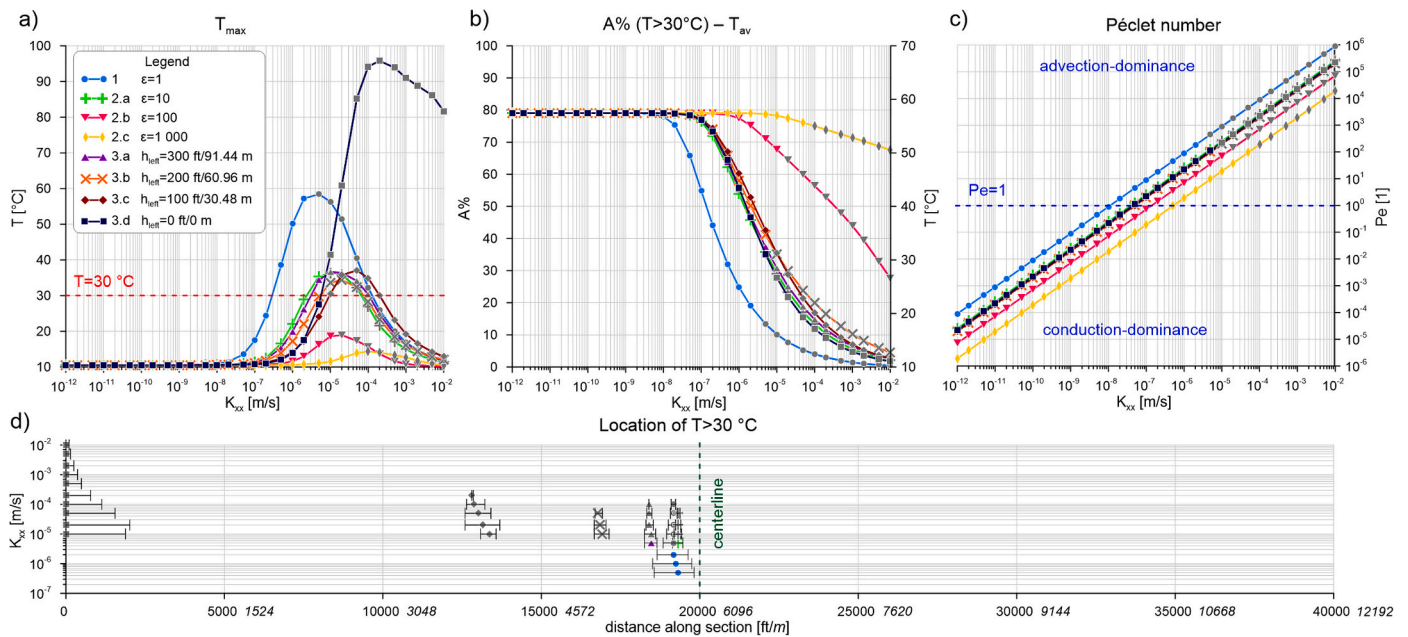
Fig. 3. Response parameters in model settings of 1, 2.a, 2.b, 2.c, 3.a, 3.b, 3.c and 3.d. a) Maximum outflowing water temperature, b) area of the thermal water reservoir (T > 30 °C) in proportion to the whole model domain and average water temperature, c) Péclet number plotted against horizontal hydraulic conductivity and d) location and horizontal extent of thermal water (T > 30 °C) discharge. Scenarios with recharge>1 m/yr are indicated by grey colour.

transfer process (Fig. 3.c). The location of thermal water discharge on the surface could be visualized only for 2 cases with lower anisotropy ($\varepsilon = 1$ and 10). These model sets (model 1 and 2.a) indicated a shift of near-surface thermal water appearance: discharge occurred at ~5800 m left of the centerline in spite of its minimum value of hydraulic head. This asymmetric phenomenon was caused by the different water table variations of the two basin-halves. The extent of the thermal water plume was reduced by applying an anisotropy of 10 (Fig. 3.d).

As a general interpretation, increasing anisotropy, which means decreasing vertical hydraulic conductivity, favors horizontal groundwater flow since the vertical component is retained and, thus, increasing anisotropy lessens the intensity of flow. These changes are reflected in all of the response parameters. By increasing anisotropy, the transition from a conduction-dominated to an advection-dominated domain – revealed by the Péclet number – requires larger horizontal hydraulic conductivity values. Suppressing advection more effectively by conduction resulted in an increase in average temperature and the relative fraction of the thermal water reservoir because of the shallow penetration depth of the flow lines and consequent undisturbed conductive temperature field in the deeper part of the basin (retained advective cooling). On the other hand, maximum outflowing water temperature decreased owing to the higher anisotropy values, since conduction could not generate considerable heat anomalies and thermal water was not transported toward the surface. Hence, in these cases, the absence of thermal springs actually resulted in a larger extent of the thermal water reservoir with higher temperatures compared to models with thermal water discharge.

4.2. Effects of water table variations

Topographical variations of basin surfaces are unquestionably present and as there are no identical basins and basin-halves, an infinite number of various water table settings might exist. Therefore, here, only a limited number of cases were presented in two packages of model sets: topographical variations of the Unit basin* and Composite basin parts, respectively. The first series of models covered the Unit basin* part, in which a gradual decrease of the maximum water table rise on the left-hand side (h_{left}) was implemented: starting with model 2.a (400 ft./

121.92 m) and then 3.a (300 ft./91.44 m, Fig. B.4.), 3.b (200 ft./60.96 m, Fig. B.5.), 3.c (100 ft./30.48 m, Fig. B.6.) and 3.d (0 ft./m, Fig. B.7.), while the right-hand side part was kept unaltered (Table A.1.).

The maximum temperature of discharging water (T_{max}) for the four models (2.a, 3.a,b,c) with h_{left} greater than 0 m was not more than ~35 °C. A sudden rise in maximum water temperature occurred in the flat basin surface case (0 m, model 3.d). This response parameter reached a temperature of ~95 °C, almost the possible maximum of 105 °C, which was set as the bottom boundary condition. All of the cases produced thermal water discharge on the surface, mostly between hydraulic conductivities of $2\cdot10^{-6}$ and 10^{-4} m/s (Fig. 3.a). A plateau of the thermal water portion appeared at ~79% and of the average temperature at ~58 °C, at a hydraulic conductivity of $2\cdot10^{-8}$ m/s. There were only slight changes regarding A% and T_{av} in the studied cases: their minima were ~ 3–5% and ~ 12–13 °C, respectively (Fig. 3.b). There were very minor differences in Péclet number, reflecting the driving force and consequent magnitude variation of groundwater flow caused by the modified water table shapes, as Pe was dependent only on average Darcy velocity. The critical value of 1 was reached at K ≈ $5\cdot10^{-8}$ m/s (Fig. 3.c). The location of thermal water discharge on the surface displayed a gradual shift from the mid-basin parts toward the leftmost positions as h_{left} decreased: from ~5800 m, via ~5500 m, ~5200 m, ~4000 m to 0 m. This migration pattern of thermal discharge was caused by the asymmetry of topographical driving forces, i.e. higher hydraulic head values in the right-hand side Composite basin-half. The extent of the thermal water plume increased as the hydraulic head on the left-hand side decreased and as the hydraulic conductivity was reduced (Fig. 3.d).

In the second series of models investigating basin asymmetry, the Composite basin part was altered in several ways: the regional slope of water table rise (c' = 0.01, 0.02 and 0.05) and amplitude of the superimposed sine function (a' = ~50, ~100 and ~ 200 ft./15.24, ~30.48, ~60.96 m) were varied resulting in h_{right} changes (200, 400 and 1000 ft./60.96, 121.92 and 304.8 m). (Note that the value of b', which is related to wavelength, was also varied, and water table minima lower than 10,000 ft. (3048 m) could develop in the Composite basin part.) These values of surface undulation were adopted from (Tóth 2009a). The left-hand side basin-half was kept unaltered. Altogether 9 model sets

were examined: model 2.a, 4.a, 4.b, 4.c, 4.d, 4.e, 4.f, 4.g and 4.h (see Table A.1. for geometry parameters and Figs. B.8–15. for the results).

The simulation results of this model set were quite similar to the previous ones, so the response parameters generally portrayed very similar curves. The maximum temperature of discharging water (T_{max}) was not more than ~32 °C, except for one model geometry (4.g), where this value was a bit under 30 °C, i.e. without thermal water discharge. Water temperatures higher than 30 °C were mostly restricted to hydraulic conductivities of $2 \cdot 10^{-6}$ to $5 \cdot 10^{-5}$ m/s (Fig. 4.a). The portion of the thermal water reservoir (A% ($T > 30$ °C)) and average temperature (T_{av}) had the same plateau, starting at $K = 2 \cdot 10^{-8}$ m/s with values of ~79% of A% and ~58 °C of T_{av}. There were only minor changes regarding A% and T_{av} in the studied cases: their minima were ~4% and ~13 °C, respectively (Fig. 4.b). Minor differences could be observed in the values of Pe reflecting changes in the magnitude of groundwater flow due to water table variations: slightly higher Pe numbers were characteristic for cases (4.b, 4.e and 4.h) with higher water table maxima (1000 ft./304.8 m), i.e. groundwater flow was more intense. Otherwise, the critical value of $Pe = 1$ was reached at $K \approx 5 \cdot 10^{-8}$ m/s (Fig. 4.c). The location of thermal water discharge on the surface was controlled by the water table configuration. In cases (2.a and 4.d), where the regional slope was c' = 0.02 and the sine amplitude was a' $\approx$ 50 and 100 ft. (15.24 and 30.48 m), the thermal water discharged at the "regular" place of ~5800 m, i.e. at the discharge area of the reference model 1. As the regional slope increased to 0.05 (models 4.b, 4.e and 4.h), the location of thermal water occurrence migrated to ~4900–5200 m along the x-axis since groundwater was forced leftward due to a higher position of the water table on the right. With a lower regional slope (c' = 0.01), and in cases with a sine amplitude of ~50 and ~100 ft. (15.24 and 30.48 m) (models 4.a and 4.c), the opposite situation occurred: the topographical driving force acting on the left-hand side was larger than in the right-hand side basin-half, so groundwater was pushed rightward and the thermal water discharge took place at ~7200 m. As the sine amplitude was further increased to ~200 ft. (~60.96 m) (model 4.f), the location of discharge moved farther to ~8700 m because of local-scale variation of the water table and consequent shallow penetration depth of the flow paths. The width of the thermal water plume gradually decreased as the discharge location

migrated along the x-axis and as the water table gradient decreased (Fig. 4.d).

Effects of topographical variations were investigated in altogether 13 model sets, in which several symmetric and asymmetric cases by changing water table configuration were simulated, while other parameters of the medium were not modified ($\varepsilon = 10$, basal $T = 105$ °C). The curves of response parameters T_{av} and A% exhibited roughly the same trends and similar values of T_{max} outflowing water temperatures were obtained. A heavily undulating surface (high value of a') could cause fragmentation of the flow pattern and facilitate a shallow penetration depth of groundwater, thus, advection was predominant in the near-surface segment, while in the deeper part of the basin, conduction could act as the main heat transfer process. In the same way, a higher regional slope (c') could generate a larger driving force of groundwater flow and consequently reduced the contribution of conduction. These phenomena were reflected in the slight variation of the average Péclet number, whose actual local values could widely vary within the basin. Water table configuration mostly affected the occurrence and location of the thermal water discharge since the temperature field was controlled by basinal and local-scale water table variations. Regarding the extreme case of a flat basin-half (model 3.d), thermal water reached the surface due to the applied no-flow boundary conditions prescribed on the side walls. However, thermal water could theoretically proceed farther leftwards until facing a concurrent opposing flow system. In conclusion, the geothermal potential was seemingly independent of the water table configuration, since only minor changes could be observed in the average and maximum outflowing temperature, portion of the thermal water reservoir and Péclet number. Nevertheless, discharge and accumulation patterns were strongly controlled by variation of the topographical driving force resulting in the relocation of basin parts possessing the highest geothermal potential.

4.3. Effects of basin heterogeneity

Similarly to various topographical and water table configurations, heterogeneities of the basin surely exist, a homogeneous medium might be present only on the local-scale. Stratification, sedimentary sequences and tectonic evolution of a basin can create unique geology, which
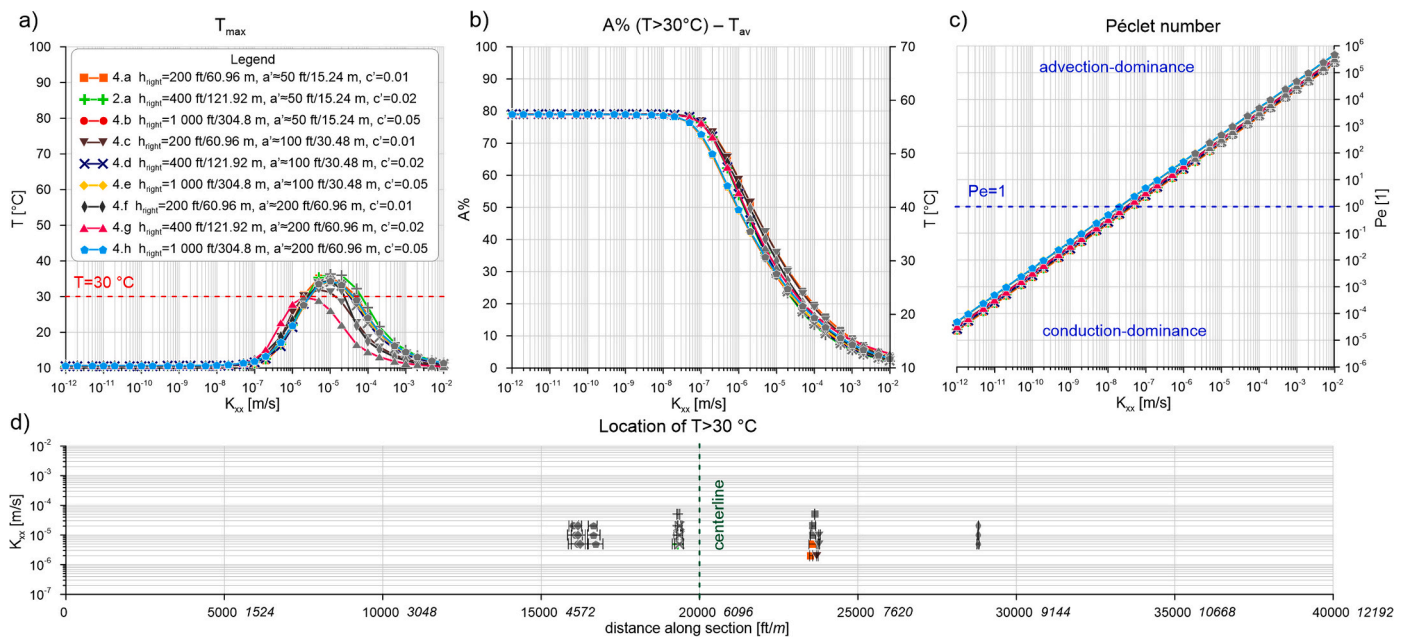

Fig. 4. Response parameters in model settings of 4.a, 2.a, 4.b, 4.c, 4.d, 4.e, 4.f, 4.g and 4.h. a) Maximum outflowing water temperature, b) area of the thermal water reservoir ($T > 30$ °C) in proportion to the whole model domain and average water temperature, c) Péclet number plotted against horizontal hydraulic conductivity and d) location and horizontal extent of thermal water ($T > 30$ °C) discharge. Scenarios with recharge>1 m/yr are indicated by grey colour.

varies from place to place. On the basin-scale, the presence of sedimentary cover and basin fill might be the most relevant. Note that effects of faults were studied in this context by several authors, e.g. Bauer et al. (2019); Jiang et al. (2018); López and Smith (1995); McKenna and Blackwell (2004); Wisian and Blackwell (2004). The omittance of faults and fault zones in these models was justified by detailed 3D numerical simulations which showed that faults have only a local impact on flow and temperature fields in basin-scale studies (Cherubini et al. 2013; Noack et al. 2013; Przybycin et al. 2017).

Two series of basin heterogeneities were examined in two basic basin geometries. The first case was the original Unit basin* + Composite basin and model 2.a was used as a reference for comparison of simulation results. A basin fill/sedimentary cover of $K_{xx} = 10^{-7}$ m/s was applied in 4 ways: half basin fill in the Unit basin* with a minimum thickness of 5000 ft. (1524 m) (model 5.a, Fig. B.16.), full basin fill in the Unit basin* (5.b, Fig. B.17.), semi-confining cover with a maximum thickness of 50 ft. (15.24 m) in the Composite basin (5.c, Fig. B.18.) and full basin fill in the Unit basin* + semi-confined situation in the Composite basin (5.d, Fig. B.19.) (for details, see Fig. 1. and Table A.1.).

The maximum temperature of discharging water max(T_{max}) was not more than ~35–40 °C and in the case of heterogeneous models, temperatures were generally higher than in the homogeneous medium. At the same time, the thermal water discharge also took place at higher K (approx. $>10^{-4}$ m/s) values compared to the reference model (2.a) (Fig. 5.a). In the presence of the basin fill sedimentary unit (models 5.a, 5.b and 5.d), a considerable increase was revealed in the minimum values of A% and T_{av}: from ~3% and ~12 °C to ~28% and ~26 °C. The semi-confined only situation (5.c) provided almost the same values as the reference model (2.a). The same plateau of both parameters appeared at ~79% of A% and ~58 °C of T_{av}, which were reached at K ≈ 5·10⁻⁸ m/s (Fig. 5.b). The Péclet number curve had different shapes for the heterogeneous cases: with a semi-confining cover, in cases of K lower than ~10^{-10} m/s, Pe exhibited ~$1.6 \cdot 10^{-2}$ instead of values of the reference line (2.a). The same phenomenon occurred in models with basin fill, but the minimum value of ~1.2 came at K ≈ 10^{-8} m/s. Because of the constant hydraulic conductivity of the basin fill and the semi-confining layer (K = 10^{-7} m/s), advection increased in the aforementioned domains (Fig. 5.c). Thermal water discharge on the surface

formed sharply along the centerline in the presence of basin fill (models 5.a, 5.b and 5.d) as groundwater was forced upward along the hydraulic barrier. There was only a slight rightward migration of the discharge location in model 5.c as the semi-confined cover weakened the groundwater flow from the right (Fig. 5.d).

The effects of basin heterogeneity were also examined in the model geometry of the flat Unit basin* part + Composite basin (model 3.d as reference) as it produced extreme discharging temperatures. Only two cases were simulated: half (model 6.a, Fig. B.20.) and full basin fill (6.b, Fig. B.21.) in the Unit basin* part. The maximum values of the maximum temperature of discharging water (T_{max}) were remarkably decreased by the sedimentary basin fill: the initial ~95 °C decreased to ~20 °C (Fig. 5. a). The portion of the thermal water reservoir (A% ($T > 30$ °C)) and average temperature (T_{av}) curves displayed values similar to the previous heterogeneous models (5.a, 5.b and 5.d) including minimum (~30% of A% and ~28 °C of T_{av}) and maximum values of both parameters (~79% of A% and ~58 °C of T_{av}) (Fig. 5.b). A slight negative departure in Péclet numbers was observed, when of K > 10^{-7} m/s due to the presence of basin fill with a hydraulic conductivity of 10^{-7} m/s, which decreased the intensity of groundwater flow in these cases. As there was no undulation and consequent driving force in the Unit basin* part, Pe reflected the reference values when K < 10^{-7} m/s (model 3.d) (Fig. 5.c). These heterogeneous scenarios did not produce thermal water discharge (Fig. 5.d).

Sedimentary basin fill, in general, based on the numerical simulation, served as a thermal blanket resulting in heat accumulation under and within this unit as the average temperature and the area of thermal water reservoir curves displayed. Hot water could be transported by advection along the hydraulic conductivity contrast (the boundary of basin fill) from the deeper part of the basin toward the surface, where thermal water discharge occurred. This phenomenon was reflected by higher T_{max} values (Fig. 5.c). In addition, advection remained dominant within the basin fill with constant hydraulic conductivity resulting in an enhanced Pe. The thermal blanketing effect of the basin fill was even more apparent in the flat Unit basin* part models (6.a and 6.b), where thermal water could not reach the surface but instead accumulated in the deeper regions. The extent of the basin fill, i.e. half or full, had an insignificant effect on the heat accumulation. The semi-confined
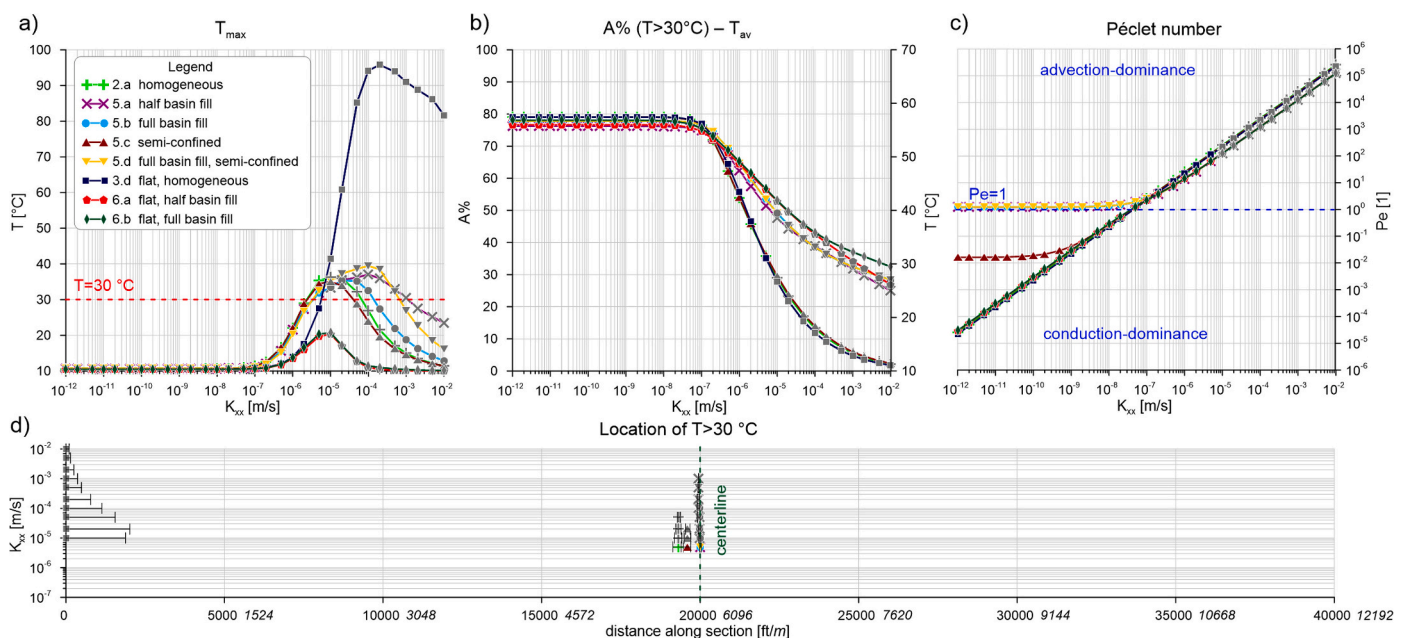

Fig. 5. Response parameters in model settings of 2.a, 5.a, 5.b, 5.c, 5.d, 3.d, 6.a and 6.b. a) Maximum outflowing water temperature, b) area of the thermal water reservoir ($T > 30$ °C) in proportion to the whole model domain and average water temperature, c) Péclet number plotted against horizontal hydraulic conductivity and d) location and horizontal extent of thermal water ($T > 30$ °C) discharge. Scenarios with recharge>1 m/yr are indicated by grey colour.

situation did not cause any significant changes on the flow and temperature fields by itself (5.c), however, in combination with full basin fill (5.d), it could slightly enhance T_{max} of the water discharge. As a general finding, sedimentary basin fill would result in heat accumulation in the deeper part of the basins in the advection-dominated regime. Owing to groundwater flow and advective heat transfer, the thermal water lifted to near-surface along the interface of the hydraulic conductivity barrier. This part of the basin had the highest theoretical geothermal potential, which was indicated by thermal springs, as well. Under and within the basin fill, there are further prospective areas but with lower intensity of flow and heat rejuvenation.

4.4. Extensional domain type geothermal plays

Apart from CV1 volcanic and CV2 plutonic type geothermal plays, ~10% of the worldwide geothermal development is related to CV3 extensional domain type plays. These regions formed during extensional tectonics, such as crustal extension, back-arc extension, pull-apart basin formation, intracontinental rifting, and including metamorphic core complexes are associated. Due to the extensional stress field, crustal thinning and mantle upwelling occur which act as the main heat source. Consequently, this play type is characterised by an elevated heat flow and high geothermal gradient (Faulds et al. 2010; Moeck 2014; Moeck and Beardsmore 2014). One typical form of the extensional domain play type is a range with elevated topography and an adjoining sedimentary basin. Hot springs might develop around the foothills indicating deep circulation of groundwater (Grasby and Hutcheon 2001), however, these geothermal plays are often "blind" without surface expression and thermal water resources are concealed (Moeck 2014). CV3 type plays can be found in Western Anatolia (Turkey) (Gokgoz et al. 2010; Özkaymak and Sözbilir, n.d; Özler 2000), along the East African Rift System, in Uganda (Kato 2016) and Kenya (Otieno 2020), in the Rhine Graben (Europe) (Rybach 2007; Schindler et al. 2010), in Mexico (Gutierrez-Negrin 2015; Gutiérrez-Negrín 2015; Prol-Ledesma and Morán-Zenteno 2019) and in the Great Basin region (Western USA) (Faulds et al. 2010; Faulds et al. 2006; Siler and Faulds 2013). The latter is the archetype of an extensional geothermal domain and these plays

are often referred to as Basin and Range type systems (Moeck 2014).

As these extensional domain type plays exhibit high basal heat flow, during this part of the simulation, elevated temperatures (150 °C, 195 °C, 240 °C and 285 °C) were imposed along the bottom boundary. A symmetric (models 7.a, 7.b, 7.c and 7.d, Figs. B.22–25.) and an asymmetric basin geometry (8.a, 8.b, 8.c and 8.d, Figs. B.26–29.) including a full basin fill (5.b and 6.b as reference models) were exposed to the aforementioned temperature conditions (Table A.1.). Maximum values of the maximum temperature of discharging water ($max(T_{max})$) certainly increased as the temperature of the bottom boundary increased: in the symmetric model set, ~35, ~48, ~60, ~72 and ~ 83 °C, and in the asymmetric case, ~20, ~25, ~30, ~35, ~40 °C were the maximum temperatures of outflowing groundwater. The symmetric model geometry produced thermal water within a wider hydraulic conductivity range (10^{-6}–10^{-3} m/s) compared to the asymmetric case ($5\cdot10^{-6}$–10^{-5} m/s) (Fig. 6.a). The portions of the thermal water reservoir (A%) curves show an increase with higher basal boundary temperatures: minima were 30–40% and maxima reached 85–92%. There was an upper limit of this parameter since cold freshwater infiltrated through the surface which was transported by advection in models of $K > 5\cdot10^{-8}$ m/s. However, in conduction-dominated cases ($K < 5\cdot10^{-8}$ m/s), only the near-surface basin part did not heat up above 30 °C (Fig. 6.b). Average temperature (T_{av}) values were not proportional to A% and these were plotted separately. Increasing the basal boundary temperature induced a higher T_{av}: in minima from ~30 °C to ~70 °C, in maxima from ~58 °C to ~145 °C. The model geometry of the flat Unit basin* part yielded higher average temperatures in the advection-dominated domain while a lower intensity of groundwater flow took place in absence of driving force in the left-hand side of the basin (Fig. 6.c). Péclet numbers were identical to the reference values (5.b and 6.b) because, based on the model assumptions, the temperature did not affect the flow conditions and the position of $Pe = 1$ was similar to and brought from the previous reference cases. The location of thermal water discharge was only controlled by the flow pattern and the hydraulic conductivity contrast, so hot water reached the surface along the centerline (Fig. 6.d).

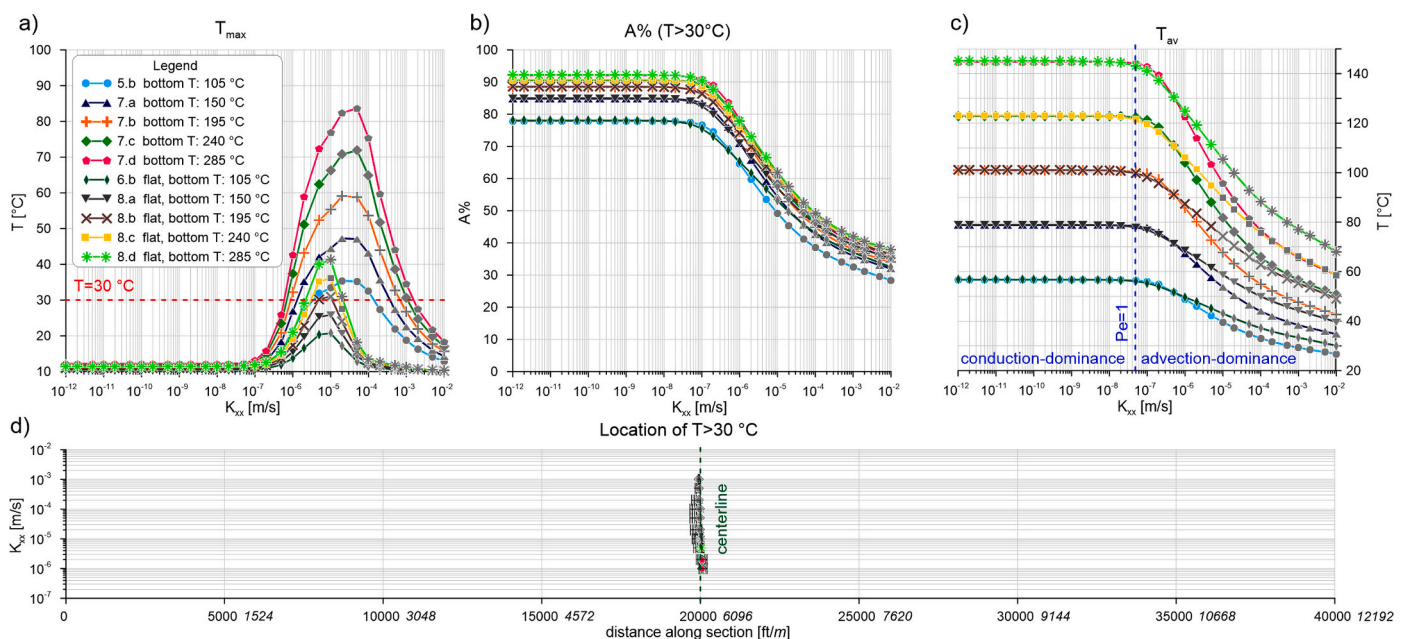Groundwater flow and heat transport were not fully coupled,

Fig. 6. Response parameters in model settings of 5.b, 7.a, 7.b, 7.c, 7.d, 6.b, 8.a, 8.b, 8.c and 8.d. a) Maximum outflowing water temperature, b) area of the thermal water reservoir ($T > 30\,°C$) in proportion to the whole model domain, c) average water temperature, indicating conduction- and advection-dominated domains, plotted against horizontal hydraulic conductivity and d) location and horizontal extent of thermal water (T > 30 °C) discharge. Scenarios with recharge>1 m/yr are indicated by grey colour.

therefore, temperature conditions and increasing basal boundary temperatures had no effect on the flow pattern in the investigated model cases. Response parameters reflected the increase in theoretical geothermal potential, however, prospective areas within the basin remained at the same places, i.e. along the centerline and under/within the basin fill unit. Consequently, one would need to drill to relatively shallower depths for reaching the same temperature in areas with a higher heat flow. In these circumstances, elevated temperatures would allow geothermal energy utilization for industrial purposes and electricity generation.

5. Case study of an extensional domain type geothermal play

Besides the above-listed examples, in Europe, the Pannonian Basin exhibits one of the most favorable temperature conditions to utilize geothermal energy (Cloetingh et al. 2010; Horváth et al. 2015; Lenkey et al. 2002; Limberger et al. 2018). This region is an integral part of the Alpine orogenic system with various terranes and a complex geologic–tectonic evolution (Csontos and Vörös 2004; Haas 2012; Handy et al. 2010; Horváth et al. 2015; Schmid et al. 2008). The back-arc basin

started to develop in the late Miocene, and it was formed by extensional processes and subsequent basin inversion. Attenuated crust and lithosphere characterize the area and, therefore, high heat flow (50–130 mW/m^2, on average 80–100 mW/m^2) and temperature gradient (40–50 °C/km) are present (Békési et al. 2018; Dövényi and Horváth 1988; Horváth et al. 2006; Horváth et al. 2015; Lenkey et al. 2002; Lenkey et al. 2017). On the basis of its tectonic settings and evolution and the catalog of Moeck (2014), the area can be categorized as a CV3 extensional domain type geothermal play. A selected "basin and range" part of the Pannonian Basin was investigated in the light of basin asymmetry, the occurrence of thermal springs and geothermal potential applying the same approach of numerical simulation of basin-scale groundwater flow and heat transport as in the synthetic models.

5.1. Study area

The local study area covered the Danube Basin – Transdanubian Range – Transdanubian Hills within the Hungarian part of the Pannonian Basin, and its groundwater flow conditions and geothermal resources were previously studied by many authors separately in the sub-
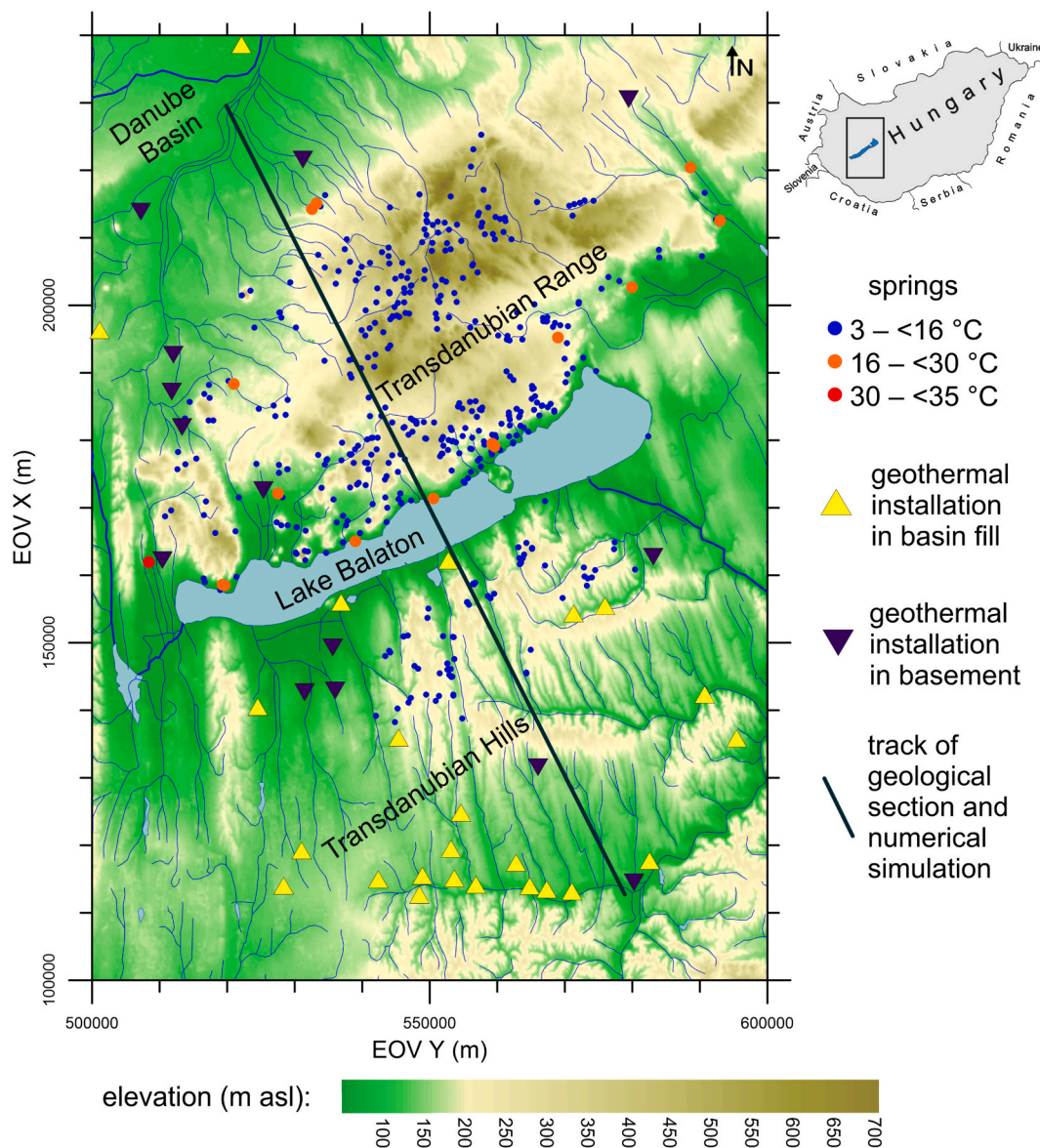

Fig. 7. Local study area in the Hungarian part of the Pannonian Basin. Geothermal installations were adapted from Horváth et al. (2015) and spring data from Izápy (2002).

areas (Lenkey et al. 2017; Nádor et al. 2019; Rman et al. 2020; Rman et al. 2015; Rotár-Szalkai et al. 2017; Tóth et al. 2016). The investigated area has a typical range plus sedimentary basin setting: elevation of the Transdanubian Range is 500–700 m asl, to the north, the Danube Basin is a relatively flat area at ~120 m asl, and to the south of Lake Balaton, the Transdanubian Hills has a hummocky terrain with an average

elevation of 180–200 m asl (Fig. 7). The mainly Triassic carbonate formations outcrop in the Transdanubian Range, while they become confined in area of the Danube Basin and Transdanubian Hills under a thick sedimentary basin fill unit (Fig. 8.a).

The presence of thermal water (T > 30 °C) is indicated by many geothermal installations located in the Transdanubian Hills and around
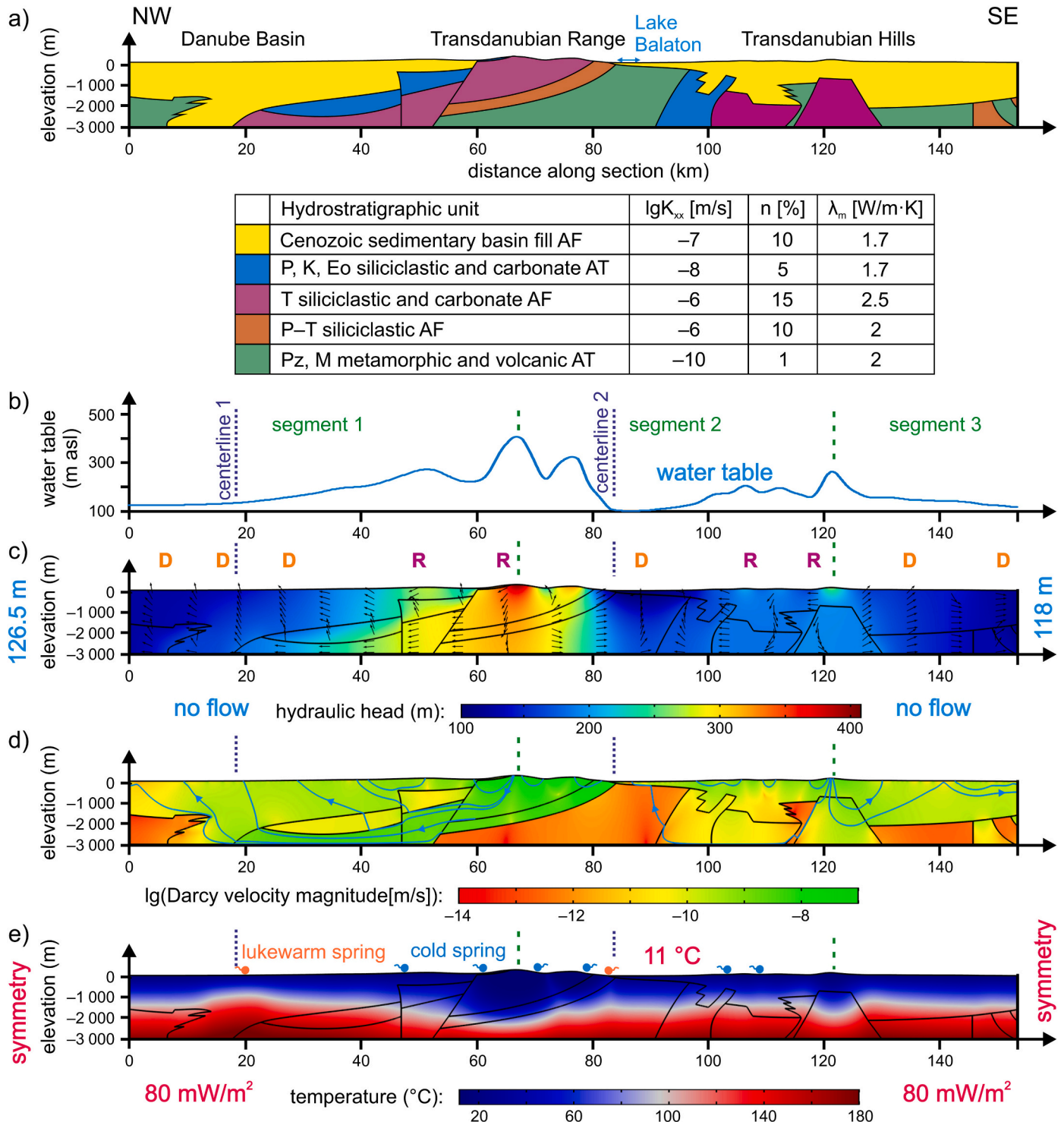

Fig. 8. Numerical simulation input and results of the local study area. a) Simplified geologic section across the Danube Basin – Transdanubian Range – Transdanubian Hills region and the properties of hydrostratigraphic units (AF: aquifer, AT: aquitard, K_{xx}: horizontal hydraulic conductivity, n: porosity, λ_m: thermal conductivity of matrix). b) Water table variation as upper boundary condition along the surface. c) Boundary conditions and the simulated flow pattern showing the hydraulic head and uniform Darcy velocity vector field. R: recharge, D: discharge d) Base 10 logarithm of Darcy velocity magnitude with characteristic streamlines. Calculated recharge rate: 217 mm/yr. e) Boundary conditions and the simulated temperature field with the position of springs.

the foothills of the Transdanubian Range. Thermal water is produced from either the carbonate basement or siliciclastic basin fill and is mainly used for balneological, heating, agricultural and industrial purposes (Horváth et al. 2015; Rman et al. 2020). Only a few of the ~500 springs yield naturally discharging water with an elevated temperature: ~3% have $T > 16\,°C$ and these lukewarm springs discharge around the foothills of the Transdanubian Range (Izápy 2002; Mádl-Szőnyi and Tóth 2015). Note that there is no surface indication of underground stored thermal water in the region of the Transdanubian Hills (Fig. 7). Overall, springs bear only low theoretical geothermal potential, however, on the basis of our synthetic numerical simulation series, considerable heat accumulation can be expected to occur in the deeper part of a heterogeneous basin.

5.2. Groundwater flow and heat transport simulation

To study the basin-scale groundwater flow patterns and their role in the distribution of geothermal resources, we performed numerical simulations along a regional section in this area (Fig. 7.). The main goal was to display and understand the groundwater pattern and temperature field in a basin-scale model to investigate possible interdependence between the sub-areas. Site-specific characteristics could not be resolved due to the resolution and this was also outside the scope of our study.

A regional, ~150 km long and ~3 km deep, section of Haas (2012) was generalized and simplified and the formations were converted into hydrostratigraphic units. Main lithology, age and properties of aquifers and aquitards (horizontal hydraulic conductivity, porosity and matrix thermal conductivity) were determined based on Mádl-Szőnyi et al. (2019); Rman et al. (2015); (Tóth, 2018); Tóth et al. (2016) (Fig. 8.a). The undulation of the water table was the driving force of groundwater flow which was specified as the upper boundary condition (Fig. 8.b). Hydrostatic flow conditions were assumed along the side walls, i.e. a constant hydraulic head of the corresponding water table level was applied. The bottom boundary was an artificial surface of the section at -3000 m asl elevation along which a no-flow boundary condition was imposed. This assumption could be valid, however, at this depth, the vertical downward component of groundwater flow could still be present but would be negligible (Fig. 8.c). For the simulation of heat transport, the annual mean air temperature ($11\,°C$) was fixed along the surface and a heat flow of $80\,mW/m^2$ was imposed at the bottom of the model. The lateral sides were symmetry boundaries, i.e. the temperature gradient across the boundary was zero (Fig. 8.d).

Basin-scale groundwater flow systems were driven by water table variations. Therefore, the Transdanubian Range and the central part of the Transdanubian Hills were recharge areas with some minor discharge areas embedded due to local hydraulic head differences. Most groundwater discharge occurred at areas with lower hydraulic heads, such as the northern foothills of the Transdanubian Range and farther in the Danube Basin, the lowland of the southern Transdanubian Hills and the area between these two elevated geographic regions, i.e. the basin of Lake Balaton. At the latter, concurrent opposing flow systems – one from the Transdanubian Range and the other from the Transdanubian Hills – had a common surface discharge area. The component coming from the north could have been more intense because of the higher water table gradient in the range and carbonate units. Nevertheless, due to the presence of a wedged regional metamorphic aquitard at the discharge area, the groundwater flow across this unit was limited.

The temperature distribution reflected the groundwater flow directions: contour lines were deflected downwards under the recharge areas indicating negative heat anomalies. Similarly, below discharge areas, high temperature values were closer to the surface as groundwater transported heat upwards generating positive heat anomalies. In

these places, significant heat accumulations could be observed under and within the sedimentary basin fill formations. There were no distinct surface manifestations of thermal water, as the near-surface part and temperature of discharging springs were usually cold. However, sporadically located lukewarm springs could receive warmer groundwater originating from the heat accumulations. The location and occurrence of these springs were controlled by the water table configuration and hydraulic conductivity contrast between hydrostratigraphic units.

5.3. Model comparison and interpretation

We tested our results of the numerical simulation of basin-scale groundwater flow and heat transport with a published data-driven evaluation and by comparing the results qualitatively to other models with higher resolution and more detailed parametrization (Békési et al. 2018; Lenkey et al. 2017; Tóth, 2018; Tóth et al. 2016). In general, the main features of the flow and temperature field, i.e. groundwater flow directions and heat anomalies, could be resolved by the regional model. Furthermore, hydraulic communication between sub-areas was also shown for the first time. Prospective areas for geothermal resources and shallow and deep energy utilization could be delineated and highlighted for further analyses.

However, the system's general behavior could be interpreted in terms of basin asymmetry, the occurrence of thermal springs and preliminary geothermal potential. The examined section could be divided into 3 segments representing asymmetric cases. Each segment exhibited a great variety of geological heterogeneity, notwithstanding, they could be simplified to obtain a basin geometry close to one of the synthetic cases. In this way, the simplified segment 1 resembled a model with a flat surface on one side (left) and hummocky terrain on the other (right) with a half basin fill and a geothermal gradient of 40–50 $°C/km$. Note that the half and full basin fill produced very similar response parameters, except for T_{av}. The synthetic model that most closely resembled the case study was model 8.a. For segment 2, two cases could be analogous: the water table variation suggested an asymmetric case with a higher hydraulic head on one side (model 4.b). But the presence of a regional aquitard around the centerline could restrict groundwater flow, so the water table difference might be balanced. In this case, and due to the elevated geothermal gradient, model 7.a could serve as a reference. Segment 3 is only a tiny part of the section, therefore, no investigation was performed. The present case study and synthetic models were compared based on their response parameters. For the segments, average values and parameters were calculated in COMSOL Multiphysics.

Response parameter values of synthetic and case study models were in the same order and slight differences could be explained by the complexity and site-specific characteristics of the case study model (Table 1., see Fig. 6. for comparison with other models). Therefore, the

Table 1
Response parameter values of synthetic and case study models for the assigned segments.

	Segment 1		Segment 2	
	Model 8.a	Case study	Model 7.a	Case study
$\overline{K_{xx}}$ (m/s)	$4\cdot10^{-7}$		$3.5\cdot10^{-7}$	
T_{max} (°C)	12	16	16	18
A% (T > 30 °C)	77.5	84	78	86
T_{av} (°C)	73	85	74	83
Pe	6	5.5	5.5	3.6

symmetric and asymmetric synthetic groundwater basin models were able to predict the temperature conditions in general with the help of the applied response parameters. These simplified basin-scale models of groundwater flow and heat transport could serve as a conceptual background and starting point in preliminary geothermal potential assessment and delineation of prospective areas. Recognition of basic behavior and pattern of processes and the parameters as highlighted above, could support the understanding of other study areas.

6. Discussion

Heat as an elemental component of a geothermal system is transported by conduction and underground fluid flow which is generally controlled by the water table configuration within a groundwater basin. The occurrence of thermal springs, as a surface manifestation of heat transport, can be a preliminary indicator of underground geothermal resources. Their development has generally been conceptualized as in-the-fault-plane circulation of hot water and the importance of local permeability changes, conduit faults, fault zones and fractures has been highlighted (Andrews et al. 1982; Bredehoeft 1997; Celico et al. 2006; Forster and Smith 1989). On the other hand, implementation of faults in basin-scale numerical models is not necessary to reproduce the temperature field, but the presence and hydraulic behavior (conduit or barrier) of faults and their influence on the temperature distribution might be locally relevant in reservoir-scale models (Cherubini et al. 2014; Przybycin et al. 2017). Basin-scale models, in addition, can reveal the position of faults in the regional flow field and their role can be evaluated accordingly as they might behave differently within the various hydraulic regimes (i.e. recharge, through-flow and discharge) of a groundwater basin (Tóth and Sheng 1996). Some of the previous studies applied basin-scale models with identical basin-halves and revealed the operation and efficiency of topography-driven groundwater flow in temperature distribution (Jiang et al. 2018; López and Smith 1995; McKenna and Blackwell 2004; Wisian and Blackwell 2004). Relevance and significance of groundwater flow even in the reservoir-scale prediction of geothermal development possibilities has been underlined, however, it has rarely been taken into account (Bauer et al. 2019).

Therefore, basin-scale numerical simulations of groundwater flow and heat transfer were performed in symmetric and asymmetric synthetic cases which can be considered as simplified representations of a selection of real systems. Our simulation series revealed the effects of anisotropy, asymmetry of the topographical driving force of groundwater flow, basin heterogeneity and basal temperature on heat accumulation, location of thermal spring discharge and prevailing mechanisms of heat transfer. Therefore, application of basin-scale models in preliminary geothermal potential assessment would be beneficial for understanding heat distribution. The results also have further implications on the interplay between basin-parts and rejuvenation of geothermal resources.

6.1. Asymmetric flow pattern – Basin interplay

In identical basin-halves, exactly the same flow pattern develops and there is no flow from one part to the other. However, this ideal situation is not the case in real groundwater basins. A symmetrical setting here refers to a basin exhibiting the same value of hydraulic head maxima acting as a driving force for groundwater flow at the water divides (same regional hydraulic gradients), but the water table configuration can be different. In an asymmetric case, the surface undulation, as well as the

hydraulic head gradients are different over the basin. As there are no identical groundwater basin-halves, symmetrical cases might occur but asymmetric basins are abundantly widespread, so consequently, a complex asymmetric flow pattern can evolve in real cases.

Groundwater flow from one basin(−part) to another is described as interbasin flow, a general form of basin interplay (e.g. Carrillo-Rivera (2000); Gillespie et al. (2012); Welch et al. (2007); Ye et al. (2016)). This process is a direct consequence of basin asymmetry since waters enter a territory of another flow system due to the differences in driving forces and/or geographic position. At the convergence of opposing flow systems under a discharge area, quasi-stagnant zones and hydraulic traps may develop and support heat and dissolved matter accumulation (Anderson and Munter 1981; Jiang et al. 2012; Jiang et al. 2011; Tóth 1987).

An asymmetric flow pattern was revealed in the area of Budapest, Hungary, which is situated at the boundary of confined and unconfined carbonates. The distinct water table position of the two basin-halves and the presence of sedimentary basin fill over the thick carbonate sequence are responsible for heat accumulation and thermal water discharge and can explain the favorable geothermal conditions (Mádl-Szőnyi and Tóth 2015). A similar flow pattern was identified near the city of Jinan, China (Wang et al. 2016; Yang et al. 2017). Synthetic model 7.a is applicable for these cases (both Budapest and Jinan) and occurrence of 40–50 °C thermal springs in a highly permeable carbonate environment can be inferred. As a consequence, an asymmetric flow field in combination with basin fill sedimentary cover can facilitate the formation of considerable heat accumulations which can be tapped by geothermal systems.

6.2. Geothermal plays and their rejuvenation

The presented approach and synthetic study of theoretical geothermal potential assessment can be applied to any range and adjoining sedimentary basin settings. However, as topographical variations exist everywhere and groundwater flow cannot be excluded, the concept might be adapted to any kind of geothermal plays. A basin-scale hydrogeological study is, therefore, recommended to map prospective areas of geothermal development and avoid dry/cold wells.

Furthermore, groundwater flow systems and their carrier fluids provide a continuous natural replenishment of geothermal systems. In an extensional, "basin and range" type setting, asymmetric flow and temperature fields evolve due to hydraulic head differences and interbasin flow occurs, while mountain-block recharge takes place. Mountain-block recharge is essentially the subsurface groundwater contribution from a topographically elevated area to the adjoining lowland sedimentary aquifers, which can receive 5–50% of their total recharge from the mountain block (Markovich et al. 2019; Wilson and Guan 2004). The role of mountain-block recharge is relevant and important in maintaining groundwater flow systems and related heat accumulation in the basin fill part of an area. Thus, the rejuvenation of a geothermal system is provided by natural topography-driven regional groundwater flow both on a human and a geological time scale. The natural rejuvenation processes, however, could be modified (enhanced/restricted) by structural settings, resulting in geothermal reservoirs without fluid and heat replenishment as these processes are dependent on several factors, such as hydraulic properties of the medium, natural recharge rate and production rate (Mádl-Szőnyi et al. 2019).

If the production of a geothermal system exceeds the rate of replenishment, reinjection of carrier fluids might be a solution for long-term sustainable operation (Rivera Diaz et al. 2016). The related

possibilities are determined by hydrogeological processes, the vertical component of groundwater flow and fluid dynamic parameters (Mádl-Szőnyi and Simon 2016). These conditions can be evaluated prior to the actual development and the applied techniques include simple basin-scale hydrogeological simulation and flow pattern analysis and even detailed processing of pressure data. Then, appropriate reinjection intervention can be planned or requested for sustainable production of geothermal resources as in some countries, reinjection is mandatory for all hot sedimentary aquifers due to environmental legislation. Analysis of the basin-scale flow patterns, heat accumulation and natural recharge could also be implemented during the reconnaissance phase of exploration.

6.3. Model limitations

Limitations of the applied study approach and their implications on the results are addressed in this section. 1) Subsurface fluid and heat flow are generally 3D problems. However, 2D numerical models can also capture the systems' main behavior and reveal hydraulic and thermal processes along the main hydraulic gradient. These can be a valuable tool for regional-scale interpretation and target areas for local-scale high-resolution 3D models can be identified. 2) All simulations assume constant fluid density and viscosity. However, some model sets include high temperature differences between the basal and upper boundaries (up to 275 °C over ~3 km) and high hydraulic conductivities (in case of 10^{-5}–10^{-2} m/s), thus one might expect significant thermal buoyancy effects. In these cases, heat transfer and groundwater flow should be fully coupled, i.e. fluid density and changes due to temperature variations could act as a driving force in the form of free thermal convection resulting in mixed convection. A recent study showed that in the presence of topography-driven groundwater flow, free thermal convection might occur only at higher Rayleigh numbers (Szijártó et al. 2019). For the purposes of this paper, constant fluid density and viscosity can be acceptable assumptions but time-dependent solutions of the fully coupled equations indicate the way forward. 3) Time is also important in the rejuvenation of geothermal reservoirs. Steady-state models do not include transient effects. For proper characterization of rejuvenation processes, transient models are required taking into consideration the natural recharge rate and time-dependent variation of flow and temperature fields. 4) Related to the previous point, instead of a water table boundary condition along the upper surface, recharge could be prescribed to represent replenishment from precipitation. There is an active debate regarding applying a fixed water table versus fixed recharge rate as the upper boundary condition (Bresciani et al. 2016). For realistic, quantitative calculations, a recharge rate should be applied as a boundary condition. However, in case of understanding basin-scale processes and flow patterns, applying specific hydraulic heads as the boundary condition is still a reasonable assumption if the computed recharge is realistic. Very low recharge rates under the low hydraulic conductivity scenarios ($K < 10^{-9}$ m/s) can be accepted. However, in the high hydraulic conductivity cases ($K > 10^{-5}$ m/s) the imposed water table shapes could never occur, those would require unrealistically high recharge (>1 m/yr). Thus these model sets were flagged on the plots (Figs. 3–6.). 5) Hydraulic and thermal conditions imposed on the boundaries of the models might have an impact on the simulation results. Other types of boundary conditions (e.g. constant hydraulic head along the sides, thermally open boundary, constant basal heat flux) might be tested and applied in specific hydrogeological situations. 6) By focusing on the influence of steady-state regional topography induced groundwater flow, other parameters of influence on the temperature

distribution were kept constant or not taken into account (such as porosity, thermal conductivity, the heat capacity of pore water and rock, heat production). The effects of these parameters can also be evaluated by a series of sensitivity studies but the influence on basin-wide temperature distribution would be minor or negligible. These parameters generally have site-specific values, thus they might be relevant in case studies. 7) Recent studies revealed linear and exponential or more complex decay of hydraulic conductivity with depth due to compaction/ diagenesis (Cardenas and Jiang 2010; Chen et al. 2020; Ehrenberg and Nadeau 2005; Zlotnik et al. 2011). This phenomenon could affect the large-scale flow and thus the temperature pattern. 8) Finally, there is an infinite number of topographical variations in real-life basins. These selected model geometries might describe the general flow pattern and hydrogeological processes of a certain area with similar settings, at least, they serve as a basic background in interpreting basin-scale groundwater flow and further studies might be triggered for detailed characterization.

7. Summary and conclusions

Fluid, as an elemental component of a geothermal system, transports and distributes underground heat according to the topographic driving force within a groundwater basin. As the water table configuration has diverse and distinct forms in real-life basins, asymmetric hydraulic head variation may occur from basin to basin in accordance with real physiographic characteristics. Therefore, the effects of an asymmetric water table distribution in groundwater basins were investigated in several model sets with special emphasis on the temperature field and with the help of five response parameters: maximum temperature of outflowing water, average temperature, the portion of the thermal water reservoir, Péclet number and location and extent of thermal water discharge.

Theoretical geothermal potential, i.e. heat in place, is often assessed based on occurrence, temperature and hydrochemistry of thermal springs. However, in case of blind geothermal systems, such as extensional domain type plays, there is no surface expression of a heat accumulation underground. Our simulation results showed that in the absence of thermal springs, the extent of the thermal water reservoir might be larger and the temperatures might be higher. Sedimentary basin fill fosters the formation of heat accumulation under and within this unit, but its extent, i.e. half or full, had an insignificant influence on the temperature pattern. As a new "parameter" in the basin-scale groundwater and geothermal studies, basin asymmetry was introduced which has a critical role in discharge and accumulation patterns, thus it controls the location of basin parts bearing the highest geothermal potential. So if thermal water can reach the ground surface, the discharge might not take place exactly above the thermal water reservoir due to the asymmetric driving forces of groundwater flow. Furthermore, the extent and temperature of thermal water reservoirs are also influenced by local-scale anisotropy, heterogeneities, i.e. faults, fault zones and fractures, and, of course, basal heat flux.

Our study on the effects of these factors shows the likely basin-scale pattern of heat transport (conductive and advective) and accumulation for extensional domain type geothermal plays. These regions are prospective targets for geothermal energy utilization and exhibit a typical "basin and range" setting: a topographically elevated block and an adjoining sedimentary basin. For this type of model geometry, our models indicate basin interplay or interbasin flow between the basin-parts, caused by an asymmetric distribution of the water table. This process is crucial in rejuvenation, i.e. continuous fluid replenishment, of thermal water reservoirs, since the range serves as a recharge area for

the adjacent sedimentary basin. In this advection-dominated flow field, sustainable exploitation of geothermal energy resources is assisted by natural topography-driven regional groundwater flow systems, which are present and active everywhere and at any time.

The significance of basin-scale regional groundwater flow and asymmetry of driving forces, as a new aspect, on preliminary geothermal potential assessment was demonstrated by synthetic and a real-life case of an extensional domain type geothermal play in Hungary. During the reconnaissance phase of exploration, a conceptual, generalized and simplified groundwater flow and heat transport model can support the identification of prospective areas. The presented preliminary numerical interpretation of the influencing factors also provides a good starting point for realistic 3D models for planning of shallow and deep geothermal energy utilization, also concerning reinjection possibilities. In conclusion, the scope of "geothermal hydrogeology" is to analyze and explain the basin-scale flow pattern and heat accumulation (including hydraulic traps and stagnation zones, groundwater flow direction and intensity, recharge and discharge areas), in addition to the occurrence of possible thermal springs. It is also critical to determine the rates and pathways of natural fluid replenishment recharging from the surrounding elevated areas, and mainly, to delineate hydrogeologically favorable regions for sustainable long-term geothermal energy exploitation.

Declaration of Competing Interest

The authors declare that they have no known competing financial

interests or personal relationships that could have appeared to influence the work reported in this paper.

Appendix A

A.1. Appendix A

Table A.1

Geometric and geologic parameters of the simulated synthetic groundwater basins (see Fig. 1. for the explanation). Symmetry refers to the regional topographical driving force of groundwater, S – symmetric ($h_{left} = h_{right}$) and A – asymmetric basins.

Model ID	Unit basin* (left)				Composite basin (right)					Symmetry	Medium	Basal boundary T [°C]
	w_0 [ft]	a [ft]	b [1/ft]	h_{left} [ft]	z_0 [ft]	a' [ft]	b' [1/ft]	c'	h_{right} [ft]			
1	10,200	200	$\frac{2\pi}{40,000}$	400	10,000	50.01000200	0.0012568914	0.02	400	S	Homogeneous isotropic	105
2.a	10,200	200	$\frac{2\pi}{40,000}$	400	10,000	50.01000200	0.0012568914	0.02	400	S	Homogeneous anisotropic, $\varepsilon = 10$	105
2.b	10,200	200	$\frac{2\pi}{40,000}$	400	10,000	50.01000200	0.0012568914	0.02	400	S	Homogeneous anisotropic, $\varepsilon = 100$	105
2.c	10,200	200	$\frac{2\pi}{40,000}$	400	10,000	50.01000200	0.0012568914	0.02	400	S	Homogeneous anisotropic, $\varepsilon = 1\,000$	105
3.a	10,150	150	$\frac{2\pi}{40,000}$	300	10,000	50.01000200	0.0012568914	0.02	400	A	Homogeneous anisotropic, $\varepsilon = 10$	105
3.b	10,100	100	$\frac{2\pi}{40,000}$	200	10,000	50.01000200	0.0012568914	0.02	400	A	Homogeneous anisotropic, $\varepsilon = 10$	105
3.c	10,050	50	$\frac{2\pi}{40,000}$	100	10,000	50.01000200	0.0012568914	0.02	400	A	Homogeneous anisotropic, $\varepsilon = 10$	105
3.d	10,000	0	0	0	10,000	50.01000200	0.0012568914	0.02	400	A	Homogeneous anisotropic, $\varepsilon = 10$	105
4.a	10,200	200	$\frac{2\pi}{40,000}$	400	10,000	50.00250012	0.0012567028	0.01	200	A	Homogeneous anisotropic, $\varepsilon = 10$	105
4.b	10,200	200	$\frac{2\pi}{40,000}$	400	10,000	50.06247797	0.0012582102	0.05	1000	A	Homogeneous anisotropic, $\varepsilon = 10$	105
4.c	10,200	200	$\frac{2\pi}{40,000}$	400	10,000	100.00500024	0.0012567028	0.01	200	A	Homogeneous anisotropic, $\varepsilon = 10$	105
4.d	10,200	200	$\frac{2\pi}{40,000}$	400	10,000	100.02000400	0.0012568914	0.02	400	S	Homogeneous anisotropic, $\varepsilon = 10$	105

Table A.1 (*continued*)

Model ID	Unit basin* (left)				Composite basin (right)					Symmetry	Medium	Basal boundary T [°C]
	w_0 [ft]	a [ft]	b [1/ft]	h_{left} [ft]	z_0 [ft]	a' [ft]	b' [1/ft]	c'	h_{right} [ft]			
4.e	10,200	200	$\frac{2\pi}{40,000}$	400	10,000	100.12495594	0.0012582102	0.05	1000	A	Homogeneous anisotropic, $\varepsilon = 10$	105
4.f	10,200	200	$\frac{2\pi}{40,000}$	400	10,000	200.0100048	0.0012567028	0.01	200	A	Homogeneous anisotropic, $\varepsilon = 10$	105
4.g	10,200	200	$\frac{2\pi}{40,000}$	400	10,000	200.040008	0.0012568914	0.02	400	S	Homogeneous anisotropic, $\varepsilon = 10$	105
4.h	10,200	200	$\frac{2\pi}{40,000}$	400	10,000	200.24991188	0.0012582102	0.05	1000	A	Homogeneous anisotropic, $\varepsilon = 10$	105
5.a	10,200	200	$\frac{2\pi}{40,000}$	400	10,000	50.01000200	0.0012568914	0.02	400	S	Half basin fill left ($K_{xx} = 10^{-7}$ m/s) anisotropic, $\varepsilon = 10$	105
5.b	10,200	200	$\frac{2\pi}{40,000}$	400	10,000	50.01000200	0.0012568914	0.02	400	S	Full basin fill left ($K_{xx} = 10^{-7}$ m/s) anisotropic, $\varepsilon = 10$	105
5.c	10,200	200	$\frac{2\pi}{40,000}$	400	10,000	50.01000200	0.0012568914	0.02	400	S	Semi-confined right ($K_{xx} = 10^{-7}$ m/s) anisotropic, $\varepsilon = 10$	105
5.d	10,200	200	$\frac{2\pi}{40,000}$	400	10,000	50.01000200	0.0012568914	0.02	400	S	Full basin fill left semi-confined right ($K_{xx} = 10^{-7}$ m/s) anisotropic, $\varepsilon = 10$	105
6.a	10,000	0	0	0	10,000	50.01000200	0.0012568914	0.02	400	A	Half basin fill left ($K_{xx} = 10^{-7}$ m/s) anisotropic, $\varepsilon = 10$	105
6.b	10,000	0	0	0	10,000	50.01000200	0.0012568914	0.02	400	A	Full basin fill left ($K_{xx} = 10^{-7}$ m/s) anisotropic, $\varepsilon = 10$	105
7.a	10,200	200	$\frac{2\pi}{40,000}$	400	10,000	50.01000200	0.0012568914	0.02	400	S	Full basin fill left ($K_{xx} = 10^{-7}$ m/s) anisotropic, $\varepsilon = 10$	150
7.b	10,200	200	$\frac{2\pi}{40,000}$	400	10,000	50.01000200	0.0012568914	0.02	400	S	Full basin fill left ($K_{xx} = 10^{-7}$ m/s) anisotropic, $\varepsilon = 10$	195
7.c	10,200	200	$\frac{2\pi}{40,000}$	400	10,000	50.01000200	0.0012568914	0.02	400	S	Full basin fill left ($K_{xx} = 10^{-7}$ m/s) anisotropic, $\varepsilon = 10$	240
7.d	10,200	200	$\frac{2\pi}{40,000}$	400	10,000	50.01000200	0.0012568914	0.02	400	S	Full basin fill left ($K_{xx} = 10^{-7}$ m/s) anisotropic, $\varepsilon = 10$	285
8.a	10,000	0	0	0	10,000	50.01000200	0.0012568914	0.02	400	A	Full basin fill left ($K_{xx} = 10^{-7}$ m/s) anisotropic, $\varepsilon = 10$	150
8.b	10,000	0	0	0	10,000	50.01000200	0.0012568914	0.02	400	A	Full basin fill left ($K_{xx} = 10^{-7}$ m/s) anisotropic, $\varepsilon = 10$	195
8.c	10,000	0	0	0	10,000	50.01000200	0.0012568914	0.02	400	A	Full basin fill left ($K_{xx} = 10^{-7}$ m/s) anisotropic, $\varepsilon = 10$	240
8.d	10,000	0	0	0	10,000	50.01000200	0.0012568914	0.02	400	A	Full basin fill left ($K_{xx} = 10^{-7}$ m/s) anisotropic, $\varepsilon = 10$	285

Applied parameter values in m in ascending order: 50 ft. = 15.24 m, 50.01000200 ft. = 15.24305 m, 100 ft. = 30.48 m, 100.00500024 ft. = 30.48152 m, 150 ft. = 45.72 m, 200 ft. = 60.96 m, 200.24991188 ft. = 61.03617 m, 300 ft. = 91.44 m, 400 ft. = 121.92 m, 1000 ft. = 304.8 m, 10,000 ft. = 3048 m, 10,050 ft. = 3063.24 m, 10,100 ft. = 3078.48 m, 10,150 ft. = 3093.72 m, 10,200 ft. = 3108.96 m.

A.2. Appendix B

Hydraulic head and temperature field with Darcy velocity streamlines are displayed in all models at $K = 10^{-6}$ m/s of horizontal hydraulic conductivity.
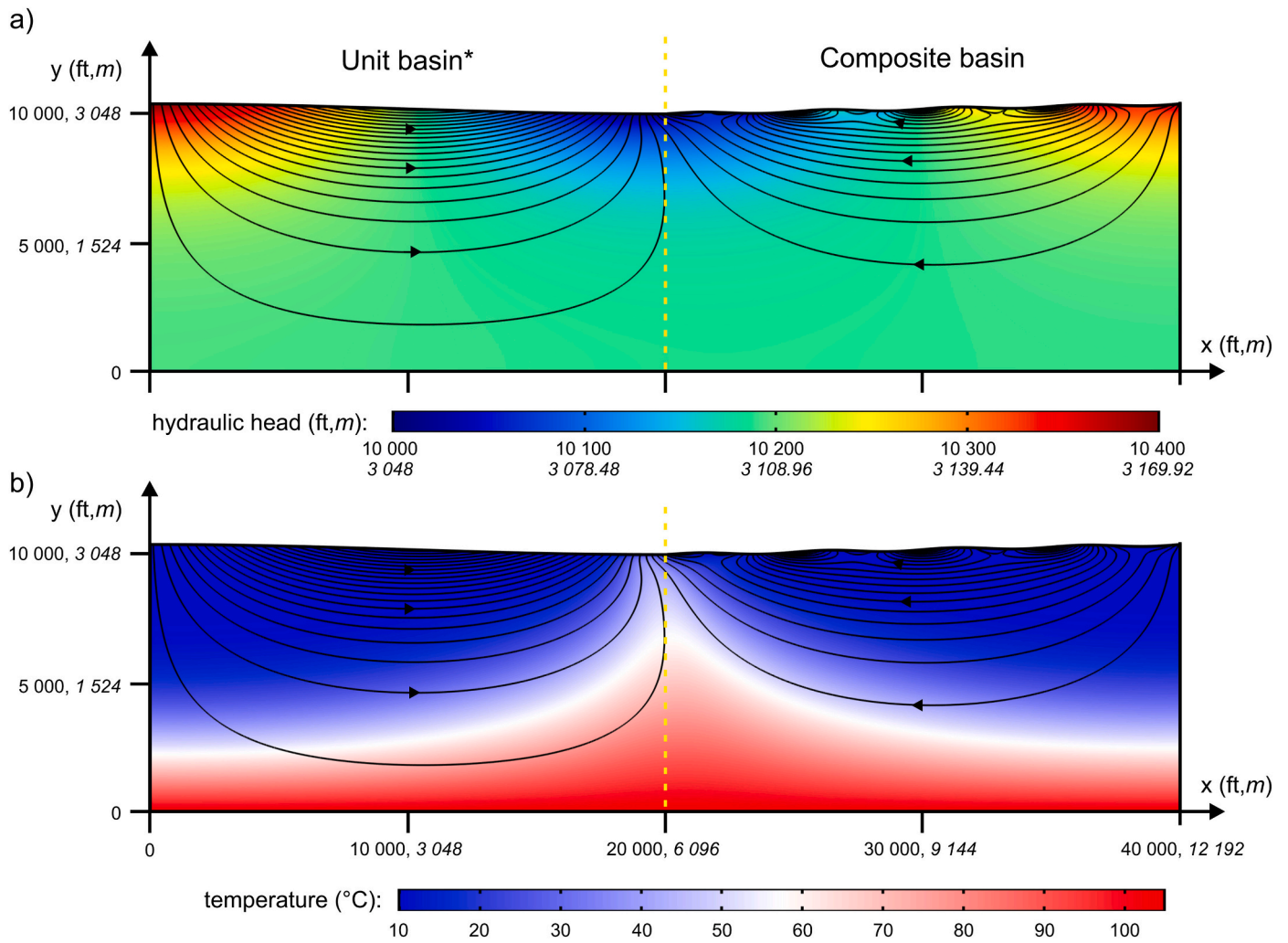
Model 1 was presented in Fig. 2.

Fig. B.1. Simulation results of model 2.a: $\varepsilon = 10$ a) Hydraulic head distribution and b) Temperature field with magnitude controlled streamlines. Calculated recharge rate: 175 mm/yr, maximum of Darcy velocity magnitude: $1.49 \cdot 10^{-7}$ m/s, number of streamlines: 20. Centerline is represented by the yellow dashed line. (For interpretation of the references to colour in this figure legend, the reader is referred to the web version of this article.)
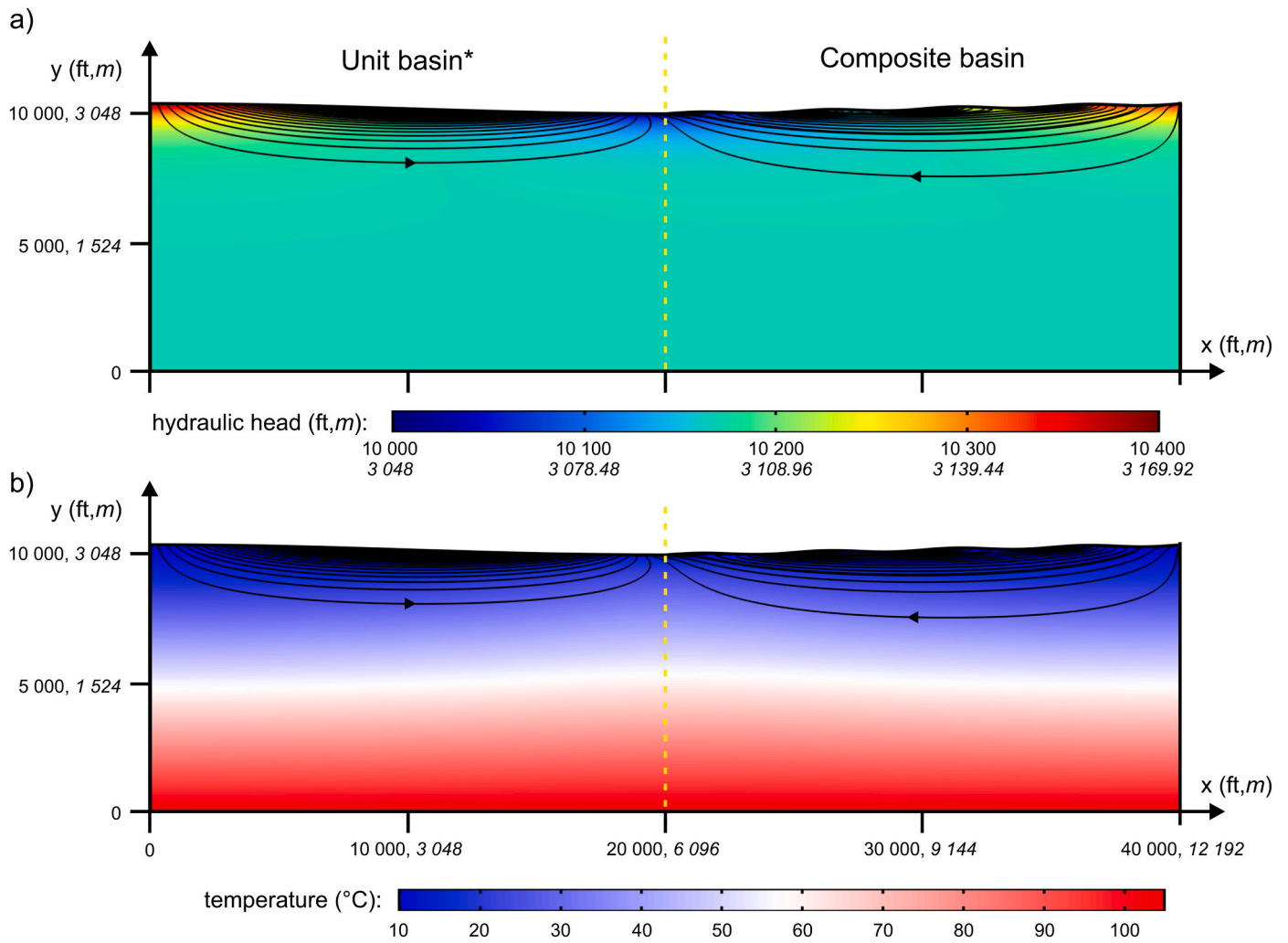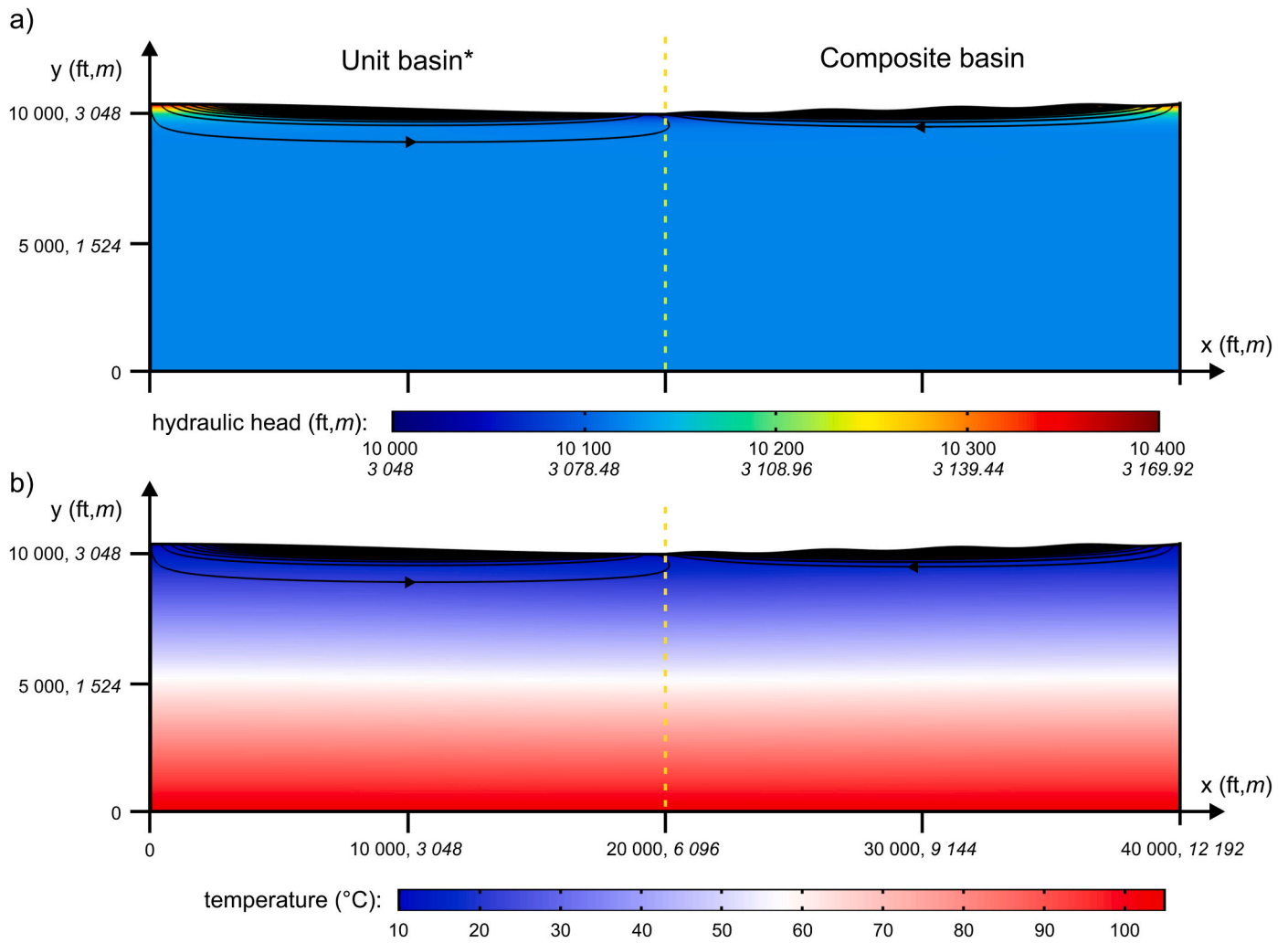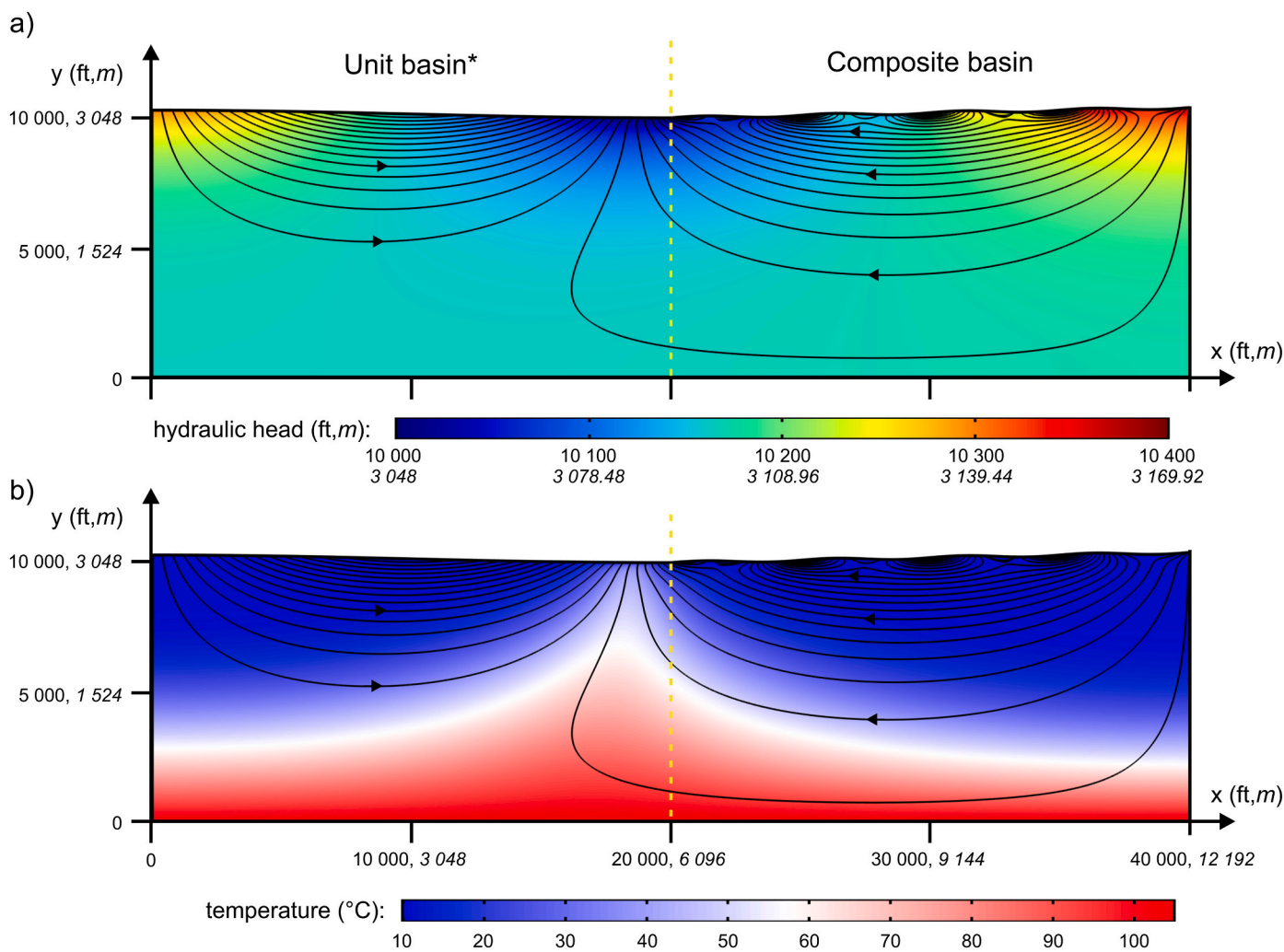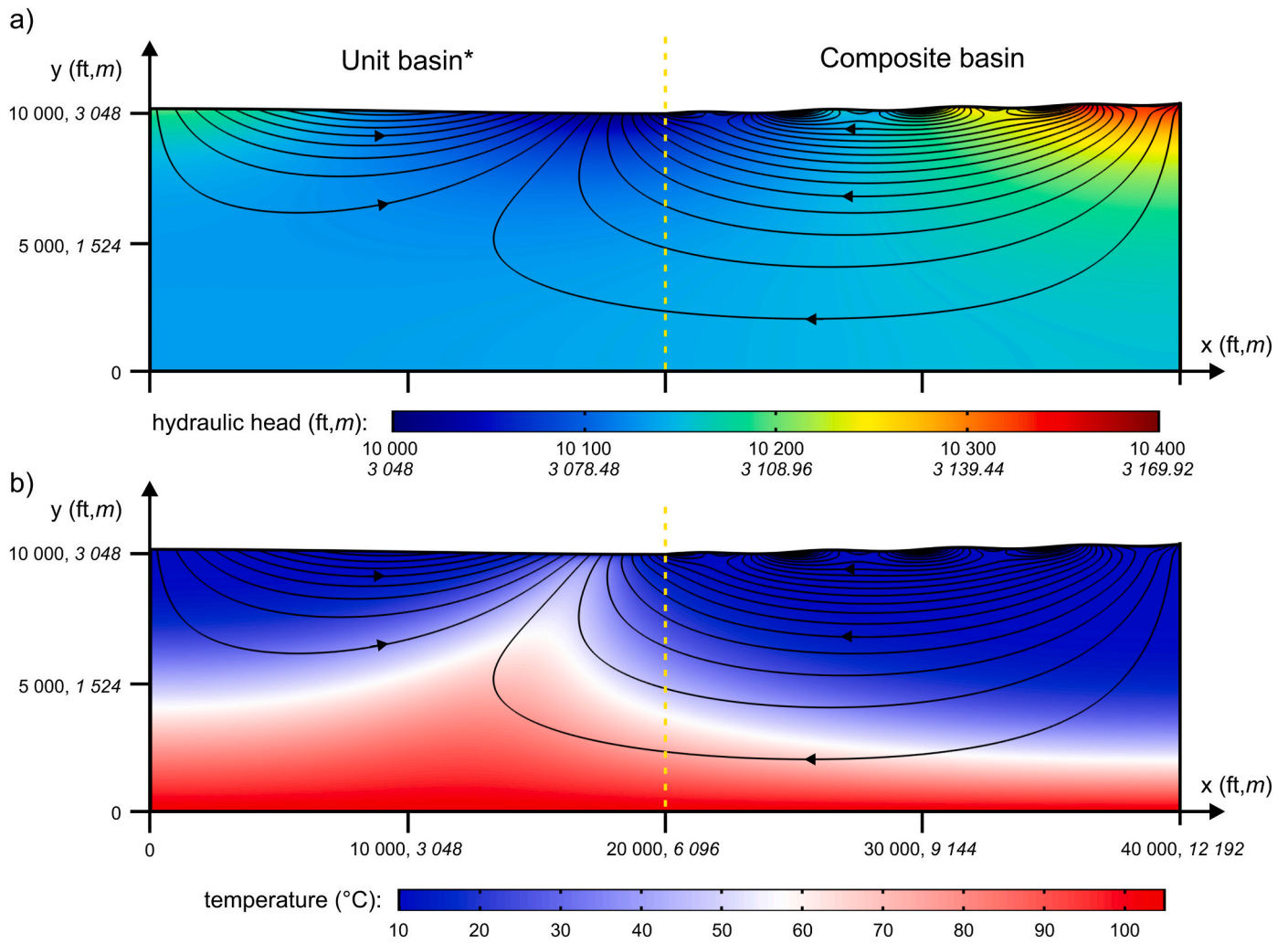
a)

b)

Fig. B.2. Simulation results of model 2.b: $\varepsilon = 100$ a) Hydraulic head distribution and b) Temperature field with magnitude controlled streamlines. Calculated recharge rate: 64 mm/yr, maximum of Darcy velocity magnitude: $2.47 \cdot 10^{-7}$ m/s, number of streamlines: 20. Centerline is represented by the yellow dashed line. (For interpretation of the references to colour in this figure legend, the reader is referred to the web version of this article.)
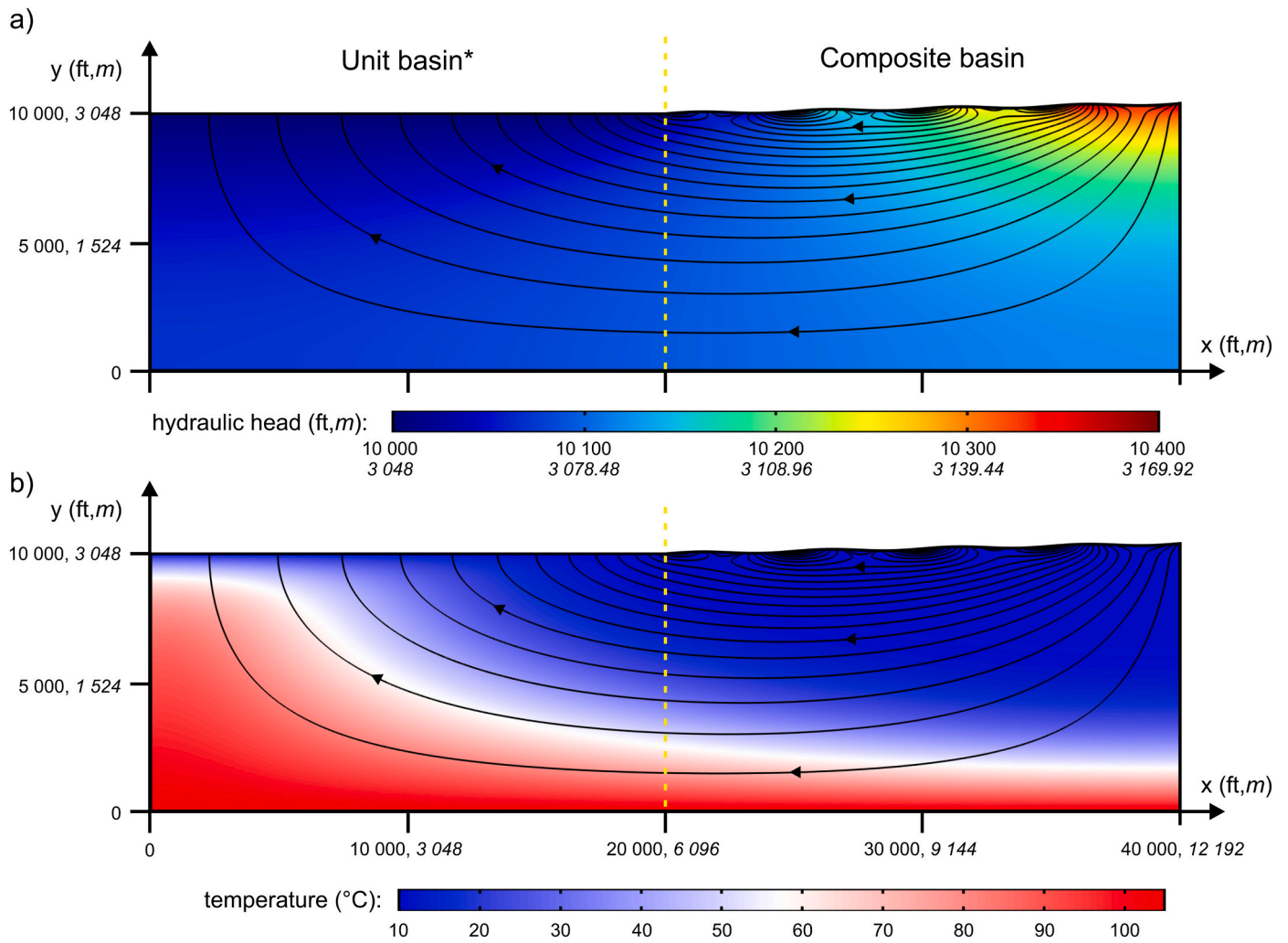
a)

b)

Fig. B.3. Simulation results of model 2.c: $\varepsilon = 1000$ a) Hydraulic head distribution and b) Temperature field with magnitude controlled streamlines. Calculated recharge rate: 17 mm/yr, maximum of Darcy velocity magnitude: $3.4 \cdot 10^{-7}$ m/s, number of streamlines: 20. Centerline is represented by the yellow dashed line. (For interpretation of the references to colour in this figure legend, the reader is referred to the web version of this article.)
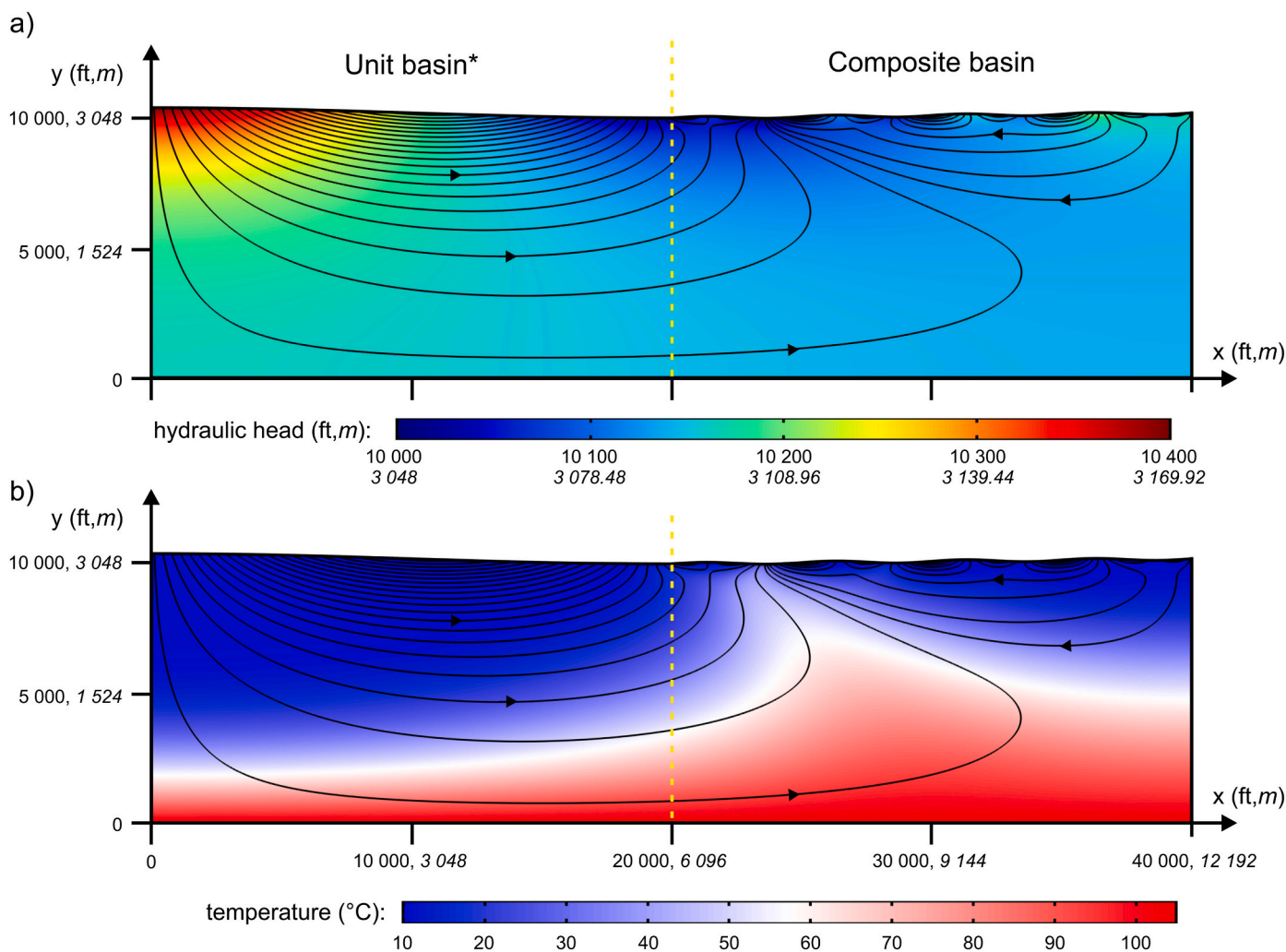
Fig. B.4. Simulation results of model 3.a: $h_{left} = 300$ ft./91.44 m a) Hydraulic head distribution and b) Temperature field with magnitude controlled streamlines. Calculated recharge rate: 162 mm/yr, maximum of Darcy velocity magnitude: $1.47 \cdot 10^{-7}$ m/s, number of streamlines: 20. Centerline is represented by the yellow dashed line. (For interpretation of the references to colour in this figure legend, the reader is referred to the web version of this article.)

Fig. B.5. Simulation results of model 3.b: $h_{left} = 200$ ft./60.96 m a) Hydraulic head distribution and b) Temperature field with magnitude controlled streamlines. Calculated recharge rate: 150 mm/yr, maximum of Darcy velocity magnitude: $1.45 \cdot 10^{-7}$ m/s, number of streamlines: 20. Centerline is represented by the yellow dashed line. (For interpretation of the references to colour in this figure legend, the reader is referred to the web version of this article.)
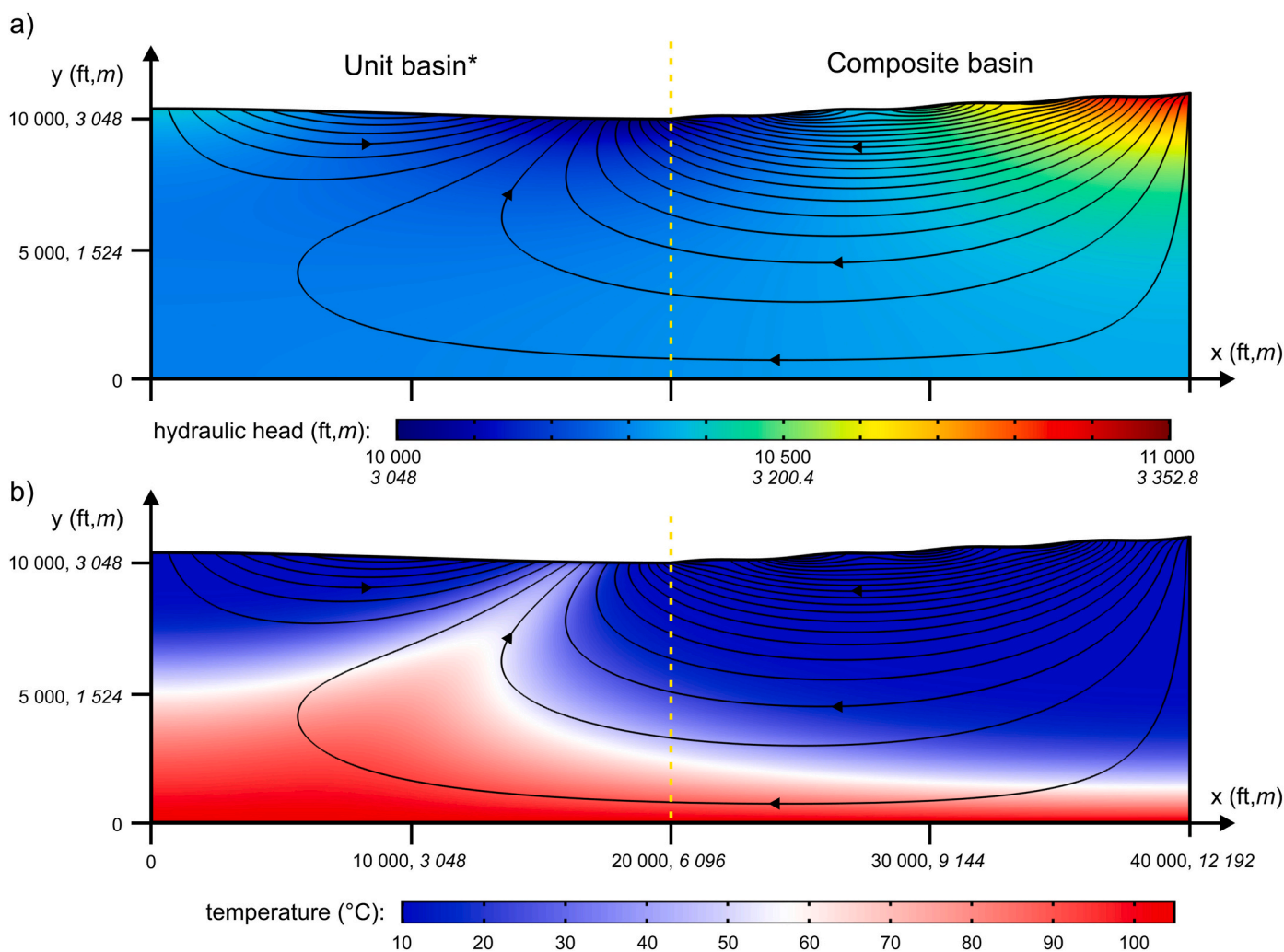
Fig. B.6. Simulation results of model 3.c: h_{left} = 100 ft./30.48 m a) Hydraulic head distribution and b) Temperature field with magnitude controlled streamlines. Calculated recharge rate: 139 mm/yr, maximum of Darcy velocity magnitude: $1.43 \cdot 10^{-7}$ m/s, number of streamlines: 20. Centerline is represented by the yellow dashed line. (For interpretation of the references to colour in this figure legend, the reader is referred to the web version of this article.)
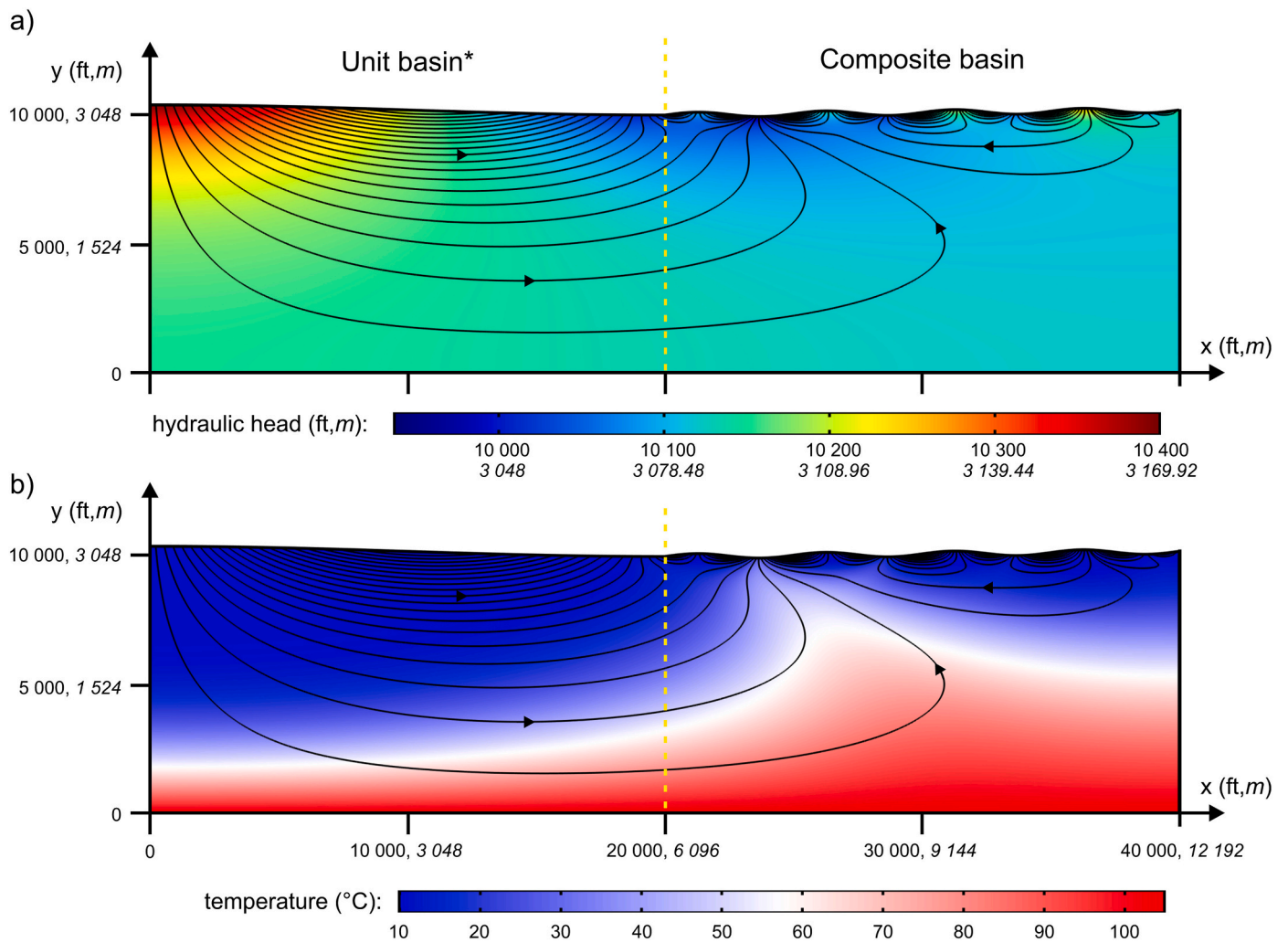
a)

b)

Fig. B.7. Simulation results of model 3.d: $h_{left} = 0$ ft./0 m a) Hydraulic head distribution and b) Temperature field with magnitude controlled streamlines. Calculated recharge rate: 137 mm/yr, maximum of Darcy velocity magnitude: $1.41 \cdot 10^{-7}$ m/s, number of streamlines: 20. Centerline is represented by the yellow dashed line. (For interpretation of the references to colour in this figure legend, the reader is referred to the web version of this article.)

Fig. B.8. Simulation results of model 4.a: $h_{right} = 200$ ft./60.96 m, $a' \approx 50$ ft./15.24 m, $c' = 0.01$ a) Hydraulic head distribution and b) Temperature field with magnitude controlled streamlines. Calculated recharge rate: 168 mm/yr, maximum of Darcy velocity magnitude: $1.22 \cdot 10^{-7}$ m/s, number of streamlines: 20. Centerline is represented by the yellow dashed line. (For interpretation of the references to colour in this figure legend, the reader is referred to the web version of this article.)
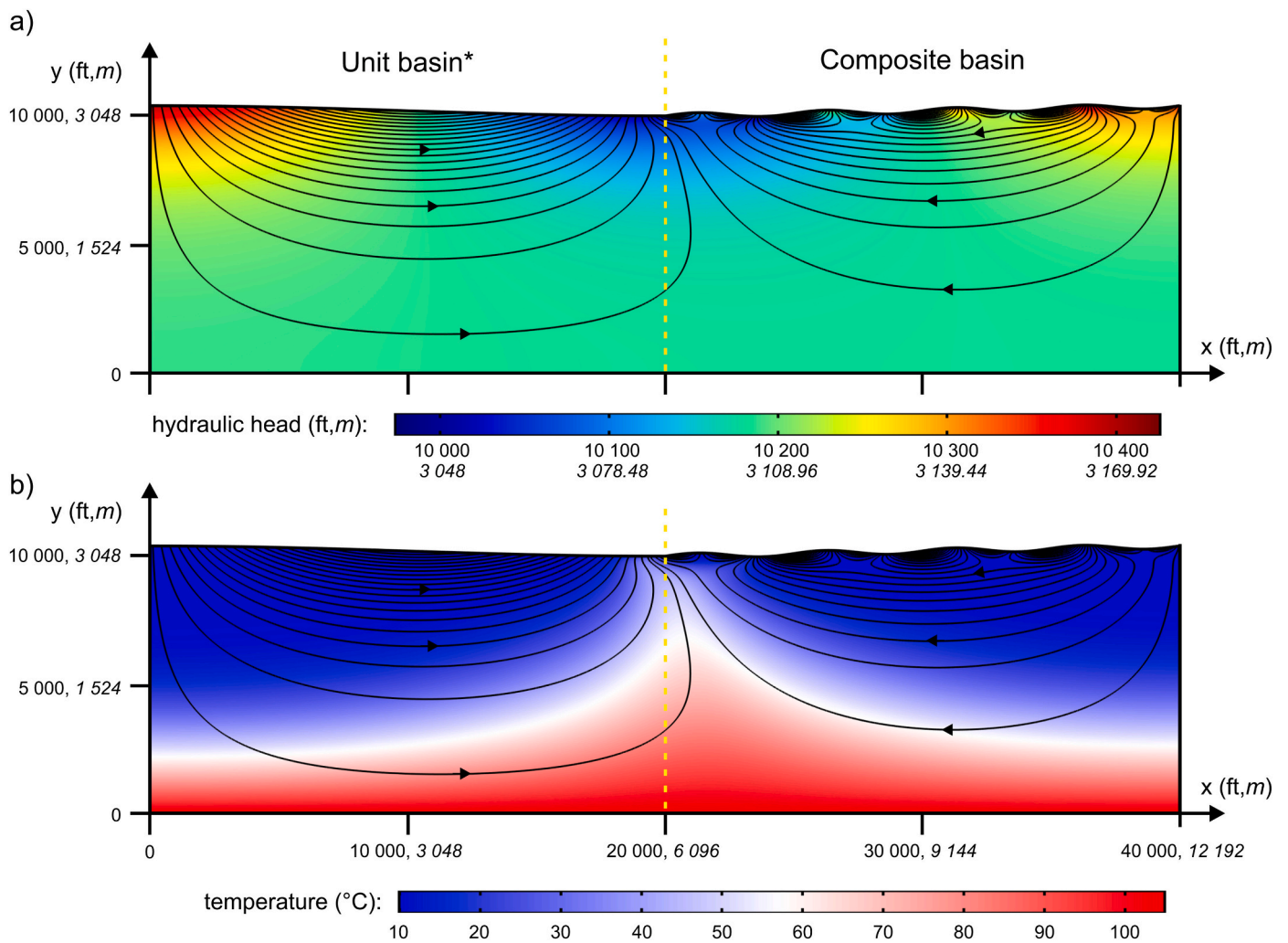
Fig. B.9. Simulation results of model 4.b: $h_{right} = 1000$ ft./304.8 m, a' ≈ 50 ft./15.24 m, c' = 0.05 a) Hydraulic head distribution and b) Temperature field with magnitude controlled streamlines. Calculated recharge rate: 224 mm/yr, maximum of Darcy velocity magnitude: 2.45·10^{-7} m/s, number of streamlines: 20. Centerline is represented by the yellow dashed line. (For interpretation of the references to colour in this figure legend, the reader is referred to the web version of this article.)
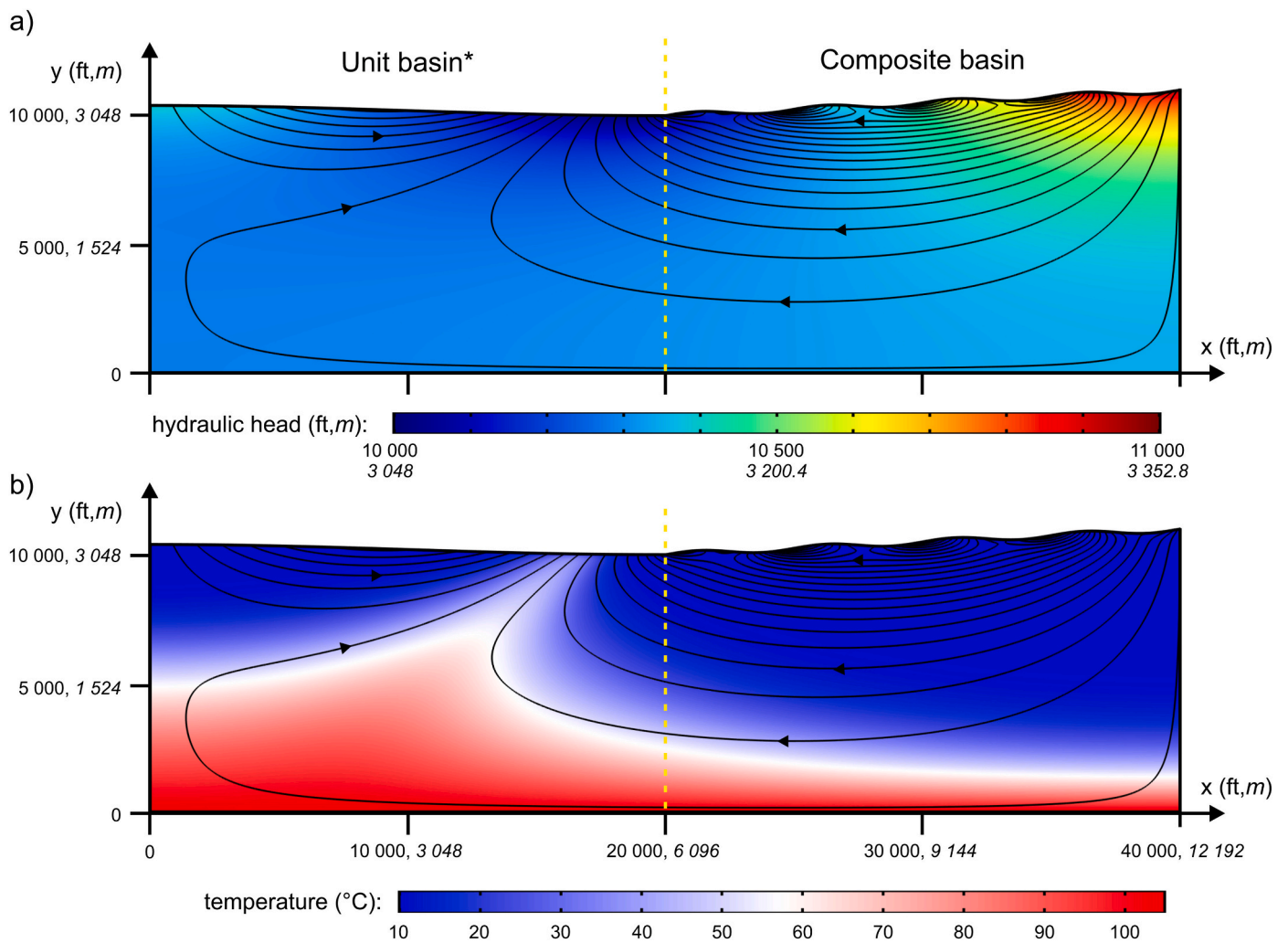
Fig. B.10. Simulation results of model 4.c: $h_{right} = 200\,\text{ft.}/60.96\,\text{m}$, $a' \approx 100\,\text{ft.}/30.48\,\text{m}$, $c' = 0.01$ a) Hydraulic head distribution and b) Temperature field with magnitude controlled streamlines. Calculated recharge rate: 306 mm/yr, maximum of Darcy velocity magnitude: $2.66 \cdot 10^{-7}$ m/s, number of streamlines: 20. Centerline is represented by the yellow dashed line. (For interpretation of the references to colour in this figure legend, the reader is referred to the web version of this article.)
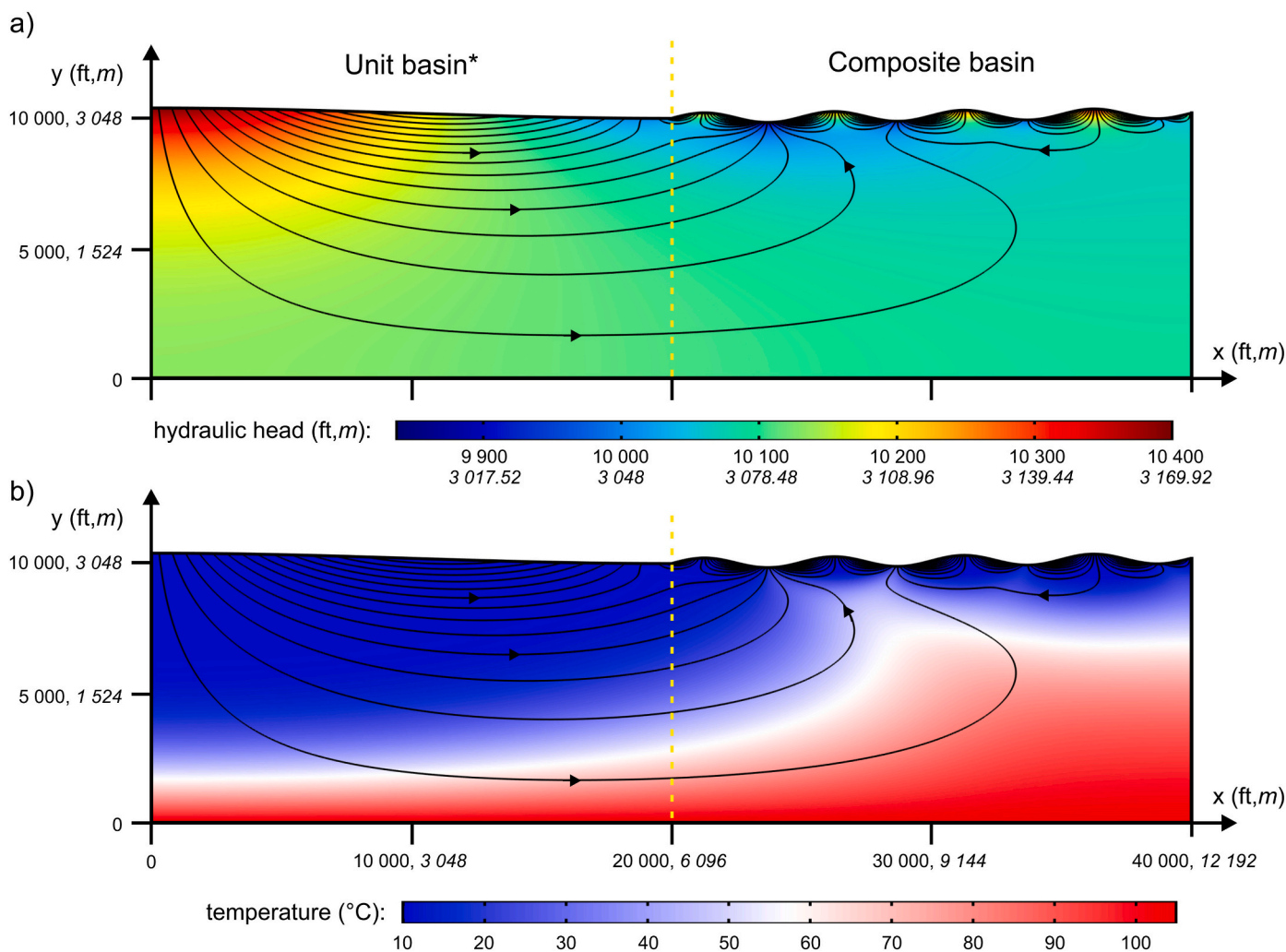
a)

b)

Fig. B.11. Simulation results of model 4.d: $h_{right} = 400$ ft./121.92 m, a' ≈ 100 ft./30.48 m, c' = 0.02 a) Hydraulic head distribution and b) Temperature field with magnitude controlled streamlines. Calculated recharge rate: 310 mm/yr, maximum of Darcy velocity magnitude: $3.04 \cdot 10^{-7}$ m/s, number of streamlines: 20. Centerline is represented by the yellow dashed line. (For interpretation of the references to colour in this figure legend, the reader is referred to the web version of this article.)
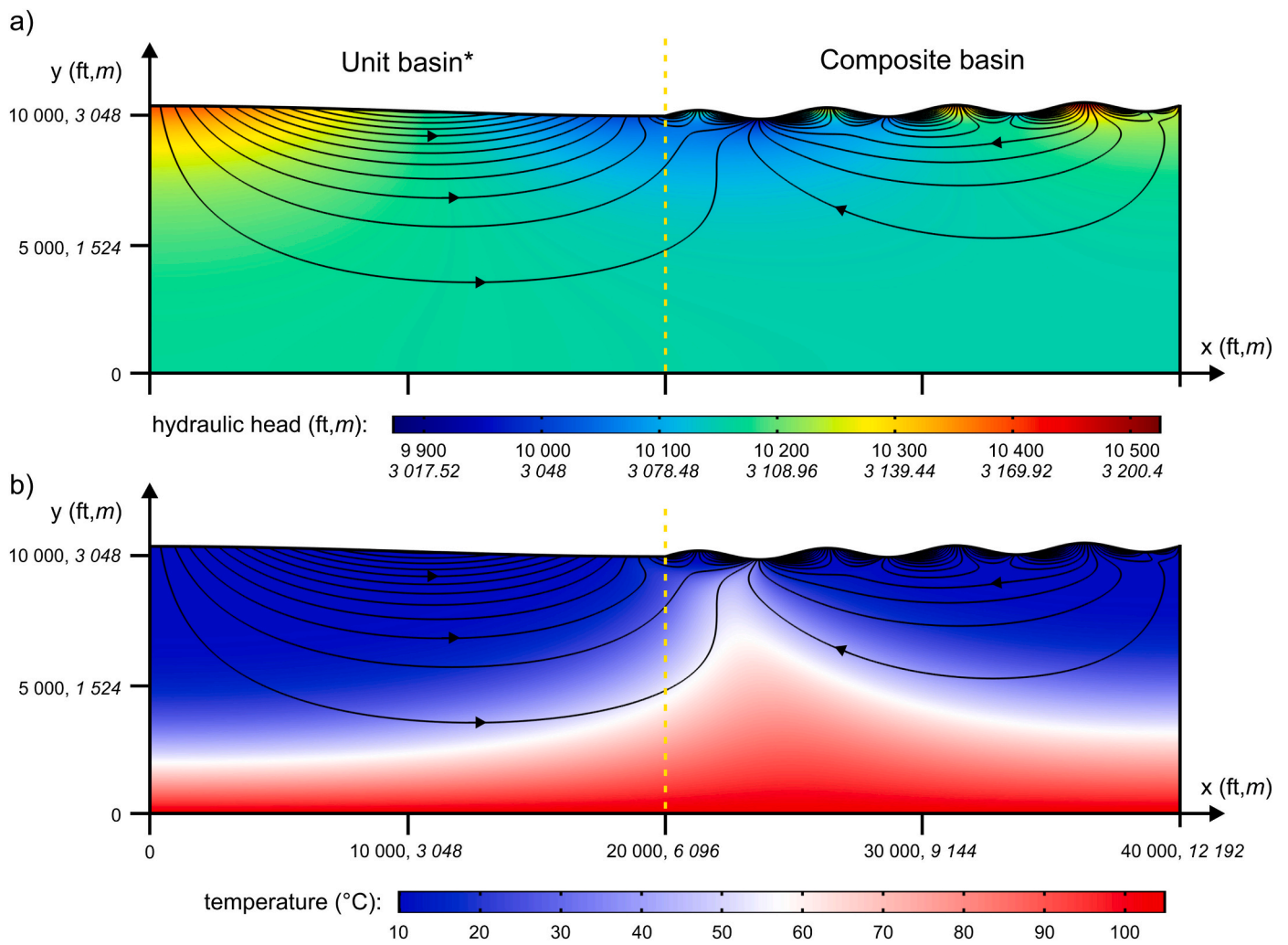
Fig. B.12. Simulation results of model 4.e: $h_{right} = 1000$ ft./304.8 m, a' $\approx$ 100 ft./30.48 m, c' = 0.05 a) Hydraulic head distribution and b) Temperature field with magnitude controlled streamlines. Calculated recharge rate: 339 mm/yr, maximum of Darcy velocity magnitude: $4.33 \cdot 10^{-7}$ m/s, number of streamlines: 20. Centerline is represented by the yellow dashed line. (For interpretation of the references to colour in this figure legend, the reader is referred to the web version of this article.)

Fig. B.13. Simulation results of model 4.f: $h_{right} = 200$ ft./60.96 m, a' ≈ 200 ft./60.96 m, c' = 0.01 a) Hydraulic head distribution and b) Temperature field with magnitude controlled streamlines. Calculated recharge rate: 595 mm/yr, maximum of Darcy velocity magnitude: $6.08 \cdot 10^{-7}$ m/s, number of streamlines: 20. Centerline is represented by the yellow dashed line. (For interpretation of the references to colour in this figure legend, the reader is referred to the web version of this article.)
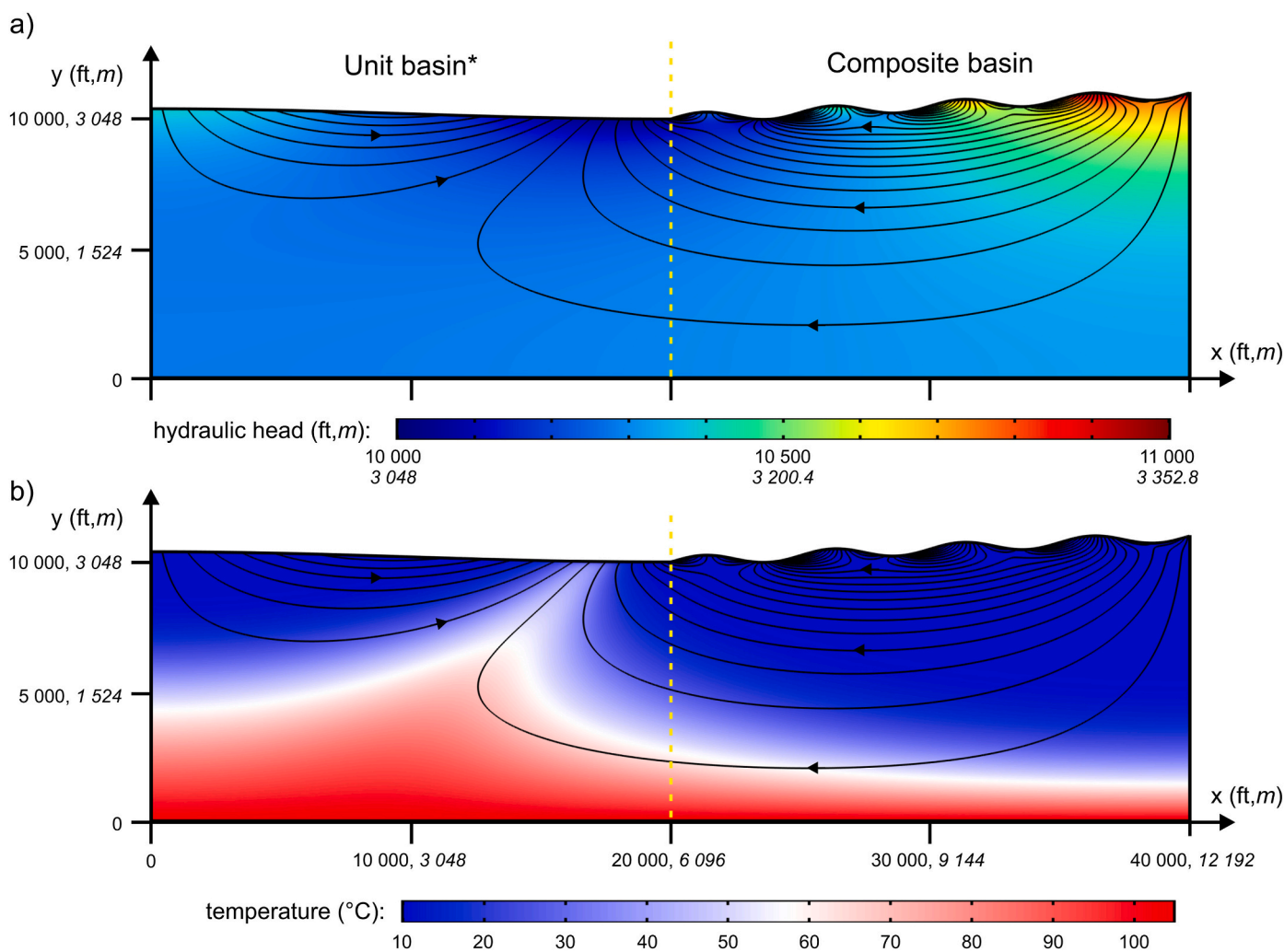
Fig. B.14. Simulation results of model 4.g: $h_{right} = 400$ ft./121.92 m, a' ≈ 200 ft./60.96 m, c' = 0.02 a) Hydraulic head distribution and b) Temperature field with magnitude controlled streamlines. Calculated recharge rate: 596 mm/yr, maximum of Darcy velocity magnitude: $6.62 \cdot 10^{-7}$ m/s, number of streamlines: 20. Centerline is represented by the yellow dashed line. (For interpretation of the references to colour in this figure legend, the reader is referred to the web version of this article.)
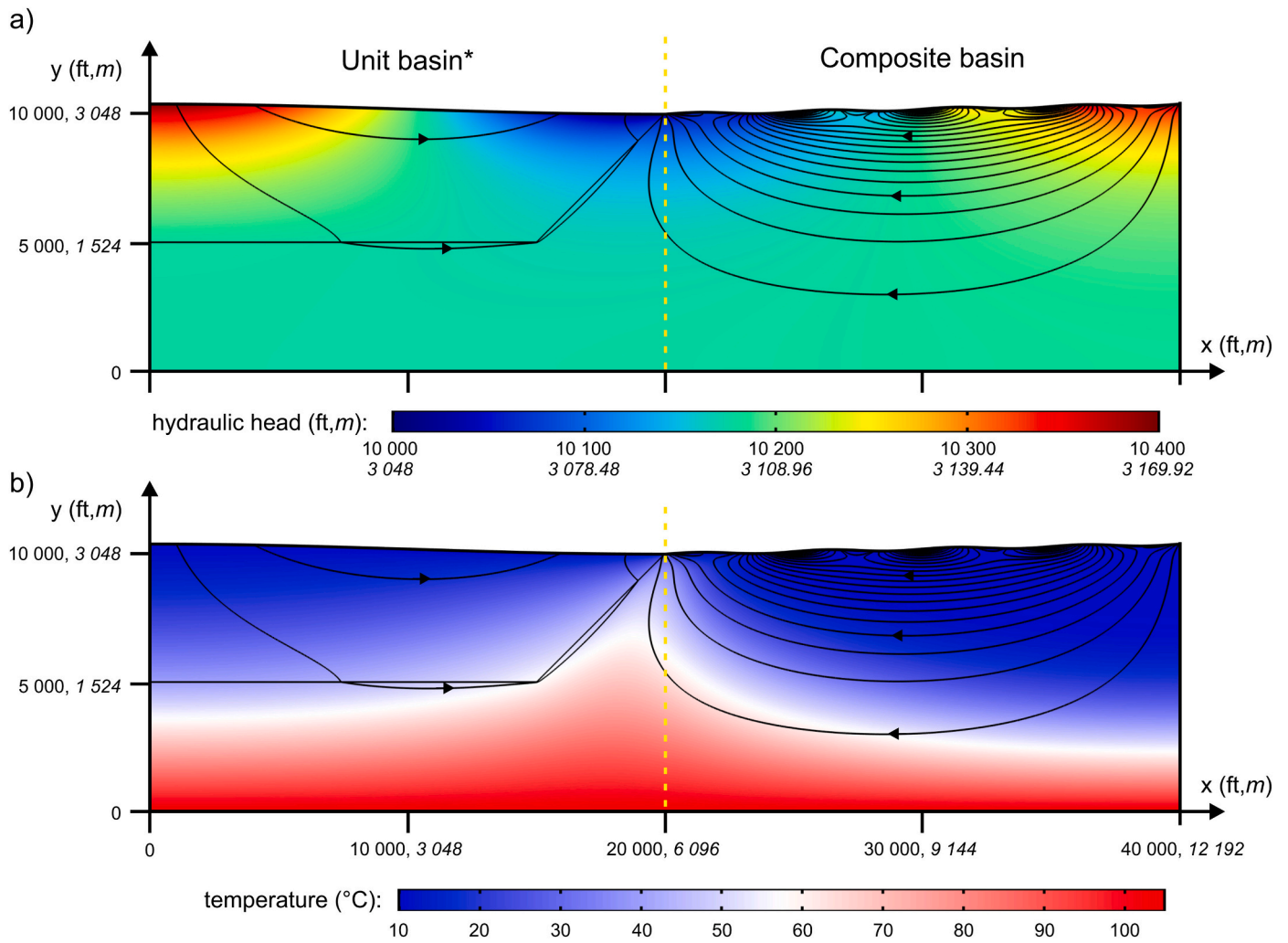
Fig. B.15. Simulation results of model 4.h: $h_{right} = 1000$ ft./304.8 m, a' $\approx$ 200 ft./60.96 m, c' $= 0.05$ a) Hydraulic head distribution and b) Temperature field with magnitude controlled streamlines. Calculated recharge rate: 608 mm/yr, maximum of Darcy velocity magnitude: $8.36 \cdot 10^{-7}$ m/s, number of streamlines: 20. Centerline is represented by the yellow dashed line. (For interpretation of the references to colour in this figure legend, the reader is referred to the web version of this article.)

a)

hydraulic head (ft,*m*):

| 10 000 | 10 100 | 10 200 | 10 300 | 10 400 |
| 3 048 | 3 078.48 | 3 108.96 | 3 139.44 | 3 169.92 |

b)

temperature (°C):

10   20   30   40   50   60   70   80   90   100

Fig. B.16. Simulation results of model 5.a: half basin fill in the Unit basin* a) Hydraulic head distribution and b) Temperature field with magnitude controlled streamlines. Calculated recharge rate: 125 mm/yr, maximum of Darcy velocity magnitude: $3.2 \cdot 10^{-7}$ m/s, number of streamlines: 20. Centerline is represented by the yellow dashed line. (For interpretation of the references to colour in this figure legend, the reader is referred to the web version of this article.)
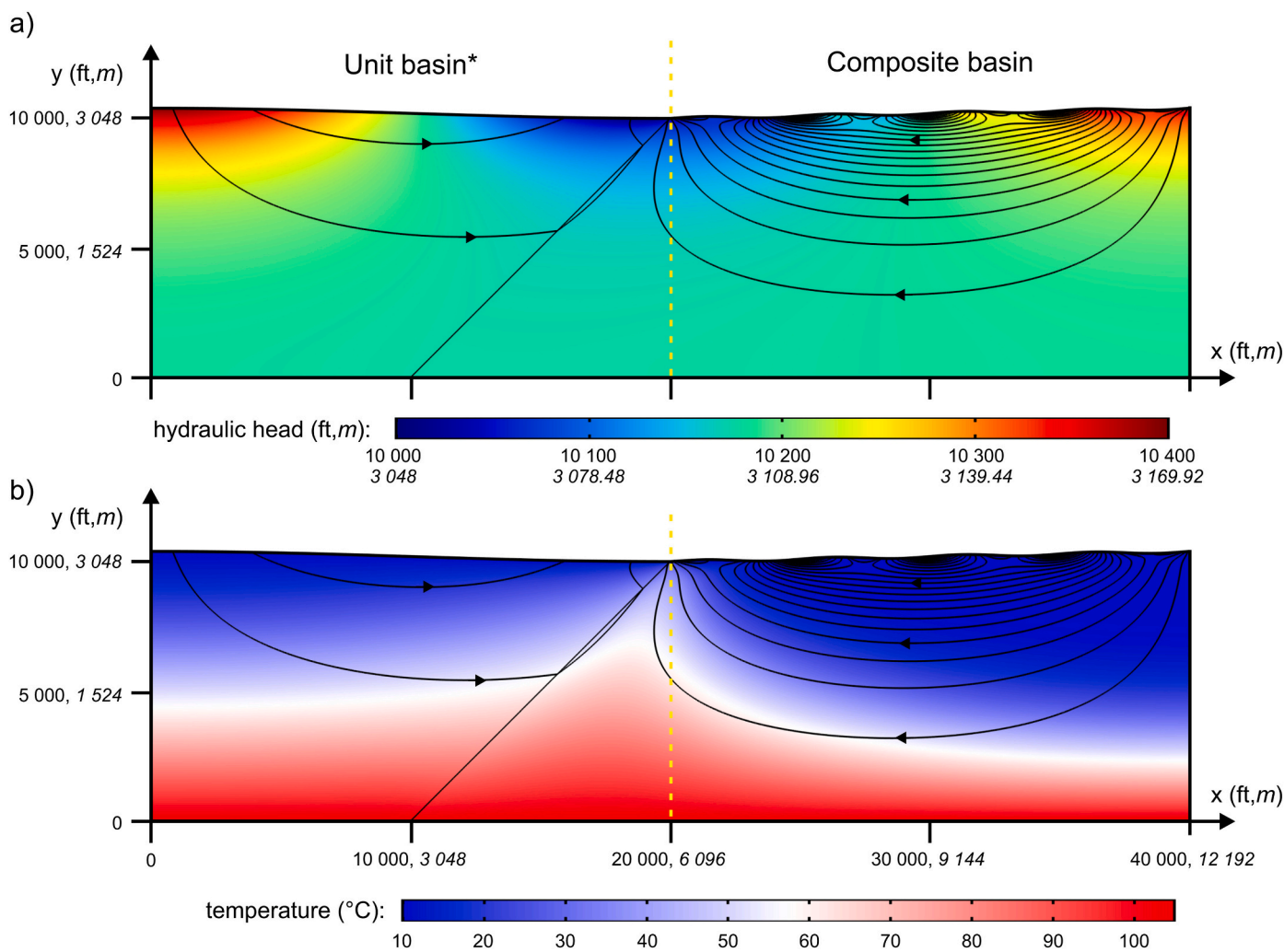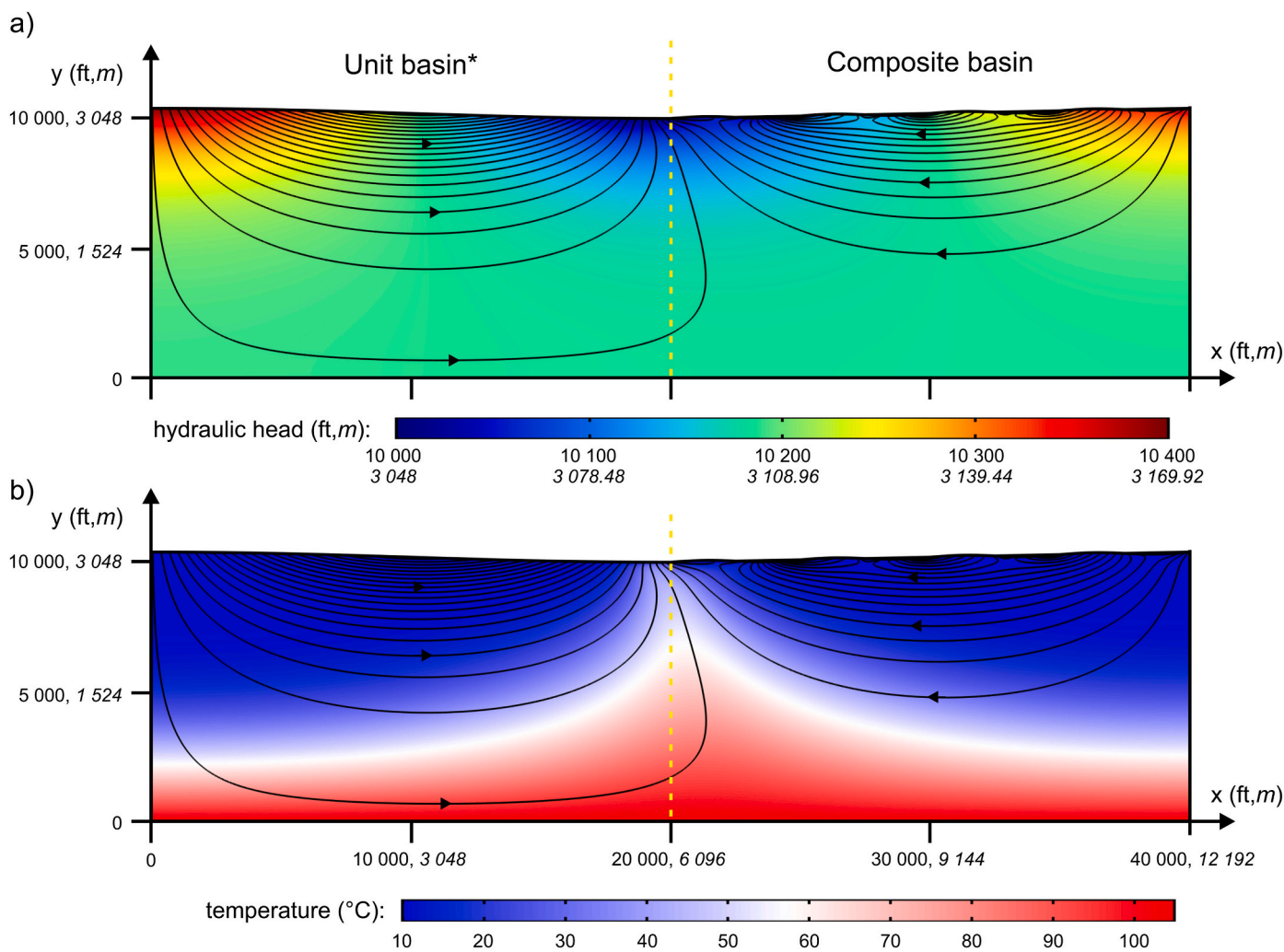
Fig. B.17. Simulation results of model 5.b: full basin fill in the Unit basin* a) Hydraulic head distribution and b) Temperature field with magnitude controlled streamlines. Calculated recharge rate: 125 mm/yr, maximum of Darcy velocity magnitude: $3.2 \cdot 10^{-7}$ m/s, number of streamlines: 20. Centerline is represented by the yellow dashed line. (For interpretation of the references to colour in this figure legend, the reader is referred to the web version of this article.)

Fig. B.18. Simulation results of model 5.c: semi-confining cover in the Composite basin a) Hydraulic head distribution and b) Temperature field with magnitude controlled streamlines. Calculated recharge rate: 140 mm/yr, maximum of Darcy velocity magnitude: $3.37 \cdot 10^{-7}$ m/s, number of streamlines: 20. Centerline is represented by the yellow dashed line. (For interpretation of the references to colour in this figure legend, the reader is referred to the web version of this article.)
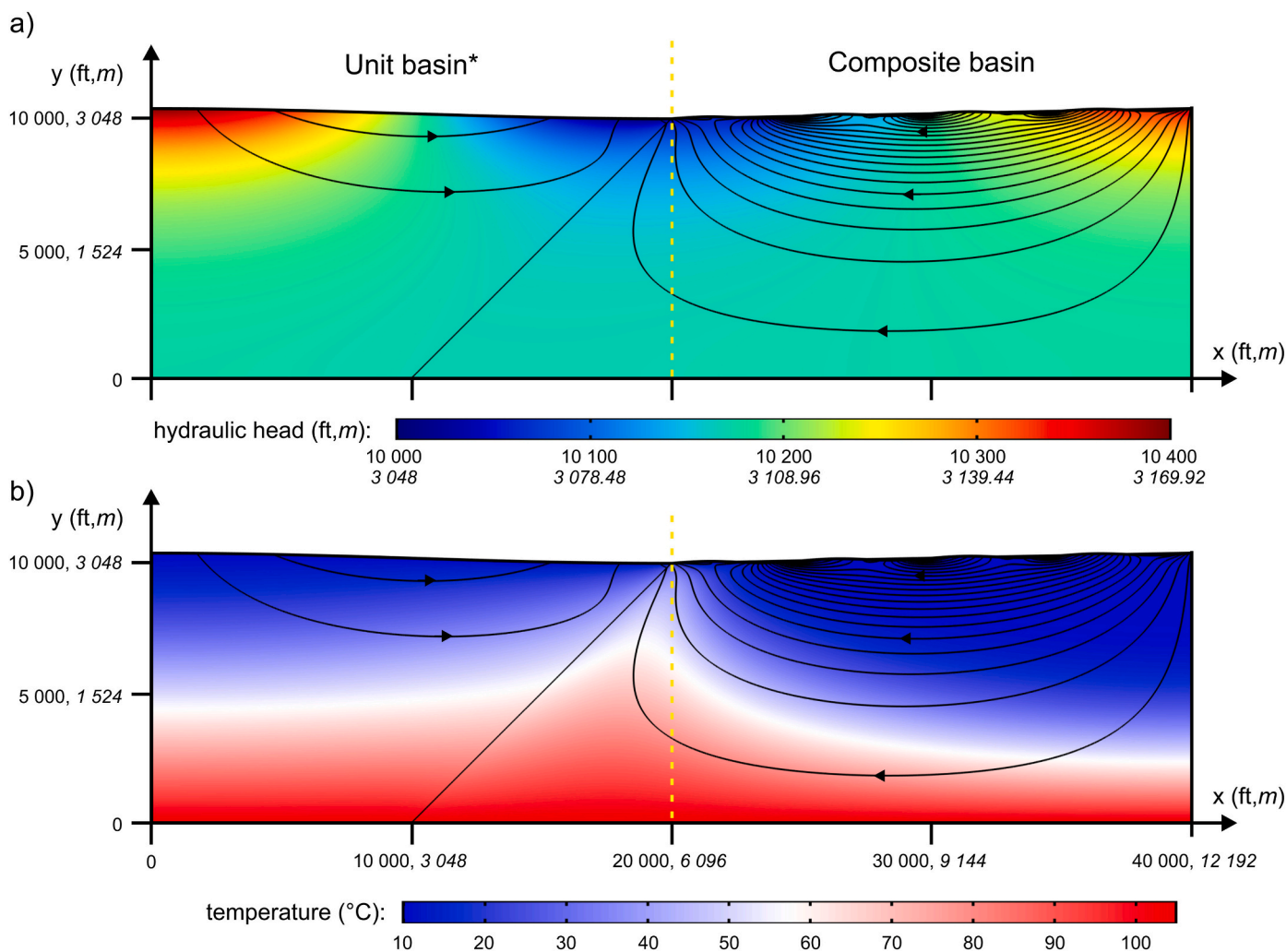
Fig. B.19. Simulation results of model 5.d: full basin fill in the Unit basin* and semi-confining cover in the Composite basin a) Hydraulic head distribution and b) Temperature field with magnitude controlled streamlines. Calculated recharge rate: 90 mm/yr, maximum of Darcy velocity magnitude: $8.05 \cdot 10^{-7}$ m/s, number of streamlines: 20. Centerline is represented by the yellow dashed line. (For interpretation of the references to colour in this figure legend, the reader is referred to the web version of this article.)
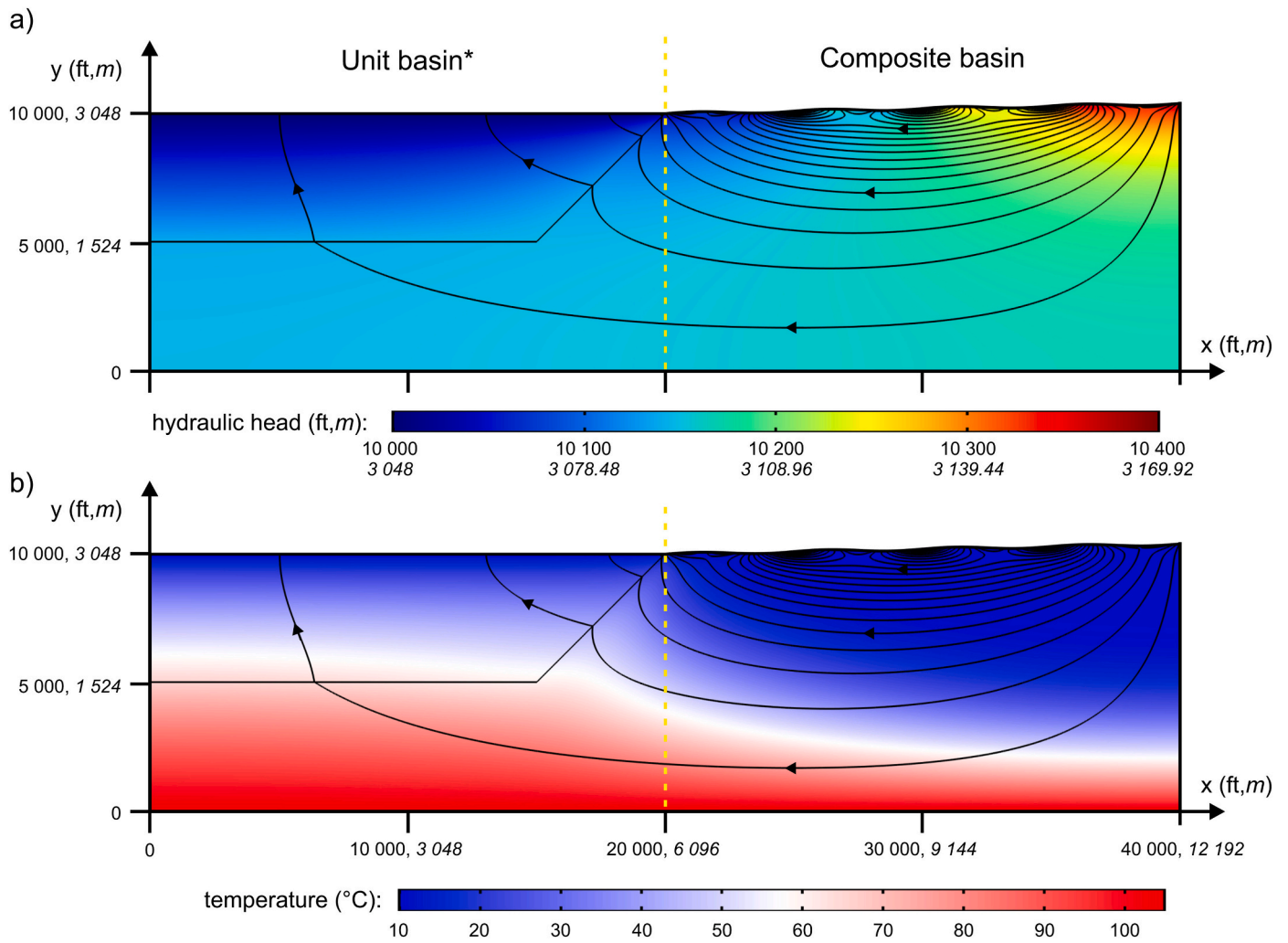
Fig. B.20. Simulation results of model 6.a: half basin fill in the flat Unit basin* a) Hydraulic head distribution and b) Temperature field with magnitude controlled streamlines. Calculated recharge rate: 123 mm/yr, maximum of Darcy velocity magnitude: $3.14 \cdot 10^{-7}$ m/s, number of streamlines: 20. Centerline is represented by the yellow dashed line. (For interpretation of the references to colour in this figure legend, the reader is referred to the web version of this article.)
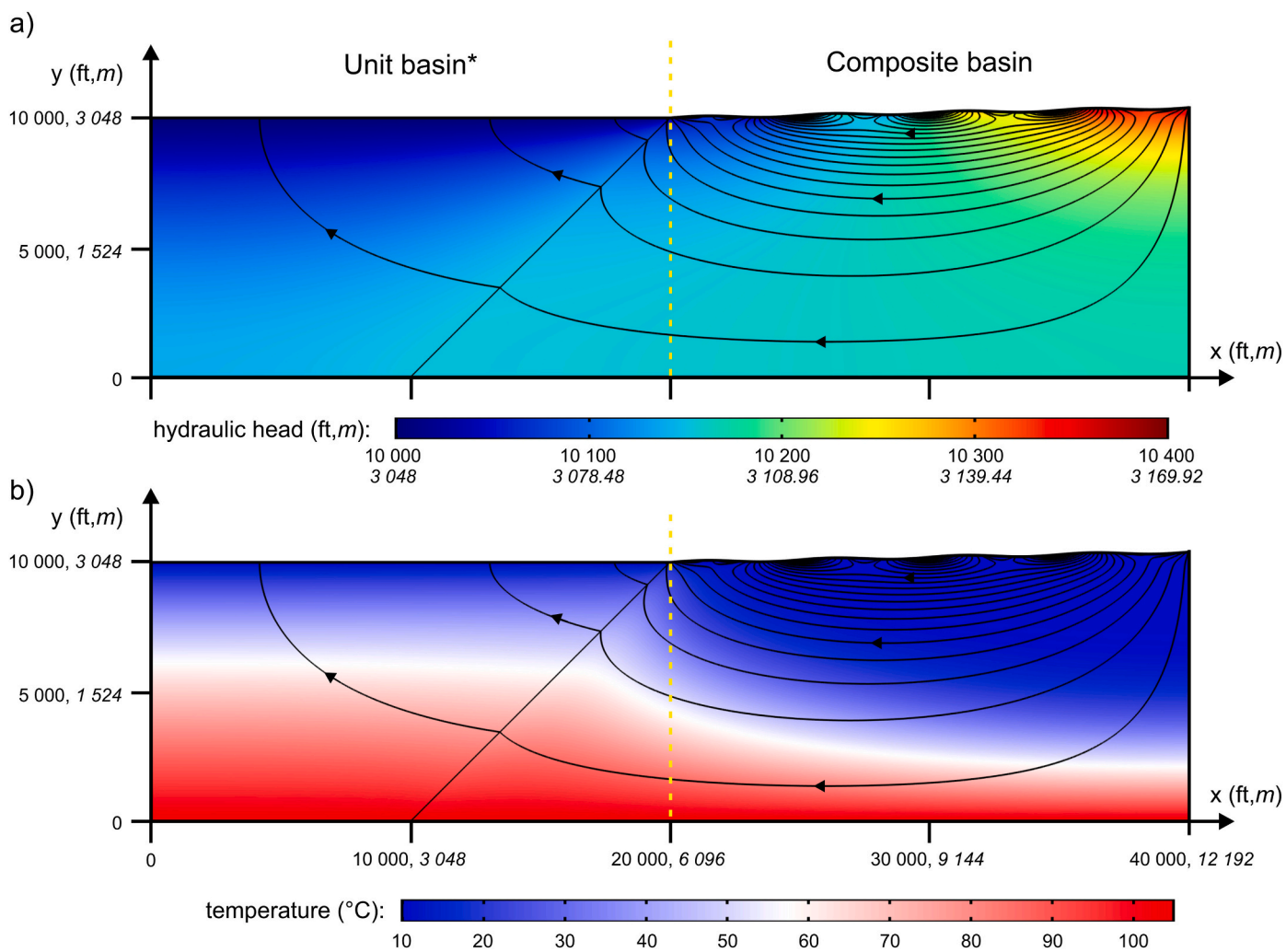
Fig. B.21. Simulation results of model 6.b: full basin fill in the flat Unit basin* a) Hydraulic head distribution and b) Temperature field with magnitude controlled streamlines. Calculated recharge rate: 123 mm/yr, maximum of Darcy velocity magnitude: $3.14 \cdot 10^{-7}$ m/s, number of streamlines: 20. Centerline is represented by the yellow dashed line. (For interpretation of the references to colour in this figure legend, the reader is referred to the web version of this article.)
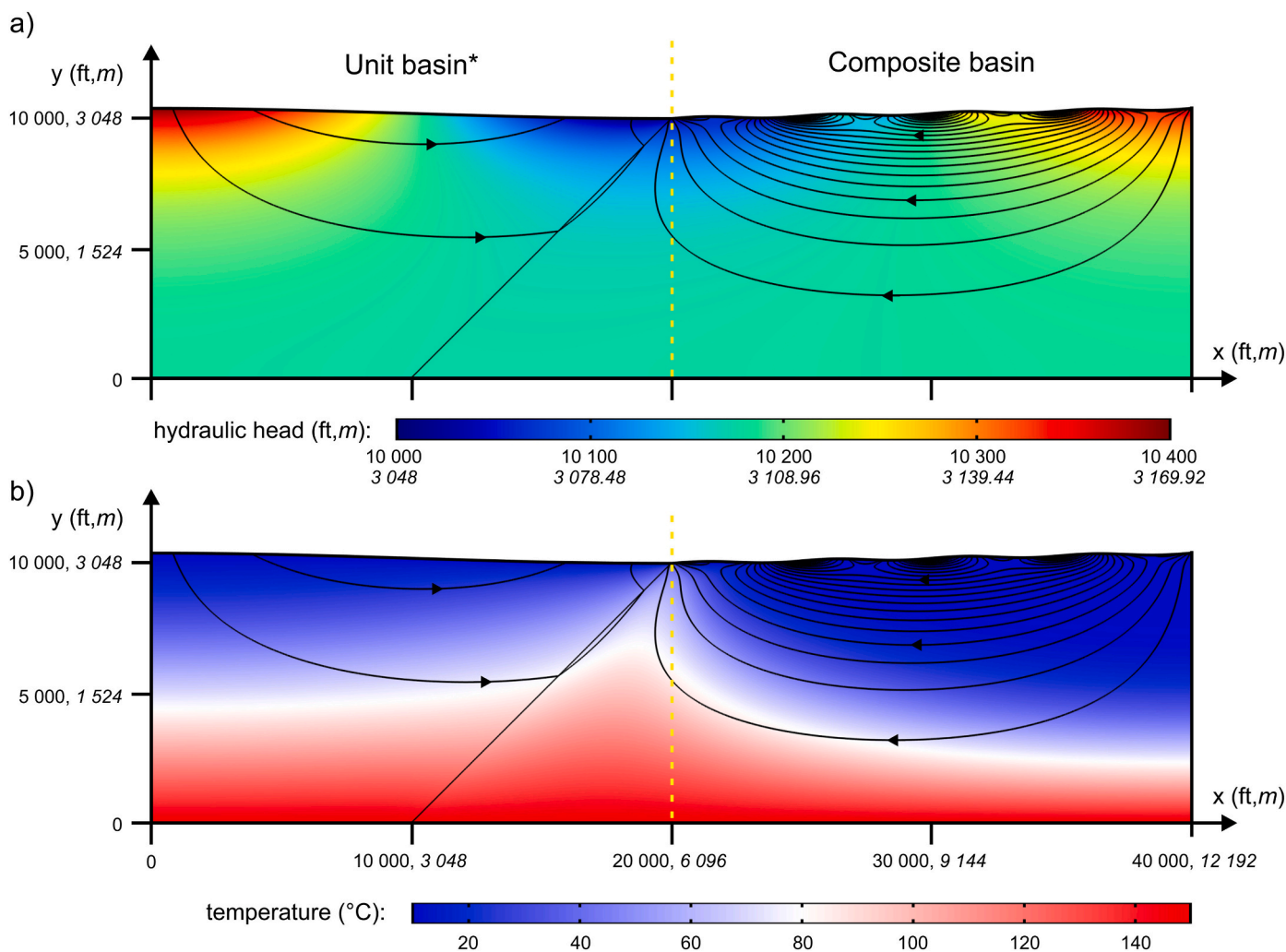
Fig. B.22. Simulation results of model 7.a: full basin fill in the Unit basin*, 150 °C as the bottom thermal boundary condition a) Hydraulic head distribution and b) Temperature field with magnitude controlled streamlines. Calculated recharge rate: 125 mm/yr, maximum of Darcy velocity magnitude: $3.2 \cdot 10^{-7}$ m/s, number of streamlines: 20. Centerline is represented by the yellow dashed line. (For interpretation of the references to colour in this figure legend, the reader is referred to the web version of this article.)

Fig. B.23. Simulation results of model 7.b: full basin fill in the Unit basin*, 195 °C as the bottom thermal boundary condition a) Hydraulic head distribution and b) Temperature field with magnitude controlled streamlines. Calculated recharge rate: 125 mm/yr, maximum of Darcy velocity magnitude: $3.2 \cdot 10^{-7}$ m/s, number of streamlines: 20. Centerline is represented by the yellow dashed line. (For interpretation of the references to colour in this figure legend, the reader is referred to the web version of this article.)
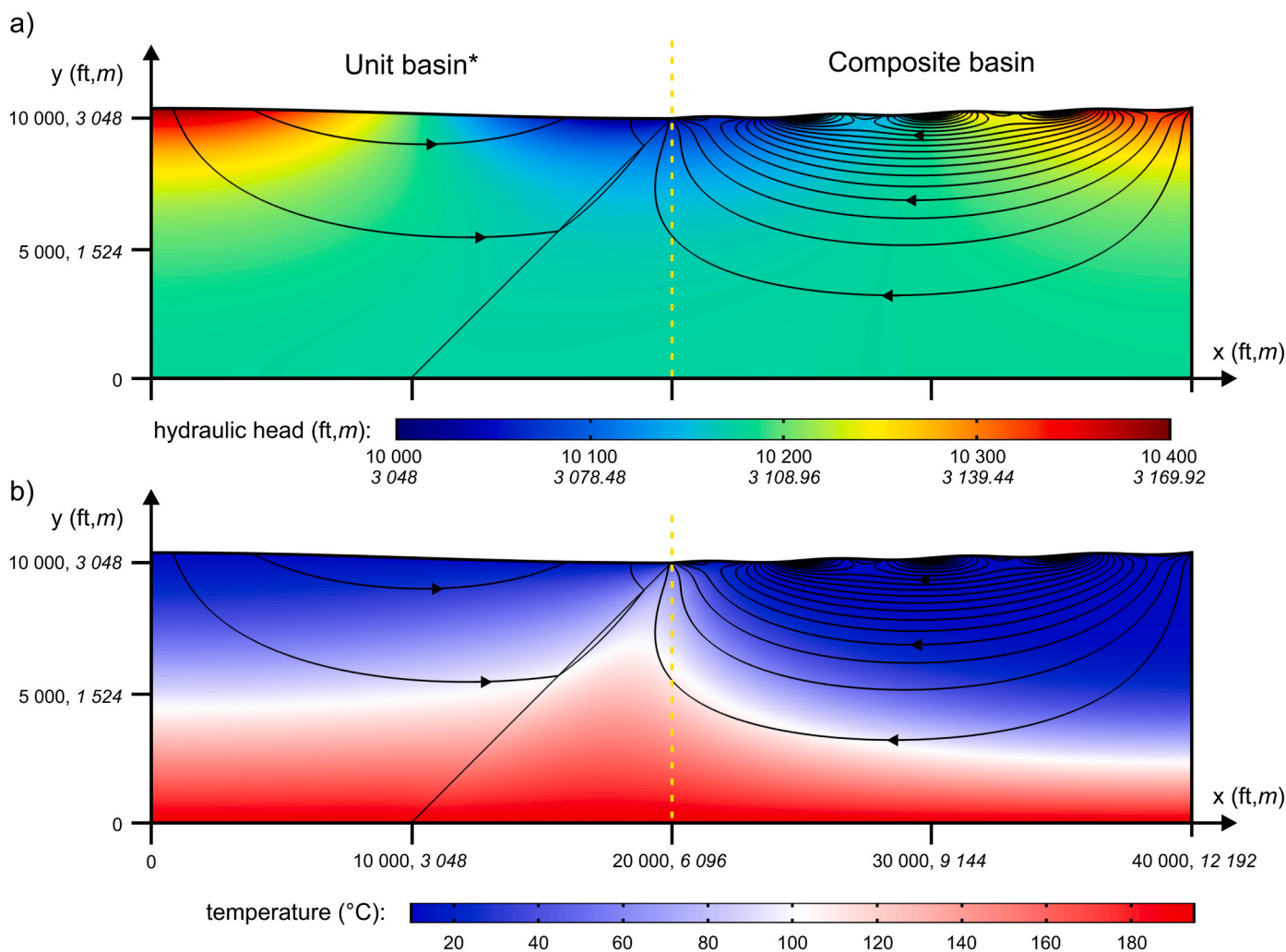
Fig. B.24. Simulation results of model 7.c: full basin fill in the Unit basin*, 240 °C as the bottom thermal boundary condition a) Hydraulic head distribution and b) Temperature field with magnitude controlled streamlines. Calculated recharge rate: 125 mm/yr, maximum of Darcy velocity magnitude: $3.2 \cdot 10^{-7}$ m/s, number of streamlines: 20. Centerline is represented by the yellow dashed line. (For interpretation of the references to colour in this figure legend, the reader is referred to the web version of this article.)
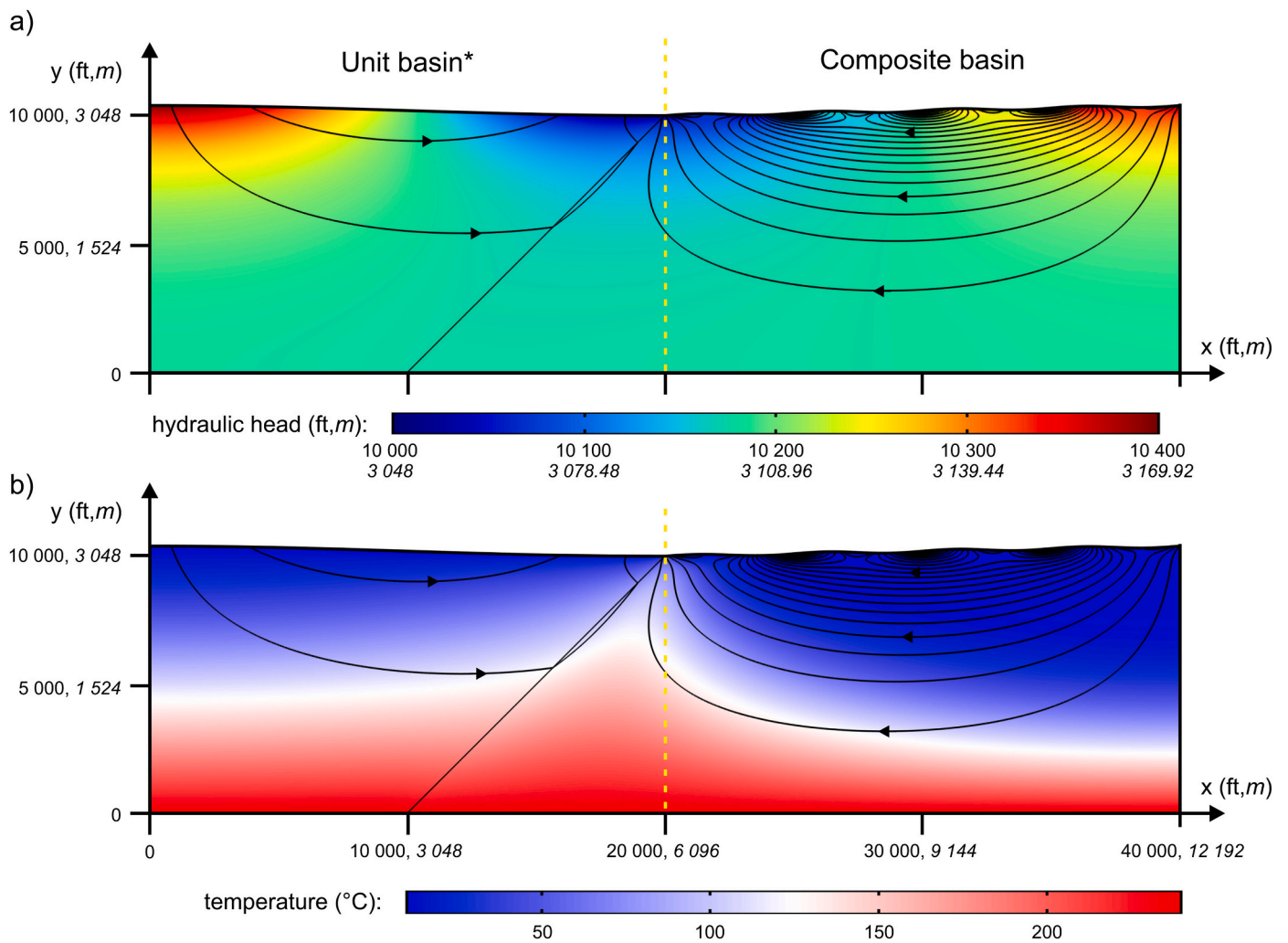
Fig. B.25. Simulation results of model 7.d: full basin fill in the Unit basin*, 285 °C as the bottom thermal boundary condition a) Hydraulic head distribution and b) Temperature field with magnitude controlled streamlines. Calculated recharge rate: 125 mm/yr, maximum of Darcy velocity magnitude: $3.2 \cdot 10^{-7}$ m/s, number of streamlines: 20. Centerline is represented by the yellow dashed line. (For interpretation of the references to colour in this figure legend, the reader is referred to the web version of this article.)
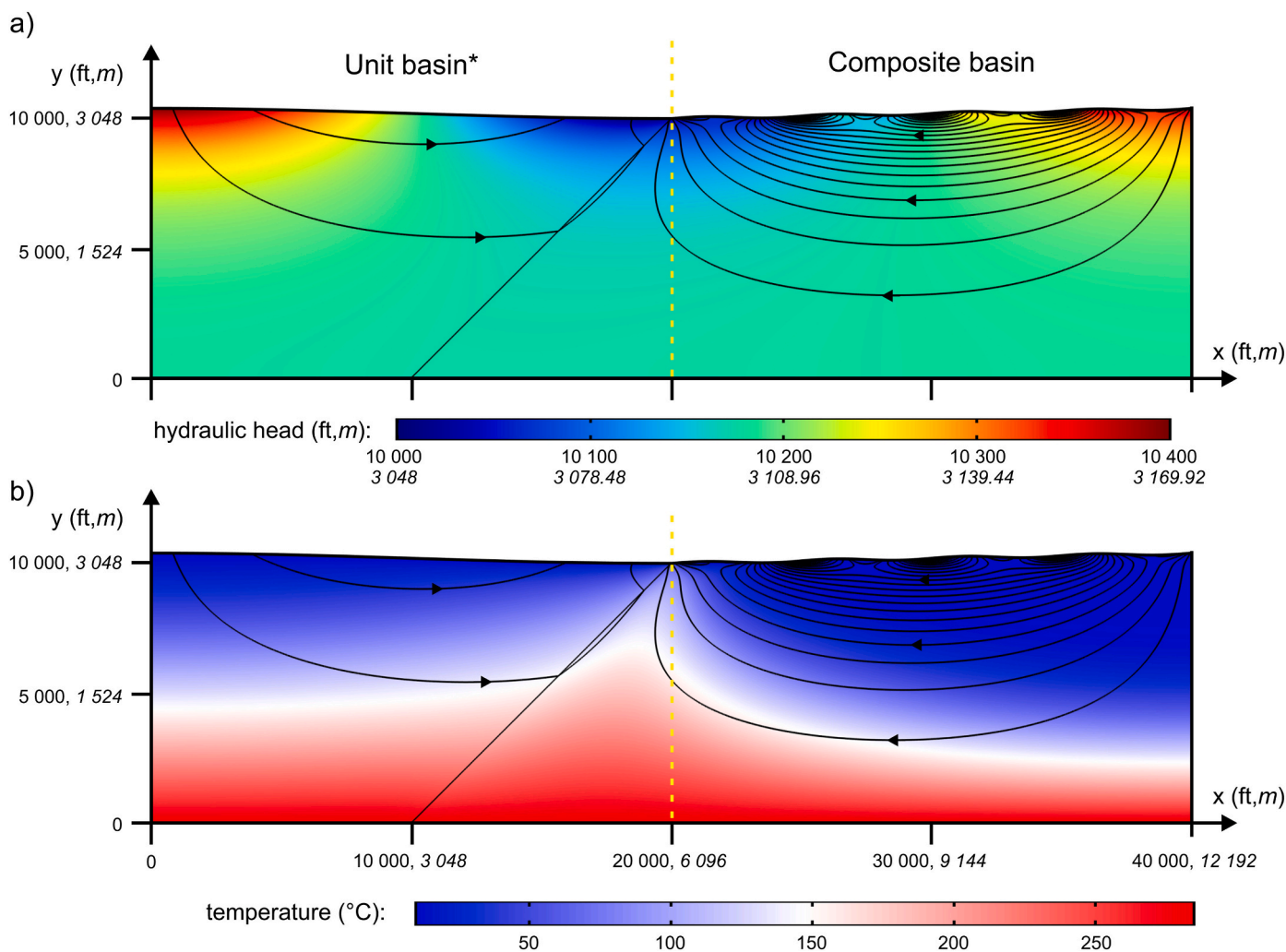
Fig. B.26. Simulation results of model 8.a: full basin fill in the flat Unit basin*, 150 °C as the bottom thermal boundary condition a) Hydraulic head distribution and b) Temperature field with magnitude controlled streamlines. Calculated recharge rate: 123 mm/yr, maximum of Darcy velocity magnitude: $3.14 \cdot 10^{-7}$ m/s, number of streamlines: 20. Centerline is represented by the yellow dashed line. (For interpretation of the references to colour in this figure legend, the reader is referred to the web version of this article.)
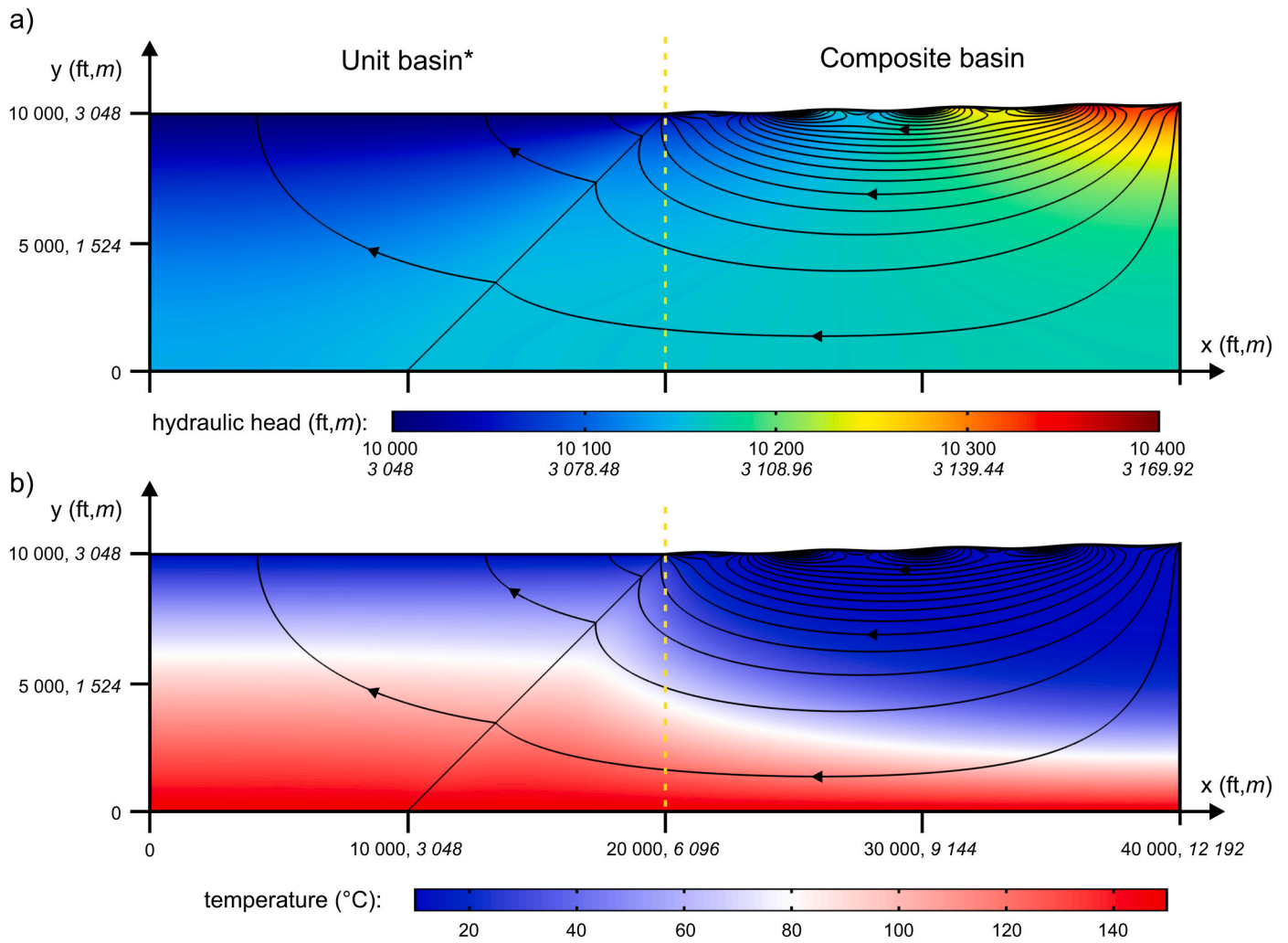
Fig. B.27. Simulation results of model 8.b: full basin fill in the flat Unit basin*, 195 °C as the bottom thermal boundary condition a) Hydraulic head distribution and b) Temperature field with magnitude controlled streamlines. Calculated recharge rate: 123 mm/yr, maximum of Darcy velocity magnitude: $3.14 \cdot 10^{-7}$ m/s, number of streamlines: 20. Centerline is represented by the yellow dashed line. (For interpretation of the references to colour in this figure legend, the reader is referred to the web version of this article.)
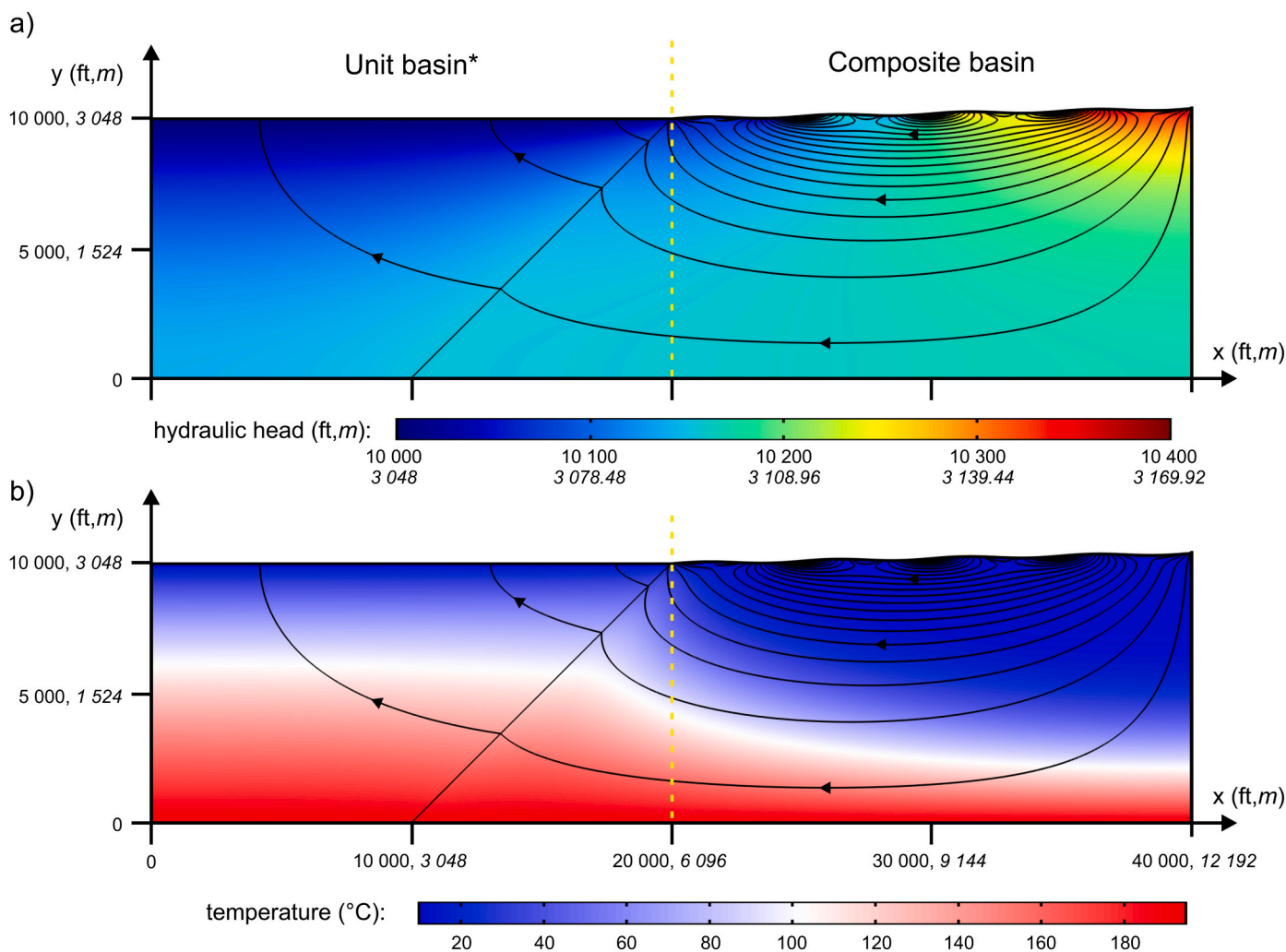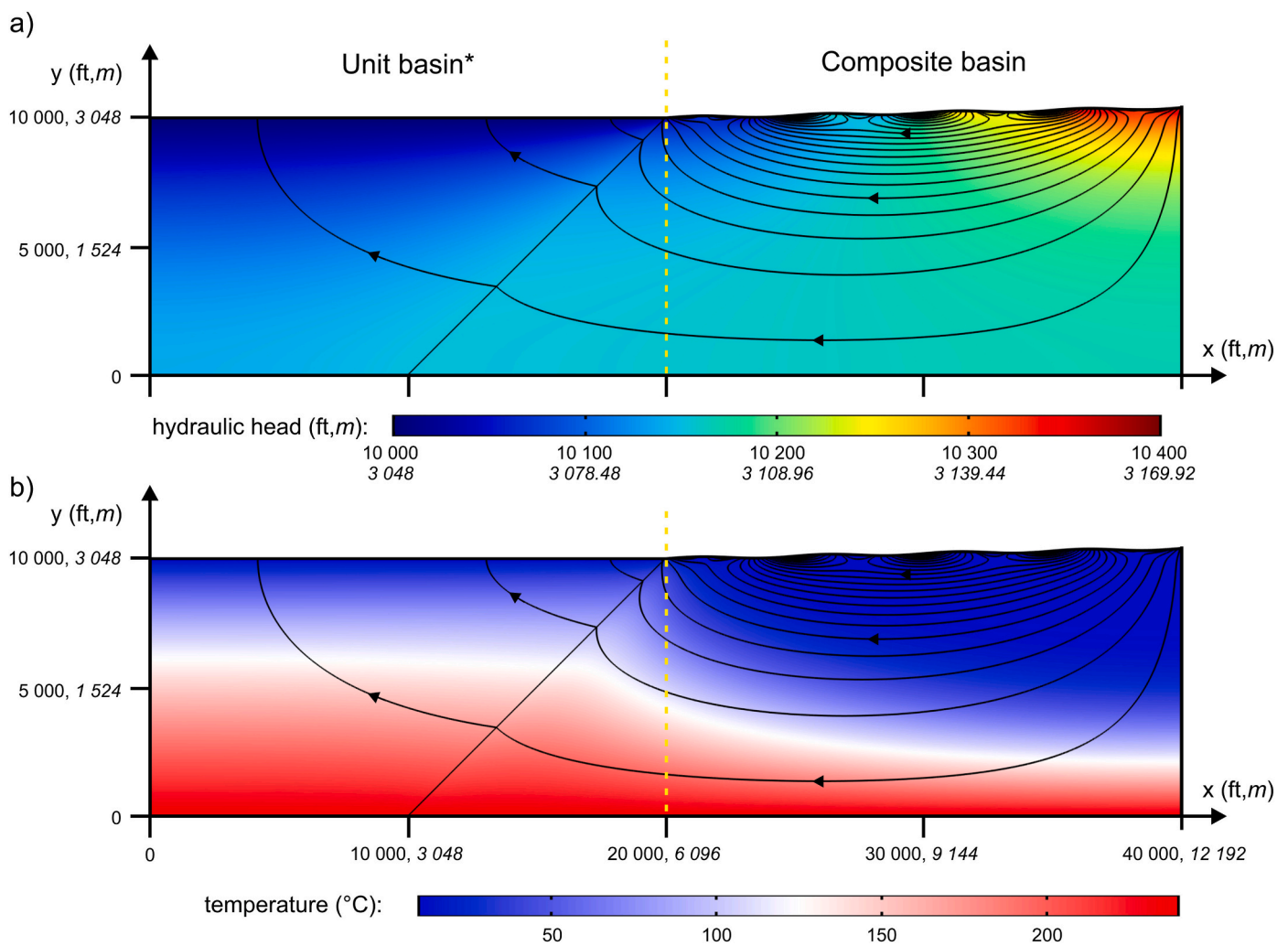
Fig. B.28. Simulation results of model 8.c: full basin fill in the flat Unit basin*, 240 °C as the bottom thermal boundary condition a) Hydraulic head distribution and b) Temperature field with magnitude controlled streamlines. Calculated recharge rate: 123 mm/yr, maximum of Darcy velocity magnitude: $3.14 \cdot 10^{-7}$ m/s, number of streamlines: 20. Centerline is represented by the yellow dashed line. (For interpretation of the references to colour in this figure legend, the reader is referred to the web version of this article.)

a)

b)

Fig. B.29. Simulation results of model 8.d: full basin fill in the flat Unit basin*, 285 °C as the bottom thermal boundary condition a) Hydraulic head distribution and b) Temperature field with magnitude controlled streamlines. Calculated recharge rate: 123 mm/yr, maximum of Darcy velocity magnitude: $3.14 \cdot 10^{-7}$ m/s, number of streamlines: 20. Centerline is represented by the yellow dashed line. (For interpretation of the references to colour in this figure legend, the reader is referred to the web version of this article.)
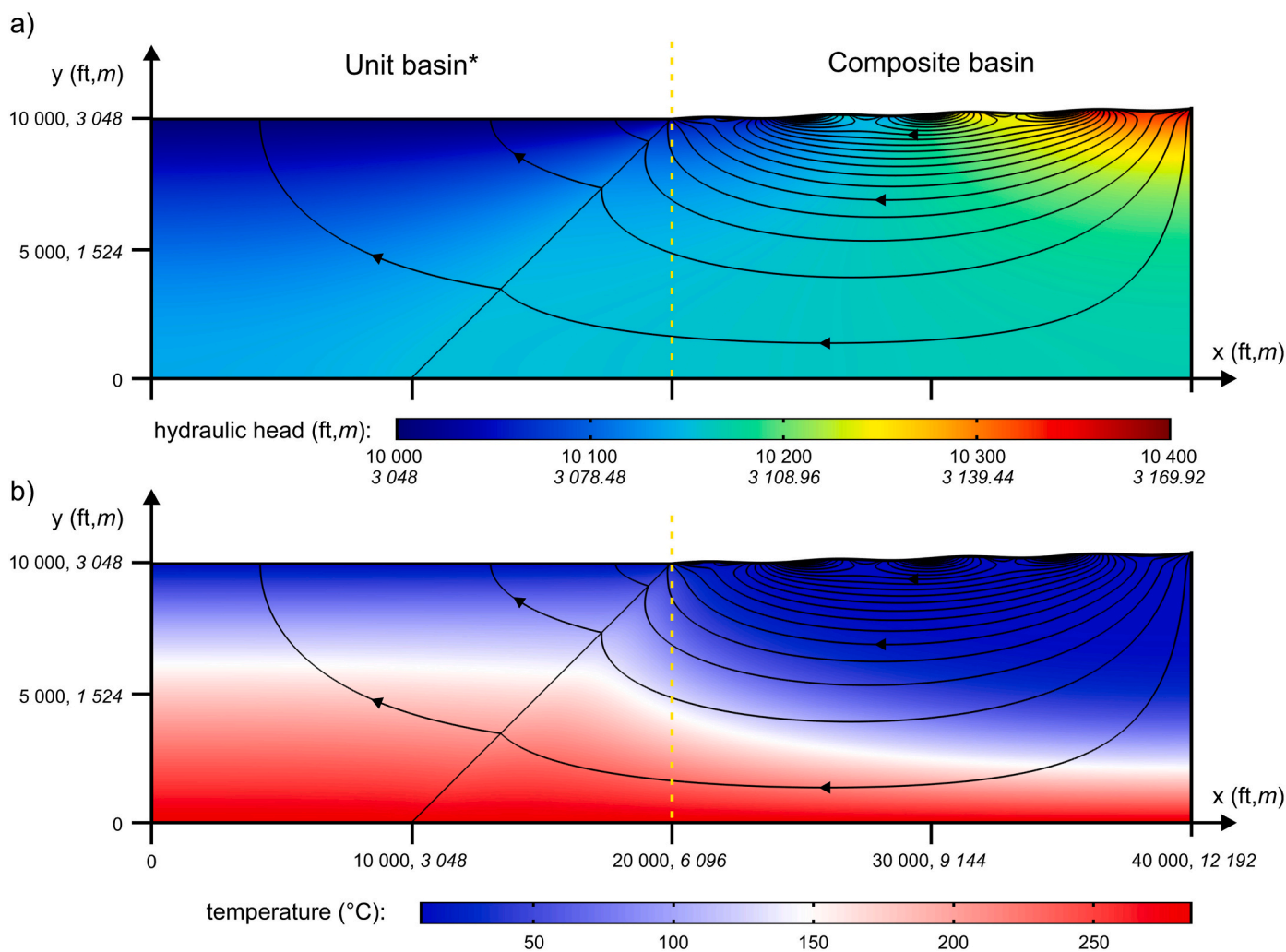
References

An, R., et al., 2015. A theoretical analysis of basin-scale groundwater temperature distribution. Hydrgeol. J. 23 (2), 397–404.

Anderson, M.P., 2005. Heat as a ground water tracer. Groundwater 43 (6), 951–968.

Anderson, M.P., Munter, J.A., 1981. Seasonal reversals of groundwater flow around lakes and the relevance to stagnation points and lake budgets. Water Resour. Res. 17 (4), 1139–1150.

Anderson, A., Rezaie, B., 2019. Geothermal technology: Trends and potential role in a sustainable future. Appl. Energy 248, 18–34.

Andrews, J.N., Burgess, W., Edmunds, W.M., Kay, R., Lee, D., 1982. The thermal springs of Bath. Nature 298, 339–343.

Aravena, D., et al., 2016. Assessment of high enthalpy geothermal resources and promising areas of Chile. Geothermics 59, 1–13.

Arnórsson, S., Bjarnason, J.Ö., Giroud, N., Gunnarsson, I., Stefánsson, A., 2006. Sampling and analysis of geothermal fluids. Geofluids 6 (3), 203–216.

Axelsson, G., 2008. Importance of Geothermal Reinjection, Workshop for Decision Makers on Direct Heating Use of Geothermal Resources in Asia, Tianjin, China. UNU-GTP, TBLRREM and TBGMED, CD.

Bauer, J.F., Krumbholz, M., Luijendijk, E., Tanner, D.C., 2019. A numerical sensitivity study of how permeability, porosity, geological structure, and hydraulic gradient control the lifetime of a geothermal reservoir. Solid Earth 10 (6), 2115–2135.

Beardsmore, G., Cull, J., 2001. Crustal Heat Flow. Cambridge University Press, Cambridge, 324 pp.

Békési, E., et al., 2018. Subsurface temperature model of the Hungarian part of the Pannonian Basin. Global Planet. Change 171, 48–64.

Bethke, C.M., 1985. A numerical model of compaction-driven groundwater flow and heat transfer and its application to the paleohydrology of intracratonic sedimentary basins. J. Geophys. Res. Solid Earth 90 (B8), 6817–6828.

Bethke, C.M., 1989. Modeling subsurface flow in sedimentary basins. Geol. Rundsch. 78 (1), 129–154.

Brassington, R., 2017. Field hydrogeology. John Wiley & Sons, Chichester, 312 pp.

Bredehoeft, J.D., 1997. Fault permeability near Yucca mountain. Water Resour. Res. 33 (11), 2459–2463.

Bredehoeft, J.D., 2018. The Toth Revolution. Groundwater 56 (1), 157–159.

Bresciani, E., et al., 2016. Groundwater flow systems theory: research challenges beyond the specified-head top boundary condition. Hydrgeol. J. 24 (5), 1087–1090.

Cardenas, M.B., Jiang, X.W., 2010. Groundwater flow, transport, and residence times through topography-driven basins with exponentially decreasing permeability and porosity. Water Resour. Res. 46 (11).

Carrillo-Rivera, J., 2000. Application of the groundwater-balance equation to indicate interbasin and vertical flow in two semi-arid drainage basins, Mexico. Hydrgeol. J. 8 (5), 503–520.

Carrillo-Rivera, J., Ouysse, S., 2013. Evaluation of Groundwater Flow System Functioning in Mexico to Reduce Drought Impacts, Drought in Arid and Semi-Arid Regions. Springer, pp. 269–280.

Celico, F., Petrella, E., Celico, P., 2006. Hydrogeological behaviour of some fault zones in a carbonate aquifer of Southern Italy: an experimentally based model. Terra Nova 18 (5), 308–313.

Chen, J., Kuang, X., Zheng, C., 2020. An empirical porosity–depth model for Earth's crust. Hydrgeol. J. 28, 2331–2339.

Cherubini, Y., Cacace, M., Scheck-Wenderoth, M., Moeck, I., Lewerenz, B., 2013. Controls on the deep thermal field: implications from 3-D numerical simulations for the geothermal research site Groß Schönebeck. Environ. Earth Sci. 70 (8), 3619–3642.

Cherubini, Y., Cacace, M., Scheck-Wenderoth, M., Noack, V., 2014. Influence of major fault zones on 3-D coupled fluid and heat transport for the Brandenburg region (NE German Basin). Geoth. Energ. Sci. 2 (1), 1–20.

Clark, S.P., 1966. Handbook of Physical Constants, 97. Geological Society of America, New York, 587 pp.

Clauser, C., Villinger, H., 1990. Analysis of conductive and convective heat transfer in a sedimentary basin, demonstrated for the Rheingraben. Geophys. J. Int. 100 (3), 393–414.

Cloetingh, S., et al., 2010. Lithosphere tectonics and thermo-mechanical properties: an integrated modelling approach for Enhanced Geothermal Systems exploration in Europe. Earth Sci. Rev. 102 (3–4), 159–206.

Craw, D., Koons, P., Zeitler, P., Kidd, W., 2005. Fluid evolution and thermal structure in the rapidly exhuming gneiss complex of Namche Barwa–Gyala Peri, eastern Himalayan syntaxis. J. Metam. Geol. 23 (9), 829–845.

Csontos, L., Vörös, A., 2004. Mesozoic plate tectonic reconstruction of the Carpathian region. Palaeogeogr. Palaeoclimatol. Palaeoecol. 210 (1), 1–56.

Deming, D., Sass, J.H., Lachenbruch, A.H., de Rito, R.F., 1992. Heat flow and subsurface temperature as evidence for basin-scale ground-water flow, North Slope of Alaska. Geol. Soc. Am. Bull. 104 (5), 528–542.

Dickson, M.H., Fanelli, M., 2004. What Is Geothermal Energy. International Geothermal Association, Pisa, Italy, pp. 1–38.

Domenico, P., Palciauskas, V., 1973. Theoretical analysis of forced convective heat transfer in regional ground-water flow. Geol. Soc. Am. Bull. 84 (12), 3803–3814.

Domenico, P., Schwartz, F., 1997. Physical and Chemical Hydrogeology. John Wiley and Sons, New York, 506 pp.

Dövényi, P., Horváth, F., 1988. A Review of Temperature, Thermal Conductivity, and Heat Flow Data for the Pannonian Basin (Chapter 16).

Ehrenberg, S., Nadeau, P., 2005. Sandstone vs. carbonate petroleum reservoirs: a global perspective on porosity-depth and porosity-permeability relationships. AAPG Bull. 89 (4), 435–445.

Engelen, G.B., Kloosterman, F.H., 2012. Hydrological Systems Analysis: Methods and Applications, 20. Springer Science & Business Media, New York, 196 pp.

Eppelbaum, L., Kutasov, I., Pilchin, A., 2014. Investigating deep lithospheric structures. In: Eppelbaum, L., Kutasov, I., Pilchin, A. (Eds.), Applied Geothermics. Springer, Heidelberg, pp. 269–391.

Faulds, J.E., Coolbaugh, M.F., Vice, G.S., Edwards, M.L., 2006. Characterizing structural controls of geothermal fields in the northwestern Great Basin: a progress report. Geothermal Resources Council Transactions 30, 69–76.

Faulds, J., Coolbaugh, M., Bouchot, V., Moeck, I., Oguz, K., 2010. Characterizing Structural Controls of Geothermal Reservoirs in the Great Basin, USA, and Western Turkey: Developing Successful Exploration Strategies in Extended Terranes. In: Proceedings World Geothermal Congress, Bali, 25–29 April 2010.

Forster, C., Smith, L., 1989. The influence of groundwater flow on thermal regimes in mountainous terrain: a model study. J. Geophys. Res. Solid Earth 94 (B7), 9439–9451.

Fournier, R., 1977. Chemical geothermometers and mixing models for geothermal systems. Geothermics 5 (1–4), 41–50.

Freeze, R.A., Cherry, J.A., 1979. Groundwater. Printice-Hall Inc, Englewood Cliffs, 604 pp.

Garven, G., 1995. Continental-scale groundwater flow and geologic processes. Annu. Rev. Earth Planet. Sci. 23 (1), 89–117.

Giggenbach, W.F., 1988. Geothermal solute equilibria. Derivation of Na-K-Mg-Ca geoindicators. Geochim. Cosmochim. Acta 52 (12), 2749–2765.

Gillespie, J., Nelson, S., Mayo, A., Tingey, D., 2012. Why conceptual groundwater flow models matter: a trans-boundary example from the arid Great Basin, western USA. Hydrgeol. J. 20 (6), 1133–1147.

Gokgoz, A., Yilmazli, I.E., Gungor, I., Yavuzer, I., 2010. Hydrogeology and environmental study at the Karahayit geothermal field (Western Turkey). Proc. World Geotherm. Congr. 1–7.

Grasby, S.E., Hutcheon, I., 2001. Controls on the distribution of thermal springs in the southern Canadian Cordillera. Can. J. Earth Sci. 38 (3), 427–440.

Gudmundsson, J.S., Freeston, D.H., Lienau, P.J., 1985. The lindal diagram. Geotherm. Res. Council Trans. 9 (1), 15–19.

!"count(.//sb:host[1]//child::*//sb:date)">Gutierrez-Negrin, L.C., . Cerro Prieto, Mexico—a Convective Extensional Geothermal Play. Geotherm. Res. Council Trans. 39, 2015.

Gutiérrez-Negrín, L.C., 2015. Mexican geothermal plays. Proc. World Geotherm. Congr. 9.

Haas, J., 2012. Geology of Hungary. Springer Science & Business Media, Heidelberg, 244 pp.

Handy, M.R., Schmid, S.M., Bousquet, R., Kissling, E., Bernoulli, D., 2010. Reconciling plate-tectonic reconstructions of Alpine Tethys with the geological–geophysical record of spreading and subduction in the Alps. Earth Sci. Rev. 102 (3–4), 121–158.

Hochstein, M.P., 1988. Assessment and modelling of geothermal reservoirs (small utilization schemes). Geothermics 17 (1), 15–49.

Hochstein, M.P., 1990. Classification and assessment of geothermal resources. In: Small geothermal resources: A guide to development and utilization. UNITAR, New York, pp. 31–57.

Horváth, F., et al., 2006. Formation and deformation of the Pannonian Basin: constraints from observational data. Geol. Soc. Lond. Mem. 32 (1), 191–206.

Horváth, F., et al., 2015. Evolution of the Pannonian basin and its geothermal resources. Geothermics 53, 328–352.

Izápy, G., 2002. Magyarország forrásainak kataszctere [Natural Spring Cadastral of Hungary]. VITUKI Rt. Hidrológiai Intézete.

Jiang, X.W., Wang, X.S., Wan, L., Ge, S., 2011. An analytical study on stagnation points in nested flow systems in basins with depth-decaying hydraulic conductivity. Water Resour. Res. 47 (1).

Jiang, X.W., et al., 2012. A quantitative study on accumulation of age mass around stagnation points in nested flow systems. Water Resour. Res. 48 (12).

Jiang, X.W., et al., 2014. Field identification of groundwater flow systems and hydraulic traps in drainage basins using a geophysical method. Geophys. Res. Lett. 41 (8), 2812–2819.

Jiang, Z., Xu, T., Mariethoz, G., 2018. Numerical investigation on the implications of spring temperature and discharge rate with respect to the geothermal background in a fault zone. Hydrgeol. J. 26 (7), 2121–2132.

Kato, V., 2016. Geothermal Exploration in Uganda. In: SDG Short Course I on Exploration and Development of Geothermal, Kenya, 10–31 November 2016.

Kaya, E., Zarrouk, S.J., O'Sullivan, M.J., 2011. Reinjection in geothermal fields: a review of worldwide experience. Renew. Sustain. Energy Rev. 15 (1), 47–68.

Khan, H.H., Khan, A., 2019. Groundwater and surface water interaction. In: Venkatramanan, S., Mohan Viswanathan, P., Chung, S.Y. (Eds.), GIS and Geostatistical Techniques for Groundwater Science. Elsevier, pp. 197–207.

Krešić, N., Stevanović, Z., 2009. Groundwater Hydrology of Springs: Engineering, Theory, Management and Sustainability. Butterworth-Heinemann, Oxford, 592 pp.

Lazear, G.D., 2006. Evidence for deep groundwater flow and convective heat transport in mountainous terrain, Delta County, Colorado, USA. Hydrgeol. J. 14 (8), 1582–1598.

Lenkey, L., Dövényi, P., Horváth, F., Cloetingh, S., 2002. Geothermics of the Pannonian basin and its bearing on the neotectonics. EGU Stephan Mueller Special Publ. Ser. 3, 29–40.

Lenkey, L., et al., 2017. Lithospheric scale 3D thermal model of the Alpine–Pannonian transition zone. Acta Geodaetica et Geophysica 52 (2), 161–182.

Limberger, J., et al., 2018. Geothermal energy in deep aquifers: a global assessment of the resource base for direct heat utilization. Renew. Sustain. Energy Rev. 82, 961–975.

Lindal, B., 1973. Industrial and other applications of geothermal energy. In: Armstead, H. C.H. (Ed.), Geothermal Energy. UNESCO, Paris, pp. 135–148.

López, D.L., Smith, L., 1995. Fluid flow in fault zones: analysis of the interplay of convective circulation and topographically driven groundwater flow. Water Resour. Res. 31 (6), 1489–1503.

Lopez, T. et al., 2016. Subsurface hydrology of the Lake Chad Basin from convection modelling and observations, Remote Sens. Water Res.. Springer, pp. 281–312.

Mádl-Szőnyi, J., Simon, S., 2016. Involvement of preliminary regional fluid pressure evaluation into the reconnaissance geothermal exploration—example of an overpressured and gravity-driven basin. Geothermics 60, 156–174.

Mádl-Szőnyi, J., Tóth, Á., 2015. Basin-scale conceptual groundwater flow model for an unconfined and confined thick carbonate region. Hydrgeol. J. 23 (7), 1359–1380.

Mádl-Szőnyi, J., et al., 2019. Confined carbonates–Regional scale hydraulic interaction or isolation? Mar. Pet. Geol. 107, 591–612.

Markovich, K.H., Manning, A.H., Condon, L.E., McIntosh, J.C., 2019. Mountain-block recharge: a review of current understanding. Water Resour. Res 55 (11), 8278–8304.

McKenna, J.R., Blackwell, D.D., 2004. Numerical modeling of transient basin and range extensional geothermal systems. Geothermics 33 (4), 457–476.

Moeck, I.S., 2014. Catalog of geothermal play types based on geologic controls. Renew. Sustain. Energy Rev. 37, 867–882.

Moeck, I.S., Beardsmore, G., 2014. A new 'geothermal play type' catalog: streamlining exploration decision making. In: Proceedings of the Thirty-Ninth Workshop on Geothermal Reservoir Engineering. Stanford University, Stanford, California.

Moeck, I.S., Beardsmore, G., Harvey, C.C., 2015. Cataloging Worldwide Developed Geothermal Systems by Geothermal Play Type. In: Proceedings of the World Geothermal Congress, Melbourne, Australia, pp. 19–25.

Muffler, L.J.P., 1979. Assessment of Geothermal Resources of the United States - 1978 (U.S. Geological Survey Circular).

Nádor, A., Sebess-Zilahi, L., Rotár-Szalkai, Á., Gulyás, Á., Markovic, T., 2019. New methods of geothermal potential assessment in the Pannonian basin. Neth. J. Geosci. 98, E10.

Noack, V., Scheck-Wenderoth, M., Cacace, M., Schneider, M., 2013. Influence of fluid flow on the regional thermal field: results from 3D numerical modelling for the area of Brandenburg (north German Basin). Environ. Earth Sci. 70 (8), 3523–3544.

Otieno, V., 2020. Structural controls on fluid pathways in active geothermal systems. Insights from Olkaria Geothermal Field, Kenya. In: Proceedings World Geothermal Congress, 21–26 May 2021, p. 5.

Özkaymak, Ç. and Sözbilir, H., Evidence for extensional domain-type geothermal play in western anatolia: a case study from afyon-akşehir graben, Proceedings World Geothermal Congress, 21-26 May 2021, pp. 9.

Özler, H.M., 2000. Hydrogeology and geochemistry in the Curuksu (Denizli) hydrothermal field, western Turkey. Environ. Geol. 39 (10), 1169–1180.

Pentecost, A., Jones, B., Renaut, R., 2003. What is a hot spring? Can. J. Earth Sci. 40 (11), 1443–1446.

Person, M., Raffensperger, J.P., Ge, S., Garven, G., 1996. Basin-scale hydrogeologic modeling. Rev. Geophys. 34 (1), 61–87.

Prol-Ledesma, R.M., Morán-Zenteno, D.J., 2019. Heat flow and geothermal provinces in Mexico. Geothermics 78, 183–200.

Przybycin, A.M., Scheck-Wenderoth, M., Schneider, M., 2017. The origin of deep geothermal anomalies in the German Molasse Basin: results from 3D numerical models of coupled fluid flow and heat transport. Geotherm. Energy 5 (1), 1.

Raffensperger, J.P., Vlassopoulos, D., 1999. The potential for free and mixed convection in sedimentary basins. Hydrgeol. J. 7 (6), 505–520.

Renner, J., White, D., Williams, D., 1975. Hydrothermal Convection Systems (U.S. Geological Survey Circular).

Rivera Diaz, A., Kaya, E., Zarrouk, S.J., 2016. Reinjection in geothermal fields − a worldwide review update. Renew. Sustain. Energy Rev. 53, 105–162.

Rman, N., et al., 2015. Potentials of transboundary thermal water resources in the western part of the Pannonian basin. Geothermics 55, 88–98.

Rman, N., et al., 2020. Geothermal sources and utilization practice in six countries along the southern part of the Pannonian basin. Environ. Earth Sci. 79 (1), 1.

Rotár-Szalkai, Á., et al., 2017. Outline and joint characterization of Transboundary geothermal reservoirs at the western part of the Pannonian basin. Geothermics 70, 1–16.

Rybach, L., 1981. Geothermal systems, conductive heat flow, geothermal anomalies. In: Rybach, L., Muffler, L.J.P. (Eds.), Geothermal Systems: Principles and Case Histories. Wiley, New York, pp. 3–76.

Rybach, L., 2007. The geothermal conditions in the Rhine Graben-a summary. Bulletin für Angewandte Geologie 12 (1), 29–32.

Rybach, L., 25-29 April 2010. The future of geothermal energy and its challenges. Proc. World Geotherm. Congr.

Rybach, L., 2015. Classification of geothermal resources by potential. Geotherm. Energy Sci. 3 (1), 13.

Rybach, L., 1985. Heat Flow and Geothermal Processes: Proceedings of the IUGG Inter-disciplinary Symposium No. 10 Held in Hamburg, West Germany, Aug. 1983. Expro Science Publ.

Sanyal, S.K., 2005. Classification of Geothermal Systems–A Possible Scheme, Proceedings of the 13th Workshop on Geothermal Reservoir Engineering. Stanford, California, pp. 85–88.

Schindler, M., et al., 25-29 April 2010. Successful hydraulic stimulation techniques for electric power production in the Upper Rhine Graben, Central Europe. Proc. World Geotherm. Congr.

Schmid, S.M., et al., 2008. The Alpine-Carpathian-Dinaridic orogenic system: correlation and evolution of tectonic units. Swiss J. Geosci. 101 (1), 139–183.

Sharma, P.V., 1997. Environmental and Engineering Geophysics. Cambridge University Press, Cambridge, 475 pp.

Siler, D.L., Faulds, J.E., 2013. Three-Dimensional Geothermal Fairway Mapping: Examples from the Western Great Basin, USA. Geothermal Resources Council, Davis, CA, United States.

Smith, L., Chapman, D.S., 1983. On the thermal effects of groundwater flow: 1. Regional scale systems. J. Geophys. Res. Solid Earth 88 (B1), 593–608.

Stefansson, V.-d., 1997. Geothermal reinjection experience. Geothermics 26 (1), 99–139.

Szijártó, M., Galsa, A., Tóth, Á., Mádl-Szőnyi, J., 2019. Numerical investigation of the combined effect of forced and free thermal convection in synthetic groundwater basins. J. Hydrol. 572, 364–379.

Tóth, J., 1962a. A Theoretical Analysis of Ground-Water Flow in Small Drainage Basins: Proceedings Hydrology Symposium 3. Groundwater. Queens Printers, Ottawa, pp. 75–96.

Tóth, J., 1962b. A theory of groundwater motion in small drainage basins in Central Alberta, Canada. J. Geophys. Res. 67 (11), 4375–4388.

Tóth, J., 1963. A theoretical analysis of groundwater flow in small drainage basins. J. Geophys. Res. 68 (16), 4795–4812.

Tóth, J., 1970. A conceptual model of the groundwater regime and the hydrogeologic environment. J. Hydrol. 10 (2), 164–176.

Tóth, J., 1971. Groundwater discharge: a common generator of diverse geologic and morphologic phenomena. Hydrol. Sci. J. 16 (1), 7–24.

Tóth, J., 1980. Cross-formational gravity-flow of groundwater: A mechanism of the transport and accumulation of petroleum (the generalized hydraulic theory of petroleum migration). In: Roberts, W., Cordell, R. (Eds.), Problems of Petroleum Migration. American Association of Petroleum Geologists, Tulsa, pp. 121–167.

Tóth, J., 1987. Petroleum hydrogeology: a potential application of groundwater science. J. Geol. Soc. India 29 (1), 172–179.

Tóth, J., 1995. Hydraulic continuity in large sedimentary basins. Hydrgeol. J. 3 (4), 4–16.

Tóth, J., 1999. Groundwater as a geologic agent: an overview of the causes, processes, and manifestations. Hydrgeol. J. 7 (1), 1–14.

Tóth, J., 2009a. Gravitational Systems of Groundwater Flow: Theory, Evaluation, Utilization. Cambridge University Press, Cambridge, 297 pp.

Tóth, J., 2009b. Springs Seen and Interpreted in the Context of Groundwater Flow-Systems. GSA Annual Meeting, Portland, USA, p. 173.

Tóth, J., 2015. Geothermal phenomena in the context of gravity-driven basinal flow of groundwater. Central Eur. Geol. 58 (1–2), 1–27.

Tóth, J., 2016. The evolutionary concepts and practical utilization of the Tóthian theory of regional groundwater flow. Int. J. Earth Environ. Sci. 111 https://doi.org/10.15344/ijees/2016/111, 2016, Article ID 1.

Tóth, Á., 2018. A Balaton-felvidék felszínalatti vizeinek hidraulikai kapcsolata a Bakonnyal és a Balatonnal [Groundwater flow systems and hydraulic connection of the Bakony - Balaton Highland - Lake Balaton region]. Ph.D. thesis Thesis. ELTE Eötvös Loránd University, Budapest, 172 pp.

Tóth, J., Sheng, G., 1996. Enhancing safety of nuclear waste disposal by exploiting regional groundwater flow: the recharge area concept. Hydrgeol. J. 4 (4), 4–25.

Tóth, G., et al., 2016. Transboundary fresh and thermal groundwater flows in the west part of the Pannonian Basin. Renew. Sustain. Energy Rev. 57, 439–454.

Wang, X.S., Jiang, X.W., Wan, L., Ge, S., Li, H., 2011. A new analytical solution of topography-driven flow in a drainage basin with depth-dependent anisotropy of permeability. Water Resour. Res. 47 (9), 1–17.

Wang, J., et al., 2016. Investigation of discharge-area groundwaters for recharge source characterization on different scales: the case of Jinan in northern China. Hydrgeol. J. 24 (7), 1723–1737.

Wang, C., Lo, W., Song, S.-R., 2018. Geothermal play fairway analysis at a populated rifting basin area of Taiwan. Geothermics 75, 146–153.

Welch, A.H., Bright, D.J., Knochenmus, L.A., 2007. Water Resources of the Basin and Range Carbonate-Rock Aquifer System, White Pine County, Nevada, and Adjacent Areas in Nevada and Utah.

Wilson, J.L., Guan, H., 2004. Mountain-block hydrology and mountain-front recharge. In: Groundwater recharge in a desert environment: the Southwestern United States, p. 9.

Wisian, K.W., Blackwell, D.D., 2004. Numerical modeling of basin and range geothermal systems. Geothermics 33 (6), 713–741.

Wooding, R., 1963. Convection in a saturated porous medium at large Rayleigh number or Peclet number. J. Fluid Mech. 15 (4), 527–544.

Yang, J., Large, R.R., Bull, S., Scott, D.L., 2006. Basin-scale numerical modeling to test the role of buoyancy-driven fluid flow and heat transfer in the formation of stratiform Zn-Pb-Ag deposits in the northern Mount Isa basin. Econ. Geol. 101 (6), 1275–1292.

Yang, P., et al., 2017. Hydrogeochemistry and geothermometry of deep thermal water in the carbonate formation in the main urban area of Chongqing, China. J. Hydrol. 549, 50–61.

Ye, M., Wang, L., Pohlmann, K.F., Chapman, J.B., 2016. Evaluating groundwater interbasin flow using multiple models and multiple types of data. Groundwater 54 (6), 805–817.

Zimmerman, W.B., 2006. Multiphysics Modeling with Finite Element Methods, 18. World Scientific Publishing Company, London, 422 pp.

Zlotnik, V.A., Cardenas, M.B., Toundykov, D., 2011. Effects of multiscale anisotropy on basin and hyporheic groundwater flow. Groundwater 49 (4), 576–583.